

DISS. ETH No. 25416

**DOUBLE MODULATION PYROMETRY
WITH EMISSIVITY CORRECTION:
A RADIOMETRIC METHOD TO
DETERMINE THE TEMPERATURE OF
RADIATIVELY HEATED SURFACES**

A thesis submitted to attain the degree of
DOCTOR OF SCIENCES of ETH ZURICH
(Dr. sc. ETH Zurich)

presented by
DIMITRIOS POTAMIAS
MSc ETH

born on 14.10.1985
citizen of Greece

accepted on the recommendation of
Prof. Dr. Alexander Wokaun, examiner
Prof. Dr. Gunnar Jeschke, co-examiner
Dr. Ivo Alxneit, co-examiner

2018

Abstract

The present work addresses the challenge of determining the temperature of a radiatively heated opaque surface by measuring and analyzing its radiosity. Determining the temperature of directly irradiated surfaces is a recurrent problem in many high-temperature experiments. It is particularly so in the field of concentrated solar power (CSP), where targets are heated to high temperatures by exposure to broadband concentrated radiation.

Extracting accurate temperature information about the irradiated target would provide further insight into the operating conditions of concentrated solar facilities and enhance the development of novel materials for CSP applications. To this end, the use of radiometric thermometers is attractive due to their characteristics of direct optical access and fast dynamic response, while the use of contact methods in these setups is problematic due to the intense irradiation and the development of high-temperature gradients. Nevertheless, the accuracy of radiometric sensors is severely limited by the combined effects of intense reflected radiation and unknown, varying emissivity of the target which contribute two correlated and variable error terms.

To enable accurate radiometric temperature measurement in solar simulators, the parasitic reflectance, which amounts to a significant portion of the radiosity signal, has to be separated from the thermal self-emission signal that bears the temperature information. To this end, in the present work a novel radiometric method, double modulation pyrometry (DMP), is developed and experimentally demonstrated in three representative CSP facilities. The operating principle of DMP relies on amplitude modulation and phase sensitive detection to independently measure the irradiance (I_0) reflected by the sample as well as the radiosity, i.e. the sum of thermal and reflected radiation emanating from the surface. From the difference of these independent measurements, the thermal emission signal bearing the temperature information is extracted.

The method is experimentally demonstrated by building a prototype in a single-source 1-kW_e solar simulator. Its design, implementation, calibration and performance assessment is presented. To modulate the intensity of external radiation, a mechanical modulator mounted parallel to the optical axis of the simulator is real-

ized based on the design proposed by a ray-tracing analysis. A two-step calibration procedure is developed. The first step equalizes the gains of the voltage signals that are obtained from the independent measurements of reflected irradiance and radiosity emanating from a cold lambertian surface, while the second step determines the mapping from the voltage to the temperature scale. To implement the second step, an experimental setup is realized that allows transferring the scale from a readily available calibrated pyrometer operating at a different wavelength. The systematic error introduced as a result of the proposed calibration setup is analyzed and the combined uncertainty in the output variable that results from the calibration and measurement steps is estimated by Monte-Carlo simulation. The performance of DMP was assessed by conducting measurements on a thin platinum strip where it was demonstrated that DMP can eliminate the contribution of reflected radiation and can attain satisfactory measurement accuracy ($\approx \pm 20$ K) in the case of the low emissivity metallic sample. The method is validated by observing the melting point of the platinum sample. Even though the method performs adequately in the benign case of a constant emissivity sample, it requires the emissivity value to be provided externally and therefore it is exposed to an emissivity error that might be more severe in the case of samples with variable optical properties.

Next, an improvement of DMP with *in-situ* measurement of reflectance and online emissivity correction is demonstrated. Since in a CSP facility, samples are irradiated by the broadband I_0 under an approximately hemispherical configuration, while the narrow-band DMP observes under a relatively small solid angle, the hemispherical-directional spectral reflectance factor can be measured *in-situ* and used to correct the emissivity error. This is advantageous during solar experiments where the material under test undergoes dynamic emissivity changes. The enhanced prototype is implemented at Paul Scherrer Institute's 50 kW multi-source high-flux solar simulator and used to measure the temperature of ceramic foams (SiSiC, ZrO₂, and Al₂O₃) during fast-heat-up. The enhancement improves accuracy, enabling DMP to determine the true temperature despite the temporal variation of emissivity and to identify signature surface changes in the ZrO₂ and Al₂O₃ samples. During the dynamic experiments, the two dominant error sources - parasitic reflectance and unknown emissivity - are studied by tracking the evolution of the respective error components. Furthermore, measurements from a solar cavity-receiver are obtained, where the presence of the cavity reflection error limits measurement accuracy.

So far, the experiments were conducted under artificial concentrated solar radiation and therefore did not allow for direct comparison with another radiometric method since solar blind pyrometry (SBP), the de facto method in solar furnace experiments, cannot cope with the continuous spectrum of the Xenon-arc lamp

that is used as light source in solar simulators. To this end, the method was applied to experiments in a natural concentrated sunlight facility at CNRS France, where it is feasible to directly compare the measurement results against a calibrated solar-blind pyrometer operating at $5.5 \mu\text{m}$. Compared to SBP, DMP offers the relative advantage of freely selecting the operating wavelength within the IR spectral region. The performance of DMP is assessed at four wavelengths ($\lambda = 0.88, 1.0, 1.1, 1.2 \mu\text{m}$) and the DMP measurements generally agree with the reference pyrometer within approximately 100 K.

The proposed method can be used as an accurate radiometric thermometer in the adverse conditions of concentrated radiation, and as a diagnostic tool to characterize materials with dynamic optical properties. Its simple design and ability to correct for the two dominant errors render it a useful tool for experiments in concentrated solar power facilities.

Zusammenfassung

Die vorliegende Arbeit befasst sich mit der Herausforderung, die Temperatur einer strahlungsbeheizten opaken Oberfläche durch Messung und Analyse ihres Strahlungsaustausches mit einer Lichtquelle und der Umgebung zu bestimmen. Die Bestimmung der Temperatur direkt bestrahlter Oberflächen ist in vielen Hochtemperaturanwendungen ein wiederkehrendes Problem. Dies gilt insbesondere für den Bereich der konzentrierten Solarenergie, wo die Zieloberflächen durch konzentrierte Breitbandstrahlung auf hohe Temperaturen erhitzt werden.

Das Extrahieren von genauen Temperaturinformationen über die bestrahlte Zieloberfläche würde weitere Einblicke in die Betriebsbedingungen konzentrierter Solaranlagen anbieten und die Entwicklung neuartiger Materialien für CSP Anwendungen fördern. Zu diesem Zweck ist die Verwendung von radiometrischen Thermometern aufgrund ihrer direkten optischen Zugriffs und ihrer schnellen dynamischen Reaktion attraktiv, wohingegen die Verwendung von Kontaktmethoden problematisch wegen der intensiven Bestrahlung und der Entwicklung von Hochtemperaturgradienten ist. Trotzdem ist die Genauigkeit radiometrischer Sensoren durch die reflektierte Strahlung und die mit der Temperatur unbekannt variierende Emissivität der Zieloberfläche stark eingeschränkt.

Um eine genaue radiometrische Temperaturmessung in Sonnensimulatoren zu ermöglichen, muss die parasitäre Strahlungsreflektion von der Zieloberfläche, die einen wesentlichen Teil des Messsignals ausmacht, von dem thermischen Eigenemissionssignal, das die eigentliche Temperaturinformation trägt, getrennt werden. Zu diesem Zweck wird in der vorliegenden Studie eine neuartige radiometrische Methode, die Doppelmodulations-Pyrometrie (DMP), entwickelt und experimentell in drei repräsentativen CSP-Anlagen demonstriert. Das Funktionsprinzip der DM-Pyrometrie beruht auf dem Verfahren der Amplitudenmodulation und phasempfindlicher Detektion zur Messung der von der Probe reflektierten Bestrahlungsstärke (I_0) sowie der Radiosität, d.h. der Summe der thermischen und reflektierten Strahlung, die von der Zieloberfläche ausgeht. Aus dem Unterschied dieser unabhängigen Messungen wird das thermische Emissionssignal extrahiert, das die Temperaturinformation trägt.

Die Methode wird experimentell demonstriert, indem ein Prototyp in einem

1-kW_e Einlichtquellen-Solarsimulator gebaut wird. Sein Design, Implementierung, Kalibrierung und Leistungsbewertung werden in der vorliegenden Studie vorgestellt. Um die Intensität der externen Strahlung zu modulieren, wird ein parallel zu der optischen Achse des Simulators montierter mechanischer Modulator benutzt. Das Design wurde durch ein numerisches ray-tracing Modell unterstützt und ein zweistufiges Kalibrierungsverfahren wurde entwickelt. Der erste Schritt gleicht die Verstärkung der Spannungssignale aus, die aus unabhängigen Messungen der von einer kalten Lambert'schen Oberfläche ausgehenden reflektierten Strahlung und Radiosität erhalten werden. Der zweite Schritt ermöglicht die Zuordnung der Spannungssignale auf die Temperaturskala. Um den zweiten Schritt zu implementieren, wird ein Versuchsaufbau realisiert, der die Übertragung der Skala von einem leicht verfügbaren kalibrierten Pyrometer, das bei einer anderen Wellenlänge arbeitet, ermöglicht. Der systematische Fehler, der als Ergebnis der vorgeschlagenen Kalibrierungsmethode eingeführt wird, wird analysiert und die kombinierte Unsicherheit in der Ausgangsvariable, die sich aus den Kalibrierungs- und Messschritten ergibt, wird durch Monte-Carlo-Simulation geschätzt. Die Leistung der DMP-Methode wurde durch Messungen an einem dünnen Platinstreifen bewertet und es wurde gezeigt, dass DMP den Beitrag der reflektierten Strahlung eliminieren kann und eine zufriedenstellende Messgenauigkeit ($\approx \pm 20$ K) im Fall der niedrig emittierenden metallischen Probe erreichen kann. Die Methode wird validiert, indem der Schmelzpunkt der Platinprobe beobachtet wird. Obwohl das Verfahren im Fall einer Probe mit konstanter Emissivität angemessen arbeitet, erfordert es eine externe Bereitstellung der Emissivität und ist daher einem Emissivitätsfehler ausgesetzt, der im Fall von Proben mit variablen optischen Eigenschaften schwerwiegender sein könnte.

Als Nächstes wird eine Verbesserung von DMP demonstriert, die eine in-situ Messung der reflektierten Strahlung beinhaltet. Dieser Ansatz ermöglicht, dass der Wert der gerichteten Reflektanz gemessen statt angenommen wird und dazu verwendet werden kann, den Emissivitätsfehler zu eliminieren. Dies ist vorteilhaft bei Solarexperimenten, bei welchen das zu testende Material dynamische Emissivitätsänderungen aufweist. Der verbesserte Prototyp wird am 50 kW Mehrlichtquellen-Hochfluss-Solarsimulator des Paul Scherrer Instituts implementiert und zur Messung der Temperatur von schnell aufgeheizten Keramikschaumen (SiSiC, ZrO₂ und Al₂O₃) verwendet. Der neue Prototyp verbessert die Genauigkeit und ermöglicht es, mittels DMP die wahre Temperatur trotz der zeitlichen Variation der Emissivität zu bestimmen und Oberflächenänderungen in Proben von ZrO₂ und Al₂O₃ zu identifizieren. Während der dynamischen Experimente werden die zwei dominanten Fehlerquellen, d.h. die parasitäre Reflexion und die unbekannte Emissivität, untersucht, indem man die Entwicklung der jeweiligen Fehlerkomponenten verfolgt. Außerdem werden zusätzliche Messungen von einem kavitätstförmigen

Solarempfänger erhalten, wo die mehrfache Reflektion innerhalb der Kavität die Messgenauigkeit begrenzt.

Die unter künstlicher konzentrierter Sonneneinstrahlung durchgeführte Experimente erlaubten bisher keinen direkten Vergleich mit einem anderen radiometrischen Messverfahren, da die Solar-Blind-Pyrometrie (SBP), das De-facto Messverfahren in Solarofen-Experimenten, das kontinuierliche Spektrum der als Lichtquelle in Solarsimulatoren verwendeten Xenon-Bogenlampen nicht bewältigen kann. Zu diesem Zweck wurde das DMP Verfahren bei Experimenten in einer Anlage mit natürlichem konzentriertem Sonnenlicht bei CNRS France getestet, wo es möglich ist, die Ergebnisse direkt mit einem kalibrierten Solarblind-Pyrometer zu vergleichen, das bei $5.5 \mu\text{m}$ arbeitet. Im Vergleich zur SBP bietet DMP den Vorteil der freien Wahl der Betriebswellenlänge im IR-Spektralbereich. Die Leistung von DMP wird bei vier Wellenlängen bewertet ($\lambda = 0.88, 1, 1.1, 1.2 \mu\text{m}$), und die DMP-Messungen stimmen im Allgemeinen mit der Referenz innerhalb von etwa 100 K überein.

Das vorgeschlagene Messverfahren kann als genaues radiometrisches Thermometer unter den widrigen Bedingungen konzentrierter Strahlung und als Diagnosteinstrument zur Charakterisierung von Materialien mit dynamischen optischen Eigenschaften verwendet werden. Sein einfaches Design und seine Fähigkeit, die zwei dominanten Fehler zu korrigieren, machen es zu einem nützlichen Werkzeug für Experimente in konzentrierten Solarenergieanlagen.

Acknowledgements

First of all, I would like to express my gratitude towards my supervisors Prof. Dr. Alexander Wokaun and Dr. Ivo Alxneit for giving me the unique opportunity to conduct my doctoral research at the Solar Technology Laboratory at the Paul Scherrer Institute. It was a great honor to work under the supervision of Prof. Dr. Wokaun. His valuable guidance of my research over the course of this project was indispensable for the completion of this work and I would like to sincerely thank him. The continuous right-on advice, guidance, support and feedback of Dr. Alxneit were instrumental for the completion of my thesis and are tremendously appreciated.

I would like to further thank Prof. Dr. Gunnar Jeschke, Head of the Electron Paramagnetic Resonance Group at the laboratory of the physical chemistry of ETH Zurich, for serving as co-examiner of my thesis.

I am also very grateful to Dr. Erik Koepf for closely collaborating on parts of this project. His creative ideas and suggestions as well as his experimental excellence were invaluable. I would like to profoundly thank him for sharing his great expertise and for his continuous support and help.

I am also very grateful to Prof. Oliver Kröcher for welcoming me into the Catalysis for Energy Group during the last year of my thesis and for the valuable feedback. Special thanks go to Dr. Christian Wieckert for his interest in my project and for always taking the time to discuss and provide me with great advice as well as to Dr. Anton Meier for his support.

The experimental work carried out throughout this project would not have been possible without the great support and contribution of the team at PSI. I would like to especially thank Alwin Frei, Daniel Wuillemin, Yvonne Bäuerle and Valentin Schnentzler for the numerous hours, continuous help and impeccable technical expertise provided during my project.

I am grateful to Emmanuel Guillot, Jean-Louis Sans and Nicolas Boulet for their collaboration during the experimental campaign at the CNRS facility in Odeillo, France. I would like to thank them for sharing their expertise and knowledge as well as their support.

Financial support by the European Union through the SFERA II project

(Grant Agreement No. 312643) is gratefully acknowledged.

I would like to also express my gratitude to my friends and colleagues at the Solar Technology Lab. Special thanks go to Nikolas for his priceless friendship and support and to Chris, Kay, Manolis, Miriam, Sebastian and Stefan for the fun time and fruitful discussions.

Finally, I am grateful to Cynthia for always being there for me, supporting and inspiring me every step of the way. Last but not least, I would like to express my deepest gratefulness to my parents for their unconditional love and support. I dedicate this thesis to them.

Contents

1	Introduction	1
1.1	Motivation for radiometric temperature measurement	1
1.2	The general problem of pyrometry	2
1.3	Temperature measurement in concentrated solar power facilities . .	3
1.4	Thesis outline	9
2	An overview of pyrometric methods	11
2.1	Elimination of ΔT_ε	11
2.1.1	Ratio pyrometry	11
2.1.2	Multi-wavelength pyrometry	14
2.1.3	Multi-wavelength pyrometry with reflectance measurement .	17
2.1.4	Pyroreflectometry	19
2.1.5	Polarization pyrometry	20
2.2	Elimination of ΔT_ρ	21
2.2.1	Solar blind pyrometry (SBP)	21
2.2.2	Short-wavelength pyrometry	22
2.2.3	Flash-assisted multi-wavelength pyrometry	22
3	Theory	25
3.1	Planck's law	25
3.2	Emissivity	26
3.3	Radiance Temperature	26
3.3.1	Radiance Equation	27
3.3.2	Effective Emissivity	27
3.3.3	Emissivity Error ΔT_ε	27
3.4	Lambertian Surface	28
3.5	Measurement equation	29
3.6	Operating principle of double modulation pyrometry	30
3.6.1	Double modulation	31
3.6.2	Phase sensitive detection	31
3.6.3	Gain calibration	32

3.6.4	<i>In-situ</i> indirect measurement of spectral directional emissivity	33
3.6.5	Temperature calibration	34
4	Double Modulation Pyrometry: A radiometric method to measure surface temperatures of directly irradiated samples	37
4.1	Introduction	38
4.2	Theory of Double Modulation Pyrometry	39
4.3	Calibration Procedure	41
4.3.1	Gain Calibration	41
4.3.2	Temperature Calibration	42
4.4	Implementation of double modulation pyrometry at the 1 kW imaging furnace	44
4.4.1	Mechanical Modulation	45
4.5	Evaluation of the performance of double modulation pyrometry at the 1 kW imaging furnace	50
4.6	Error Analysis	53
4.7	Conclusion	55
5	Double modulation pyrometry with emissivity correction based on <i>in-situ</i> reflectance measurements applied to surfaces with dynamic optical properties	59
5.1	Introduction	60
5.2	Methodology of Double Modulation Pyrometry	61
5.3	Design of the Modulator	64
5.4	Experimental Setup	66
5.5	Results	68
5.6	Discussion of the error terms	72
5.7	Temperature measurement in a solar receiver	74
5.8	Conclusion	78
6	Assessment of Double Modulation Pyrometry as a diagnostic tool for use in concentrated solar facilities	79
6.1	Introduction	79
6.2	Theory	81
6.2.1	Double Modulation Pyrometer	81
6.3	Experimental	83
6.4	Gain Calibration	84
6.5	Temperature Calibration	86
6.6	Results and Discussion	87
6.6.1	Copper	89
6.6.2	Stainless Steel 310S	92

CONTENTS

6.6.3	Al_2TiO_5	94
6.6.4	ZrO_2 reticulate porous ceramic	96
6.6.5	CeO_2 reticulate porous ceramic	97
6.7	Conclusion	98
7	Conclusions and Outlook	101

Chapter 1

Introduction

1.1 Motivation for radiometric temperature measurement

Temperature is the primary means by which macroscopic information about the thermodynamic state of a physical system can be obtained. It is one of the most frequently measured experimental quantities in natural and engineering sciences as it is linked to the rate of chemical reactions, the thermodynamic efficiency of heat engines, the reproductive rate of living cells. Accurate temperature measurement is paramount in scientific experimentation and industrial applications where it is used in diagnostics and process control.

Temperature information can be obtained by using a transducer that relies either on *conduction* or *radiation* of heat as its operating principle. The former route requires bringing a probe in *contact* with the studied system, while the latter involves a direct, *non-contact* measurement of thermal radiance to infer the thermodynamic state of the observed sample.

Under conditions of high temperatures or radiatively heated surfaces, contact probes become prone to measurement bias, via the conductive or radiative heat transfer mode. If the point of interest is not directly accessible, a sensor placed at a distance from the point of interest will incur a temperature error. In case of radiatively heated surfaces, as is the case with the set of problems examined in the present work, a probe mounted between the radiation source and target surface disturbs the radiative transfer. Any mismatch in the optical properties (absorptivity) of the probe relative to the surrounding surface would cause a mismatch in measured temperature and cause the thermocouple to act as a heatsink.

Radiometric methods obtain information about the temperature of the observed sample by analyzing its thermal radiance. A radiometer outputs an electronic signal linear to the detected radiance. A *radiometric thermometer* or *pyrom-*

eter is a radiometer that has been calibrated so that its response to the spectral radiance of the observed object can be associated with temperature.

The advantage of pyrometry stems from the non-contact operating principle that allows direct optical access to the measurement area and fast dynamic response allowing for measurements with high temporal resolution. Samples can be probed that are remotely located, in motion, or embedded in hostile environments, where high temperatures or chemical reactivity would risk destroying a contact probe. Due to these characteristics, pyrometry is used in many scientific and industrial applications, where the measurement of high temperatures above ≈ 500 K is required. It is utilized to obtain real-time measurements of surface temperature in the metallurgical [1], glass [2] and semiconductor [3, 4] industries. In scientific research, it is applied in high-temperature material testing [5], in the measurement of thermo-optical properties [6], the characterization of solar driven thermo-chemical reactions and to determine the temperature of coal [7], sulfide [8], polymer particles [9], or diesel flames during combustion [10]. Additional applications include the temperature determination of the blade's surface in gas turbines [11, 12], of laser heated targets and plasma facing components [13] in nuclear fusion experiments.

1.2 The general problem of pyrometry

Pyrometric methods rely on detecting the thermal radiation emitted off an opaque surface (I_ε) and comparing it to the black body radiation (I_{bb}) to determine the temperature of the target surface. In doing so they face two main challenges: (a) a temperature error ΔT_ρ due to any external radiation flux that has been reflected off the target and is mixed with the thermal emission, (b) a temperature error ΔT_ε resulting from the uncertainty about the correct value of surface emissivity.

Assuming an optically thick ($\tau = 0$), diffuse reflective ($\varepsilon(\cdot|\theta) = \varepsilon(\cdot)$) surface at temperature T being in radiative exchange with its environment, it holds from Kirchhoff's law that $\tau + \alpha + \rho = 1$. In addition we assume that the surface is exposed to irradiance I_0 so that I_0/I_ε is nonnegligible. The spectral *radiosity* detected by a pyrometer (\hat{I}) observing the surface is the sum of a *reflected* component (I_ρ) and an *emitted* component ($I_\varepsilon = \varepsilon \cdot I_{\text{bb}}$) that holds information about T . Assuming a calibrated radiometer, \hat{I} will map to a measured temperature (\hat{T}).

$$\begin{aligned} \hat{I} &= \underbrace{\varepsilon \cdot I_{\text{bb}}(\lambda, T)}_{I_\varepsilon} + \underbrace{\rho \cdot I_0(\lambda)}_{I_\rho} \\ \hat{T} &= T + \Delta T_\varepsilon + \Delta T_\rho \end{aligned} \tag{1.1}$$

To determine the *true* temperature T , first the parasitic reflectance I_ρ has to be

eliminated from Eq. 1.1, otherwise it contributes a temperature error ΔT_ρ . Second, the detected thermal self-emission I_ε contains two unknown quantities — ε and T . To determine T from \hat{I} , ε has to be provided. Since for many materials $\varepsilon(\lambda, T, \theta)$ is a function of temperature, wavelength, direction of observation and surface condition, it is not always feasible to determine the exact value with accuracy based on *a priori* measurement or assumptions. Hence, $\varepsilon(\lambda, T, \theta)$ has to be measured *in-situ*, otherwise a temperature error ΔT_ε is incurred.

Especially when the sample is embedded in an environment where it is exposed to intense and time-dependent irradiance ($I_0(t)$), there is a dynamic balance between absorption, reflection and emission that affect its thermodynamic state (T) and the measurement process (\hat{T}). Specifically, three distinct pathways contribute to the response signal of the radiometric sensor (Fig. 1.1). The gain of each pathway is determined by the surface absorptance (α), reflectance (ρ) and emittance (ε). $\alpha(t)$ determines how strongly the surface taps into the concentrated flux and thus mediates its equilibrium true temperature $T(t)$. $\varepsilon(t)$ determines how strongly the surface communicates its true temperature $T(t)$ to its surroundings in the form of thermal self-emission. $\rho(t)$ determines the reflected component strength. Temperature variations induced by changes in $I_0(t)$ have the effect of simultaneously varying the relative contribution of all individual pathways to the response variable. Hence, the two branches contribute time-dependent, correlated errors of reflectance ($\Delta T_\rho(t)$) and emissivity ($\Delta T_\varepsilon(t)$) to the output that mask the true temperature $T(t)$. Due to Kirchhoff's law of thermal radiation ($\alpha(t) = \varepsilon(t) = 1 - \rho(t)$), *in-situ* detection of $\rho(t)$ serves to both filter out the parasitic reflectance and calculate emissivity. Based on these two steps, the true temperature $T(t)$ can be inferred.

In many industrial applications, the parasitic effect of I_0 can be neglected and the main source of uncertainty is the unknown surface emissivity $\varepsilon(\lambda, T)$. This is reflected in the related literature, where the most generic and widely reported methods aim at eliminating the emissivity error. On the other hand, elimination of ΔT_ρ shifts into focus, when measurements are attempted in environments where the target is exposed to intense radiative flux and hence the parasitic reflectance becomes a significant source of error. This is the case in concentrated solar power facilities.

1.3 Temperature measurement in concentrated solar power facilities

Concentrating solar power (CSP) facilities concentrate the sun's energy to heat a receiver to high temperatures. This heat is then used to either operate a con-

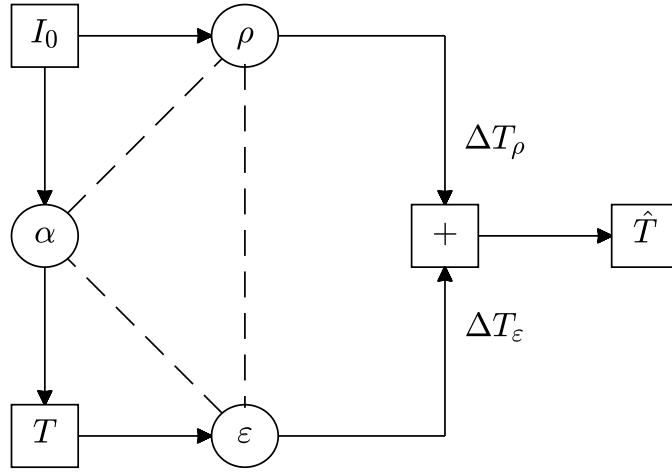


Figure 1.1: Pathways affecting the response \hat{T} of a radiometric sensor. The true temperature T is affected by surface absorbance α , while the magnitude of thermal emission for a given temperature T is determined by surface emittance ε . ρ determines the magnitude of reflected radiation. For opaque samples, Kirchhoff's law of thermal radiation holds and $\alpha = \varepsilon = 1 - \rho$ (dotted lines).

ventional heat engine for electricity generation or to drive a chemical reaction for production of solar fuels. CSP facilities may be classified in terms of their intended use into production facilities, such as solar towers and solar troughs, and research facilities, such as solar furnaces and solar simulators. A solar tower facility comprises an array of plane heliostats that are configured to concentrate the dilute solar irradiance on to a common focal point (Fig. 1.2a). The tower provides physical access to the focal point, so that a solar absorber driving a heat engine or a cavity reactor can be mounted. The field of CSP has advanced through experiments that are typically conducted in solar furnaces and solar simulators.

Solar furnaces

Solar furnaces serve as experimental platforms for conducting research in high-temperature material-testing and thermo-chemistry under conditions of concentrated flux. In a solar furnace (Fig. 1.2b), a heliostat deflects the dilute solar radiance onto a paraboloidal concentrator that focuses the solar light to a fixed location, where the experimental setup is mounted [14–19]. Shutters placed be-

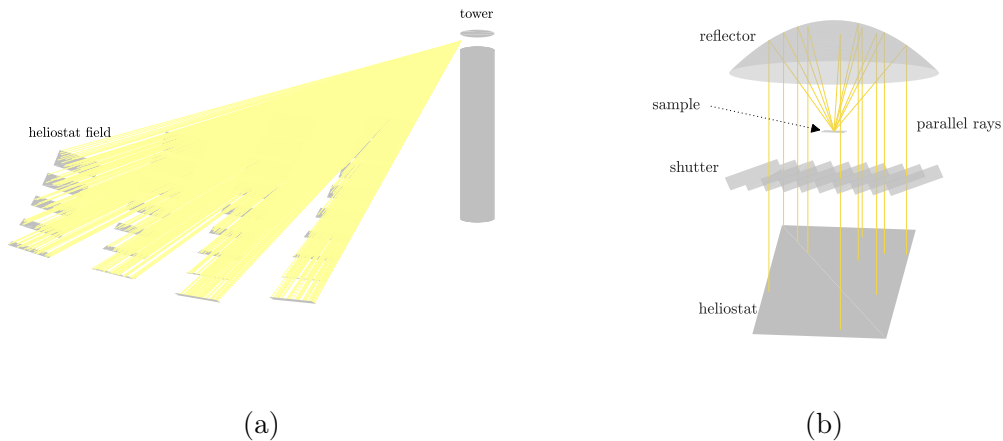


Figure 1.2: Natural sunlight concentrating facilities. (a) Solar tower facility. (b) Research grade solar furnace facility comprising a plane heliostat, a paraboloid concentrator and motion-controlled shutters to regulate the solar flux I_0 .

tween the heliostat and the concentrator are used to regulate the solar flux. In the high flux solar furnace at PSI, 40 kW of solar power can be collected and concentrated. The attained peak flux exceeds 5 MW/m^2 [16], corresponding to a sunlight concentration factor of about 5000 suns [1 sun= 1 kW/m^2]. The high-flux solar intensity provides a rapid, intense external heat source that can be used to study material properties [20–22] under high heating rates or for conducting fast high-temperature reactions in controlled atmospheres. Solar furnaces have been used to study the production of solar fuels at high temperatures [16, 23, 24] and chemical commodities, the thermal recycling of waste materials[25] as well as testing of ceramic materials [18].

Solar simulators

To accelerate research and development efforts in the field of solar thermochemistry, one would ideally opt for an experimental platform that supports experiments under controlled, reproducible, weather-independent conditions. This is the motivation behind the increased use of *artificial* concentrated sunlight. The facilities that encompass the artificial light source, concentrating optics, and instrumentation are known as high-flux solar simulators (HFSS).

In the last decade, significant research activity has developed using solar simulators[26–38]. For a comprehensive review, see [39]. In these facilities, the materials and devices under test are exposed to concentrated radiation whose spectrum approximates the terrestrial solar spectrum. Due to these characteristics, they are an important tool for solar concentrated research and serve as testbed for prototype

testing of novel solar technologies.

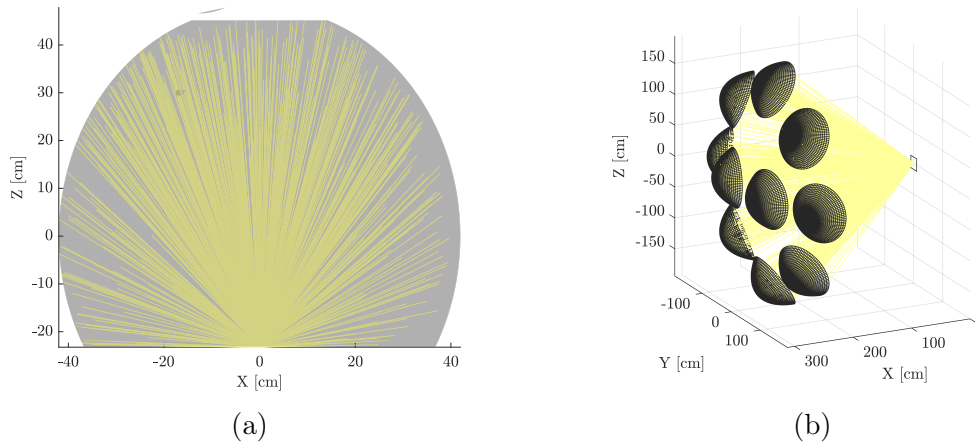


Figure 1.3: Artificial CSP facilities. (a) Schematic of the building block of a solar simulator, showing the light beam converging on the secondary focus. (b) A multi-source solar simulator containing 10 lamp-reflector modules whose secondary focal points coincide.

Solar simulators are usually built from several modules. Each module consists of a point-like, bright, broadband and non-collimated radiation source — typically a Xe short arc lamp — positioned at the primary focal point of an ellipsoidal specular reflector (Fig. 1.3a). Radiation emanating from the source converges to the conjugate focus where the experiment is conducted. Multi-source high-flux solar simulators [33, 40] utilize an array of such modules that are oriented so that their conjugate foci coincide (Fig. 1.3b). Flux densities equivalent to concentration ratios of several thousands suns can be attained at the common focus.

Temperature measurement in CSP

Accurate determination of the surface temperature of irradiated matter during experiments in CSP facilities [41] is important for the purpose of material characterization, process control, reactor design and to better understand the effects of light and heat on the ensuing chemical processes.

Thermocouple measurements do not provide accurate information: First, the probe cannot be placed directly at the exposed surface, because it would be either destroyed due to the concentrated flux or biased — unless its optical properties exactly matched the absorptivity of the target. Second, the high temperatures of 1000 K – 3000 K attained in the vicinity of the focal point may cause probe degradation. Third, the steep spatial temperature gradients may cause significant measurement bias, even if the probe is embedded close to the surface.

Conducting non-contact measurements by sampling the thermal radiation is the method of choice, but the measurement is distorted by the parasitic reflectance. During a dynamic experiment in a solar simulator, samples are exposed to concentrated irradiance $I_0(\lambda)$. The parasitic reflectance term (I_ρ) is a significant fraction of radiosity. It is also *time-dependent* since ρ varies as a function of temperature and potentially due to chemical reactions or phase transitions, and so does I_ρ . Hence, the resulting $\Delta T_\rho(t)$ can severely distort the measured temperature. In addition, dynamic experiments are conducted with operating temperatures that typically span 1000 K resulting in a varying I_ϵ . Since both I_ϵ and I_ρ may vary by several orders of magnitude with wavelength and temperature, so does the relative contribution of ΔT_ρ and ΔT_ϵ . The combination of these two dynamic error sources, if not accounted for, may greatly distort the measurement process.

In *natural* sunlight concentrating facilities, $I_0(\lambda)$ bears the characteristics of the terrestrial solar spectrum, where $I_0(\lambda) \rightarrow 0$ for selected wavebands as a result of atmospheric absorption (Fig.1.4). Selecting an operating wavelength that coincides with one of these wavebands where I_ρ becomes negligible serves to eliminate ΔT_ρ . This is the basic principle of solar blind pyrometry (SBP) [41–46]. While SBP is widely used in *natural*-light CSP due to its simplicity, it suffers from the adverse effects of emissivity uncertainty and variable attenuation of the thermal signal along the measurement path. Furthermore, the principle of SBP is not feasible in solar simulators because I_ρ exhibits a continuous distribution of intensity over wavelength, due to the continuous xenon-arc lamp's spectrum.

The only documented method that could be applied for temperature measurement under the conditions imposed by operating characteristics of solar simulators is the Flash-Assisted Multi-wavelength Pyrometry (FAMP) [42, 49–52]. FAMP is a powerful method that enables the simultaneous and in-situ determination of true temperature, sample reflectance and solar irradiance in the presence of intense external radiation. Nevertheless, it requires a complex experimental setup and elaborate calibration: First, the use of a cold, white, lambertian reference target of known reflectance ρ^{ref} should be exposed to the same radiative flux (I_0) as the sample of interest for the duration of the measurements. Second, an external light source is required - an electric flash whose intensity I_{flash} should be strong enough to be detected when it is superimposed on the concentrated irradiance (I_0). These requirements restrict the applicability of the method. Hence, it is worthwhile to investigate alternative routes to solving the temperature measurement problem. In this work, a method is developed that combines the simplicity of SBP with the capability of FAMP to measure temperature and reflectance.

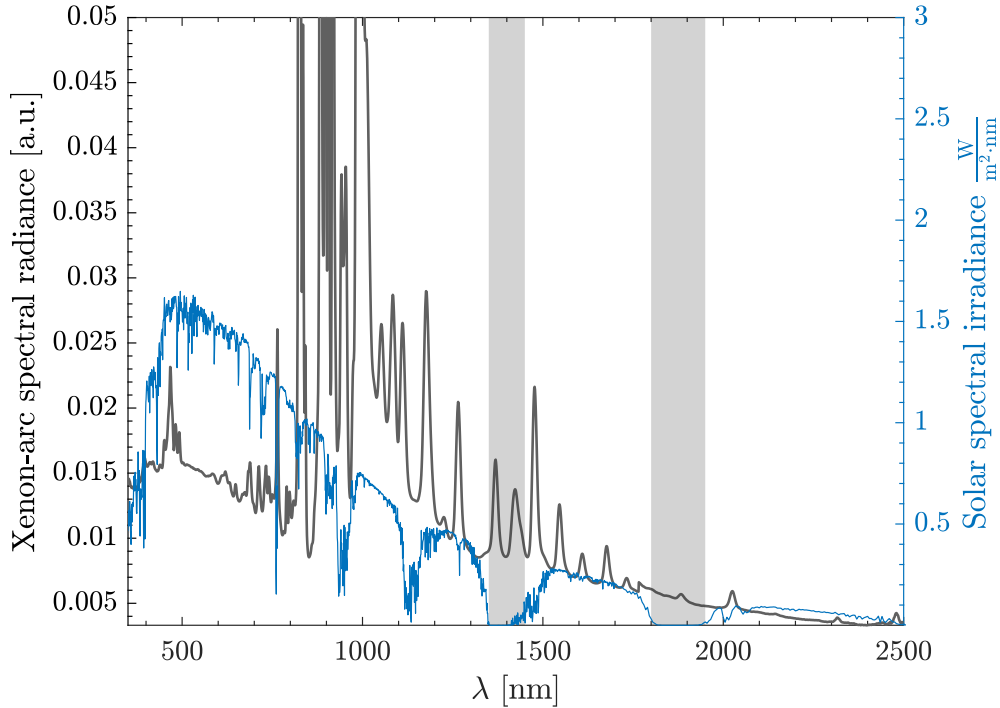


Figure 1.4: Comparison between the Air Mass 1.5 terrestrial solar spectrum [47] and the spectrum of the xenon-arc lamp — data obtained from [48] — that is typically used as the light source in high-flux solar simulators. Spectral bands where the solar spectrum is attenuated are indicated by the shaded area.

Double modulation pyrometry

The operating principle of DMP is illustrated in Fig. 1.5: DMP measures thermal emission indirectly as the difference of the directly detected radiosity ($\rho \cdot I_0 + I_\varepsilon$) and reflectance ($\rho \cdot I_0$) signals.

DMP modulates at ω_1 the irradiance (I_0) prior to it reaching the surface, then collects and modulates at ω_2 the surface radiosity ($\rho \cdot I_0 + I_\varepsilon$) — consisting of the sum of thermal (I_ε) and *modulated* reflected (I_ρ) components. The modulated composite optical signal is spectrally filtered and detected. The detector output is fed in parallel to two lock-in amplifiers (LIA). LIA₁ — phase-locked at ω_1 — detects the reflected irradiance ($\rho \cdot I_0$), while LIA₂ — phase locked at ω_2 — detects the radiosity ($\rho \cdot I_0 + I_\varepsilon$). Hence, DMP detects directly the radiosity and reflectance signals. The thermal emission can thereby be extracted as the difference of the two signals.

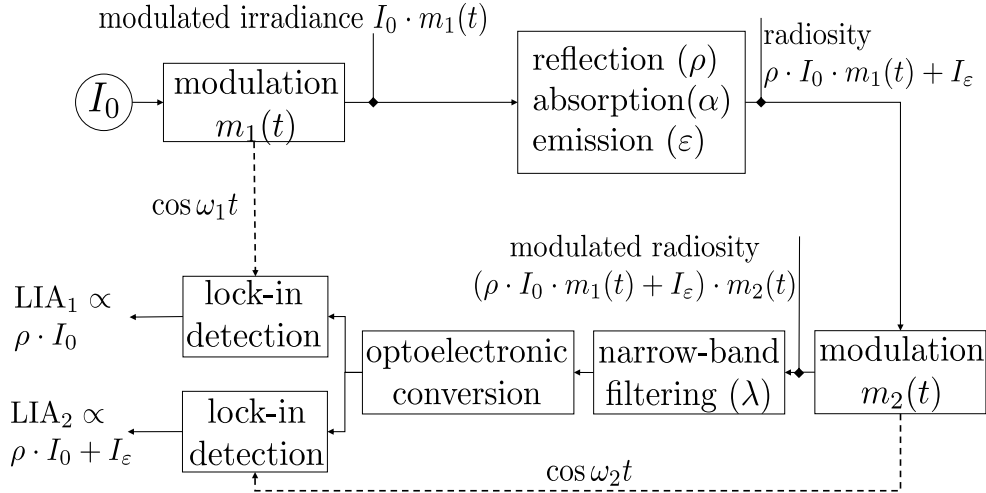


Figure 1.5: The basic principle of double modulation pyrometry (DMP): modulation of the intensity of irradiance $I_0(t)$ and lock-in detection of the reflected fraction $\rho \cdot I_0(t)$.

1.4 Thesis outline

The motivation of the thesis is to enable accurate measurement of surface temperature for opaque samples of arbitrary reflectance $\rho(\lambda, T)$ that are exposed to concentrated irradiance (I_0) and undergo dynamic experiments in solar simulator facilities. This implies developing a methodology to eliminate the reflectance $\Delta T_\rho(t)$ and emissivity $\Delta T_\varepsilon(t)$ errors.

In chapter 2, a brief review of methods and applications of pyrometry is provided. First, general purpose methods that aim at eliminating the emissivity error (ΔT_ε) are reviewed, and later specialized methods — mainly developed within the field of concentrated solar power — that tackle the reflectance error are presented. In chapter 3, the general background of radiometric measurements and the theory of double modulation pyrometry (DMP) are delineated to facilitate understanding of the results presented in subsequent chapters.

In chapter 4, the development of a prototype in a small-scale solar simulator facility is demonstrated. Implementation of amplitude modulation by superimposing a sinusoidal signal on the voltage supply of the light source is investigated and rejected on the basis that this *electronic* modulation can only modulate the arc radiation but not the thermal radiation of the electrode that accounts for 40% of emitted energy. Modulation by means of a mechanical component is implemented: A rotating blade that utilizes the symmetry of the light-source reflector is custom-

designed and built. The two-step calibration methodology is developed and the error contribution of the calibration coefficients is analyzed by Monte-Carlo simulation. The performance of the method is assessed on a high reflectance Platinum sample and verified by measurements of its melting point.

In chapter 5, the design and implementation of a DMP prototype in a multi-source high-flux solar simulator facility is presented and the methodology for correction of the emissivity error is outlined. It relies on *in-situ* measurement of reflectance that is used in the indirect determination of emissivity, that is in turn used to obtain an estimate of the true temperature. On-line measurements of temperature and reflectance are obtained on ceramic samples (Al_2O_3 , ZrO_2 , SiC) that exhibit temperature dependent optical properties. The two time-dependent error contributions $\Delta T_\rho(t)$ and $\Delta T_\epsilon(t)$ are separated and analyzed.

In chapter 6, DMP is applied in a natural-sunlight concentrating facility to experiments on a series of metallic and ceramic samples and compared against the de facto method of solar blind pyrometry (SBP). Temperature is determined by analyzing the thermal radiation at several operating wavebands, while the *in-situ* measurement of reflectance under the varying solar irradiance is obtained by utilizing the available measurements of direct normal irradiance (DNI).

In chapter 7, the most important findings of the thesis are summarized and further enhancements of the method are proposed that relate to improvements of the temperature calibration and the utilization of concurrent multi-wavelength measurements.

Chapter 2

An overview of pyrometric methods

In this chapter an overview of pyrometric methods along with a short summary of specific applications is provided. In addition, Table 2.1 summarizes the temperature range and accuracy of the various method implementations. Note that the reported temperature ranges and errors are dependent on implementation and samples tested and do not characterize the methods themselves. The pyrometric methods can be classified (Fig. 2.1) in terms of whether they can eliminate the emissivity (ΔT_ε) or reflectance errors (ΔT_ρ).

2.1 Elimination of ΔT_ε

The main source of uncertainty in many industrial applications of pyrometry is the unknown emissivity of the surface $\varepsilon(\lambda, T)$. The pyrometric methods developed to address the emissivity error can be subdivided into *active* methods that utilize an additional source of monochromatic or broadband radiation to probe the sample in order to obtain information about surface emissivity, and *passive* methods that determine temperature solely by detecting and analyzing the thermal radiance in combination with a set of assumptions about the wavelength dependence of emissivity.

2.1.1 Ratio pyrometry

Ratio pyrometry [8] is a passive method that infers the temperature of an object by measuring the *ratio* of spectral radiances $I_{\lambda_1}/I_{\lambda_2}$ at two distinct wavelengths λ_1 and λ_2 . Ratio pyrometry relaxes the requirement of knowing the absolute value of $\varepsilon(\lambda, T)$: As long as the emissivity ratio at the two wavelengths $\varepsilon_{\lambda_1}/\varepsilon_{\lambda_2}$ is a known constant, the true temperature can be determined, without knowing the absolute values. Assuming that the ratio is temperature independent, T can be

Method	Temperature Range	Accuracy/Error
Ratio pyrometry	1000 – 2500 K [8]	$\approx \pm 50 - 100$ K [8]
Multi-wavelength pyrometry	2000–5000 K[53] 1200–2600 K[54]	2%–10%[53] average error 0.5% [54]
Polarization pyrometry	$\approx 1600 - 2200$ K [55]	± 70 K [55]
Pyro-reflectometry	$\approx 900 - 1200$ K (Pr_2O_3)[56] $\approx 1000 - 4000$ K (Dy_2O_3)[56] $\approx 800 - 2300$ K [57] $\approx 800 - 1400$ K [58] > 800 K [59]	— — 2%-6% [57] 0.5%–1% [58] < 5% [59]
Solar blind pyrometry	$\approx 1000 - 2400$ K (Al_2O_3)[43] $\approx 1100 - 1400$ K [44] $\approx 850 - 1600$ K [46] $\approx 450 - 1600$ K [41]	— $\pm 0.7\%$ [44] 5% at 1223 K [46] $\approx 5\%$ [41]
Short-wavelength pyrometry	$\approx 1593 - 1773$ K (Black-body)[60] $\approx 1773 - 2673$ K (Magnesia) [60]	$\pm 0.5\%$ [60] < 5% [60]
FAMP	$\approx 1000 - 2000$ [52]	$\approx \pm 2 - \pm 6$ K [52]

Table 2.1: Operating range and accuracy of pyrometric methods. Operating range is based on reported experiments. Also the magnitude of the errors depends greatly on implementation (hardware) and sample properties (diffuse, specular) – not only on methodology.

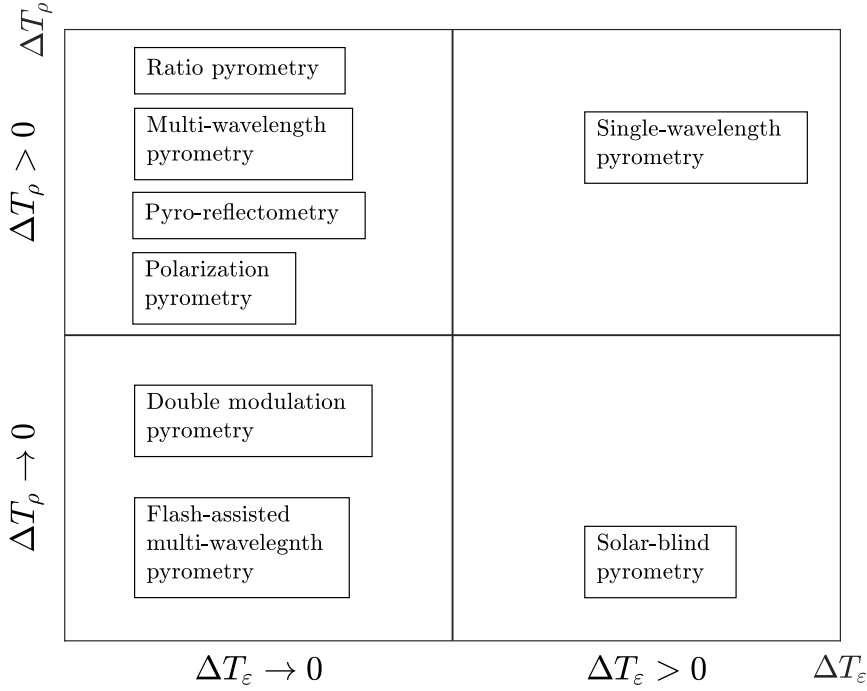


Figure 2.1: A classification of pyrometric methods in four quadrants with respect to their ability or not to eliminate any of the parasitic reflectance (ΔT_ρ) and emissivity (ΔT_ε) errors. At the right half plane fall methods that do not have the ability to measure or infer emissivity but rather require that ε be provided as external input. Hence, they are exposed to ΔT_ε . The upper half plane is occupied by methods that do not have any built-in measures to eliminate parasitic reflectance. Hence, they are exposed to ΔT_ρ .

determined without explicit knowledge of ε . In the simplest case, the ratio can be assumed to be 1 (gray body assumption). In some practical applications, such as measurements of high temperature ceramics, this assumption might be simplistic since emissivity is wavelength dependent.

Taking the logarithm of the ratio of Planck's law, with Wien's approximation ($(c_2/\lambda T) \gg 1$), we obtain a relation [8] between the detected quantities (I_{λ_1} , I_{λ_2}) and the unknown temperature T :

$$\ln \left(\frac{I_{\lambda_1}}{I_{\lambda_2}} \right) = \ln \left(\frac{\varepsilon_{\lambda_1}}{\varepsilon_{\lambda_2}} \cdot \left(\frac{\lambda_2}{\lambda_1} \right)^5 \right) + \left(\frac{c_2}{\lambda_2} - \frac{c_2}{\lambda_1} \right) \frac{1}{T} \quad (2.1)$$

where $c_1 = 1.191 \times 10^8 \text{ W}\cdot\text{sr}^{-1}\mu\text{m}^4\cdot\text{m}^{-2}$ and $c_2 = 1.439 \cdot 10^4 \mu\text{m} \cdot \text{K}$ are Planck's

first and second radiation constants.

When designing a ratio pyrometer, there is a trade-off associated with the selection of the relative position of λ_1 and λ_2 . The gray body assumption is more likely to hold true when λ_1 is close to λ_2 . Hence, it is desirable to locate λ_1 and λ_2 as close as possible. For example, the center wavelengths of the narrow band filters in [8] were selected so that $\lambda_1 = 710$ nm and $\lambda_2 = 810$ nm. On the other hand, as $\delta\lambda \rightarrow 0$, the sensitivity of the instrument to temperature changes decreases (Eq. 2.1). The signal-to-noise ratio is improved by increasing the quantity $|1/\lambda_2 - 1/\lambda_1|$. The use of ratio pyrometry to determine the temperature of particles combusting in air has been extensively documented [8, 61]. Ratio pyrometry offers an advantage when measuring across a glass window, since the effect of transmission cancels out [61], assuming that glass transmissivity is constant for λ_1 and λ_2 .

2.1.2 Multi-wavelength pyrometry

Multi-wavelength pyrometry (MWP) [5, 53, 54, 62–65] refers to a class of techniques developed to address the emissivity error. Their common feature is that they combine measurements of thermal emission at more than one wavebands with a set of assumptions about the functional form of emissivity ($\varepsilon(\lambda)$) of the measured surface in order to determine the true temperature. MWP uses interpolation [54] or curve-fitting [63] on multiple spectral radiance measurements to determine the temperature without prior knowledge of emissivity. MWP techniques are *passive* in that they attempt to determine optical properties without utilizing external light sources to probe the target surface.

In MWP the spectral radiance is collected and spatially dispersed to $n > 1$ detectors, with detector i detecting photons within narrow band centered at λ_i . The n concurrent measurements yield a system of n equations,

$$I_i = k_i \cdot \varepsilon_i \cdot I_{\text{bb}}(\lambda_i, T), \quad i = 1, \dots, n \quad (2.2)$$

where I_i are the measured intensities, k_i is the *known* calibration coefficient for channel i , $\varepsilon_i := \varepsilon(\lambda_i, T)$ is the *unknown* emissivity at channel i , and I_{bb} is the black-body spectrum.

Determination of T by solving the system of n equations (Eq. 2.2) is not possible due to the $n + 1$ unknowns ($\{\varepsilon_1, \dots, \varepsilon_n, T\}$). MWP methods utilize a set of assumptions about $\varepsilon(\lambda, T)$ to render the system of Eq. 2.2 determined. MWP assumes that the emissivity spectrum ($\varepsilon(\lambda, T)$) is a smooth function of wavelength [66] and can be approximated by a parametric model (linear, polynomial, exponential, logarithmic) with a reduced number of parameters $p \leq n - 1$, i.e. $\varepsilon(\lambda) \approx f_p(\lambda)$ [62].

Based on the relation between the number of free parameters (p) in the emissivity model and the number of available measurements (n), MWP methods can be broadly divided in interpolation-based ($p = n - 1$) and least-squares fitting ($p \ll n$) techniques [54]. The interpolation-based technique ($p = n - 1$) proposed by Svet uses a polynomial to approximate ε , and Lagrangian interpolation to determine T and ε_i [65]. Coates [62] showed that this approach shows poor performance, with errors increasing with the number of wavebands due to overfitting. An improved approach [63, 65] is to increase n , so that $p \ll n$, and use curve fitting to estimate the p coefficients. It has been reported that [53, 67] that any statistical improvement by increasing n to over-determine the system of equations is marginal. In [53] it was assumed that $\ln \varepsilon$ varies linearly with wavelength. See [53] for the mathematical development of that approach. A linear or log-linear $\varepsilon(\lambda)$ has been typically assumed in the application of MWP to measurements in steel [67] and aluminum [68] samples. Hoch et al. [69] measuring with a six-wavelength pyrometer used a model where the radiance temperature varies linearly with wavelength.

MWP suffers from several drawbacks. First, for materials whose optical properties have not been studied, it may be difficult to ascertain that a particular parametric model is a good approximation of the emissivity function. Second, any deviation of the assumed emissivity model from the true spectrum introduces a systematic error that propagates into temperature. Since, the true spectrum is unknown, it is difficult to estimate the emissivity error and the resulting temperature uncertainty, and hence the quality of the measurement cannot be assessed.

To address this limitation, a multi-wavelength pyrometer with a self-verifying feature was implemented [5]. It records radiance values (I) in 400 narrow-band channels spanning a wide spectral range in the IR region ($0.5\mu\text{m}$ - $2.5\mu\text{m}$). Planck's law can be rearranged into the following form:

$$y(I, \lambda) = \frac{1}{T} - \frac{\lambda}{c_2} \ln(\varepsilon(\lambda)) \quad (2.3)$$

where the left hand side $y(I, \lambda)$ is obtained by applying to the observed spectra I the following transformation:

$$y(I, \lambda) = \frac{\ln(c_1/\lambda^5/I)}{c_2/\lambda} - \frac{\ln(1 - \exp(-c_2/\lambda/T))}{c_2/\lambda} \quad (2.4)$$

Subsequently, the transformed intensity values y , acquired over a wide spectral range, are plotted versus λ . In regions where emittance is spectrally independent, the factor $\ln \varepsilon(\lambda)$ in Eq. 2.3 is constant and hence the $y(I, \lambda)$ data plotted against λ fall on a straight line with slope $\ln \varepsilon/c_2$. This serves as a confirmation that the material's emissivity is spectrally independent [5] within that spectral region.

Both emissivity and temperature can then be obtained by fitting the straight-line measurements over that particular region. Specifically, according to Eq. 2.3, emissivity can then be obtained from the slope and temperature from the inverse of the intercept of the straight line.

Combustion and Aerospace Applications

Knowledge of true temperature is required in the analysis and optimization of combustion systems. Since, temperature is linked to ignition, burnout and evolution of emissions [7], pyrometric measurements provide valuable data to understand the physics of flame and emission during combustion, and to quantify combustion efficiency. Typically, multicolor pyrometry has been used to determine flame and soot temperatures in a diesel combustion process [10].

Pyrometry finds extensive use in aerospace applications as a characterization and diagnostic tool. Multi-wavelength pyrometry [5] has been employed to measure the surface temperature and emissivity of coating materials used in the development of thermal barrier coatings for atmospheric reentry vehicles. MWP [5] was also used to indirectly measure the temperature of combustion gases at the exhaust path of a turbomachinery combustor, where the high temperatures of about 2300 K exceed the working temperature of platinum thermocouples, while thermocouple materials — such as tungsten and rhenium — that can withstand the high temperatures would be easily oxidized in the environment of the hot gases [5]. A BeO tubular probe was placed in the path of the exhaust gas, and thermal radiation from the probe's internal walls was coupled via an optical fiber to the detector, allowing to determine the temperatures of the hot gases. Using the method [5], real-time temperature measurements of the combustor exit of a jet engine were obtained. Such information can be fed as input into an active engine control system [5].

The performance of aircraft and gas turbine engines is dependent on operating temperature [12]. On the one hand, to attain high-efficiency and performance during operation, turbine engine design is steered towards higher operating temperatures, where highly performant ceramic materials, such as ZrO_2 , are used as thermal coatings in turbine engine components. During the development and testing cycle, pyrometry can be used to obtain temperature and emittance information [5] to characterize the novel system. On the other hand, during operation, real-time temperature measurements are required to diagnose and avoid over-heating of turbine components. Most commonly, a single, broad-band silicon detector is used to detect the average blade temperature and this information is fed to the digital engine controller that can regulate fuel flow to the combustor in order to limit the operating temperature [12].

2.1.3 Multi-wavelength pyrometry with reflectance measurement

Gardner et al. [70] developed a multi-wavelength pyrometer, where an external light-source is used to irradiate the sample under a small solid angle at a polar angle θ' from normal and the reflected component is detected at θ . The reflected component is amplitude modulated at ω , while the thermally emitted component is modulated at $2 \cdot \omega$. Hence, the reflected component can be decoupled from the emitted component and both can be measured. First, at each of the n wavelengths, measurements of both the thermal radiance and of the directional-directional spectral reflectivity ($\rho_{\theta',\theta}(\lambda)$) are obtained. Second, the hemispherical-directional reflectivity is expressed as $\rho_{\square,\theta}(\lambda) = G \cdot \rho_{\theta',\theta}(\lambda)$, where G is an unknown wavelength-independent constant. Third, the directional emissivity is expressed as $\varepsilon_\theta(\lambda) = 1 - \rho_{\square,\theta}(\lambda)$ — based on Kirchoff's law. The basic assumption of the method is that G is wavelength-independent, i.e. the variation of the directional-directional reflectivity with wavelength is the same as the variation of the total reflectivity. Substituting the expression of $\varepsilon_\theta(\lambda)$ into the system of equations of multi-wavelength pyrometry (Eq.2.2) we obtain,

$$I_i = k_i \cdot (1 - G \cdot \rho_{\theta',\theta}(\lambda)) \cdot I_{\text{bb}}(\lambda_i, T), \quad i = 1, \dots, n \quad (2.5)$$

where there are now only two unknown quantities, G and T . Hence measurements at a minimum of $n=2$ wavelengths are sufficient to formulate a determined system of equations.

Semiconductor Manufacturing

Effective process characterization in semiconductor manufacturing can be attained by using pyrometry to determine the temperature, optical properties and film thickness of semiconductor wafers. In the case of chemical vapor deposition (CVD) and molecular beam epitaxy (MBE), the *in-situ* measurement of temperature and optical properties of wafer surface enables effective on-line process control and quality assurance, improving yield and throughput.

In most MBE systems, where pyrometers are typically used to determine wafer temperature, accuracy is limited by the fact that wafer surface does not behave as a black-body. Hence, knowledge of the emittance value is required to improve measurement accuracy. Furthermore, the optical properties of the wafer surface vary during the process of hetero-epitaxial growth. Hence, *in-situ* time-resolved measurements of emittance are required to attain accurate temperature results.

A pyrometric method that incorporated *in-situ* reflectance measurement was developed to measure the temperature of semiconductor wafers [71] during MBE, where hetero-epitaxial growth causes the emissivity of the wafer surface to vary

with time. Radiance and reflectance measurements were obtained interchangeably by use of a computer controlled mirror that allowed switching between pyrometry and reflectance modes. Reflectance measurements were obtained by use of a xenon arc lamp coupled to a monochromator centered at 925 nm. Based on the principle of detailed balance for specular, opaque samples ($\varepsilon(\lambda) + \rho(\lambda) = 1$), the reflectance measurements were used to calculate emissivity. The thermal emission was also measured at 925 nm and was combined with the emissivity calculation to determine the true temperature. Note that the operating wavelength of 925 nm was selected such that the GaAs and InP substrates are opaque, so as to avoid thermal signal from the holder being transmitted through the sample.

Another in-situ method for the simultaneous measurement of film thickness and temperature of a silicon wafer during thermal oxidation is Multiwavelength Pyrometric Interferometry (MWPI) [72]. The method offers high-resolution (0.1 nm for thickness and 0.025 K for temperature) real time measurements valuable for process control and for monitoring the growth of both single films and multilayer structures.

The experimental setup consists of a process chamber containing the heated substrate covered by a growing film of thickness $d(t)$ and temperature $T(t)$. The emitted thermal radiation is amplitude-modulated by a chopper and collected by a lens. The beam is then split in two branches that are spectrally filtered at $\lambda_1 = 952.4$ nm and $\lambda_2 = 751.2$ nm and form an image of the wafer on two IR-sensitive detectors. The detector signals are processed by two lock-in amplifiers.

Thermal radiation emitted from the substrate is refracted and reflected at the interfaces of the growing film. To avoid explicitly analyzing the effects of that interference, the method considers the emissivity of the whole system (substrate and film). Hence, the dependence of detector signal on film thickness and temperature is expressed as

$$I(d(t), T(t), \lambda) = K \cdot \varepsilon(\lambda, d) \cdot I_{\text{bb}}(\lambda, T) \quad (2.6)$$

where K is a calibration constant that encompasses all optical, geometric and electronic influences of the instrument. Most importantly ε is the emissivity of the *whole* system — substrate covered by the growing film. As such, ε depends on the complex index of refraction of the film and the optical constants of the substrate, film thickness, temperature, wavelength and angle of observation. Since the covered substrate is not transmitting, emissivity can be calculated based on Kirchoff's law by calculating its reflectance [72]. The method was used to study the growth of SiO₂ film on Si during thermal oxidation and report film thickness and temperature as function of time.

2.1.4 Pyroreflectometry

Pyroreflectometry [56–59, 73] is an active method developed at CNRS that utilizes concurrent measurements of thermal radiance and bi-directional spectral reflectivity in order to determine the emissivity and temperature of the observed surface. Various implementations of the method have been developed that include operation either in two or three wavebands, in the near infrared spectral band. Emissivity is determined indirectly by measuring the bi-normal spectral reflectivity at two wavelengths. At each wavelength λ_i , a laser diode operating at λ_i extracts the bi-normal reflectivity $\rho_{\perp\perp}(\lambda_i, T)$. When the laser diode is off, the pyrometer detects at each wavelength λ_i — as a conventional pyrometer would — the thermal radiation $I(\lambda_i)$ emitted from the sample, from which the radiance temperature $T_r(\lambda_i)$ can be determined. When the laser diode is on, the sum of thermal emission and laser reflection emanating from the sample is detected. In addition, measurements of laser reflection from a reflectivity reference standard observed under the same geometric conditions are taken. By subtracting the thermal signal from the radiosity signal and dividing by the reference, the bi-normal reflectivity $\rho_{\perp\perp}(\lambda_i, T)$ can be extracted [58]. Pyro-reflectometry builds on the basic assumption formulated by Gardner et al. [70] that the angular distribution of bidirectional spectral reflectivity $\rho(\lambda, \theta, \theta')$ does not vary with λ . Hence, from the measurement of the bi-normal reflectivity $\rho_{\perp\perp}(\lambda_i, T)$, it is assumed that the directional-hemispherical reflectance can be extracted by multiplying with a term $n_d(T)$ that is wavelength independent. Since $n_d(T)$ is the same for all wavelengths, a solvable system of independent equations can be formulated that for the case of two wavelengths assumes the form[74]:

$$\begin{aligned} I(T_r(\lambda_1), \lambda_1) &= (1 - \pi n_d(T) \rho_{\perp\perp}(T, \lambda_1)) \cdot I(T, \lambda_1) \\ I(T_r(\lambda_2), \lambda_2) &= (1 - \pi n_d(T) \rho_{\perp\perp}(T, \lambda_2)) \cdot I(T, \lambda_2) \end{aligned} \quad (2.7)$$

Eq. 2.7 can be solved by an iterative calculation of $n_d(T)$ values, until the true temperature T is the same for both equations. The method has been used to measure the temperature and emissivity values of the back side of samples, such as tungsten [58], whose front side is radiatively heated at the focus of a solar furnace.

Nuclear fusion reactors

In nuclear fusion devices, the temperature of plasma facing components has to be measured in order to ensure safe operation, provide diagnostic information about component fatigue, and improve our understanding of the physics of plasma - wall interactions [75–77]. So far, these components were typically made of carbon. For future designs, metallic surfaces of low and changing emissivity, such as tungsten,

are envisioned [13, 76], thereby increasing the amount of plasma glow reflected off the metallic wall. Even though pyrometry is a method of choice for the high temperature measurements needed in fusion devices, a significant measurement error is caused when observing a highly reflective target embedded in a highly radiative environment. To eliminate the effect of unknown emissivity, the pyroreflectometry method [59, 78] that was originally developed for measurements in concentrated solar applications is considered anew in the context of fusion research. To eliminate the effect of parasitic reflectance, modulated active pyrometry [79] has been proposed — an active method that relies on chopping a continuous laser beam to modulate the temperature of the target surface, thereby extracting the temperature in the presence of reflected flux.

2.1.5 Polarization pyrometry

Polarization pyrometry [80] is a passive method that addresses the emissivity uncertainty by utilizing the Fresnel formula to analyze the polarization components of thermal radiation emitted from an optically smooth surface whose roughness (σ_s) satisfies the Fresnel condition ($\sigma_s < \lambda/10$).

The spectral emissivity of a clean optically smooth surface can be derived from the complex dielectric function $\xi(\lambda) = (n - ik)^2$ via the Fresnel formula. The two polarization components of spectral intensity at an observation angle α can be written as,

$$\begin{aligned} I_p^\alpha(\lambda) &= \left(1 - \left| \frac{\xi(n, k) \cdot \cos(a) - \sqrt{\xi(n, k) - \sin^2(\alpha)}}{\xi(n, k) \cdot \cos(a) + \sqrt{\xi(n, k) - \sin^2(\alpha)}} \right|^2 \right) \times \frac{c_1}{\lambda^5} \frac{1}{e^{\frac{c_2}{\lambda T}} - 1} \\ I_s^\alpha(\lambda) &= \left(1 - \left| \frac{\cos(a) - \sqrt{\xi(n, k) - \sin^2(\alpha)}}{\cos(a) + \sqrt{\xi(n, k) - \sin^2(\alpha)}} \right|^2 \right) \times \frac{c_1}{\lambda^5} \frac{1}{e^{\frac{c_2}{\lambda T}} - 1} \end{aligned} \quad (2.8)$$

Absolute measurements of the p- and s- polarization components of thermal radiation, at a minimum of two angles α [55] are sufficient to establish a determined system of four equations, enabling the unique solution of the three unknowns T , n and k . Increasing the number of measurement angles increases accuracy in the presence of experimental errors. Emissivity can then be determined from the solution of n and k .

While application of the technique is limited to smooth surfaces that meet the Fresnel condition, the limitation may be partially overcome by red shifting the measurement wavelength so that the surface roughness remains smaller than $\lambda/10$ [55].

2.2 Elimination of ΔT_ρ

The parasitic reflectance error (ΔT_ρ) becomes significant when attempting temperature measurement in an environment of intense radiative flux, such as the one encountered in concentrated solar power research. Hence, the three main methods reported herein — solar blind pyrometry, short-wavelength pyrometry, flash-assisted multi-wavelength pyrometry — were developed to eliminate ΔT_ρ term during measurements in CSP facilities. Nevertheless, the reflectance problem is recurrent in also in combustion research, as well as in the design of instrumentation for fusion reactors.

2.2.1 Solar blind pyrometry (SBP)

SBP [41–46] is a passive method that measures at a waveband that coincides with one of the spectral bands where natural sunlight is attenuated ($I_0 \rightarrow 0$), either due to absorption by H_2O or CO_2 species in the Earth’s atmosphere or by the concentrating optics.

SBP has been widely applied to CSP experiments due to its simplicity and flexibility, but it has several limitations. First, the operating wavelength is determined by the location of atmospheric absorption bands, and cannot be adapted to the requirements of the experiment. Second, there is undesirable attenuation of the thermal self-emission along the observation path that depends on path length and ambient conditions. In particular, the intra-day variability of relative humidity contributes a non-negligible error that has to be accounted for. Calculations [60] have shown that for the case of a solar blind pyrometer, intra-day variations of relative humidity heavily affect the transmission of radiation in the optical path and could lead to a 5% temperature error, assuming a 10 m observation distance and 1.4 μm operating waveband. SBP limits the maximum measurement distance because atmospheric conditions in the optical path may distort the measurement. This is the reason why a solar blind pyrometer typically used at PSI (IMPAC pyrometer [81]) has a focal length of ≈ 50 cm. In some applications, this might be a limiting factor. For example, the geometry of the DLR solar furnace requires a measurement distance of 6- -10 m [60].

A simple method that relies on the use of two off-the-shelf solar blind pyrometers operating at different wavebands [82] was developed that allows determination of temperature and emissivity in CSP facilities that operate on natural sunlight. First, the parasitic reflectance is eliminated due to use of the solar blind-wavebands. Second, data of spectral thermal radiance are collected over a wide range of temperatures. The emittance of the sample can be assumed wavelength dependent, but independent of temperature. From analysis of the collected data after the experiment, the true temperature and emissivity can be calculated. It is

an off-line method, where temperature is determined after the observations have been collected. The convergence to the true temperature improves as the temperature range increases. Nevertheless, the validity of the assumption that emissivity is temperature independent over that extended temperature range also weakens.

2.2.2 Short-wavelength pyrometry

To minimize the influence of both parasitic reflectance and emissivity uncertainty, a pyrometer operating in the 280-292 nm spectral range has been implemented at the German Aerospace Center (DLR)[60]. The pyrometer operates in the UV spectral region where the terrestrial solar radiance is negligible. One advantage of the method is that it does not suffer from attenuation in the optical path, since UV-absorption is primarily due to ozone and hence propagation close to the earth's surface is not affected. Another advantage is the favorable emissivity to temperature error propagation as the relative temperature error (ΔT_ε) due to emissivity uncertainty ($\Delta\varepsilon$) scales linearly with the operating wavelength. In addition, temperature resolution increases, since, small changes in temperature result in large changes in spectral radiance [83, 84]. On the other hand, radiance and hence signal to noise ratio decreases with decreasing wavelength [83]. For the UV-pyrometer, the use of photomultipliers was required. It is for that reason that the prototype could measure temperatures above ≈ 1600 K. The available thermal emission signal decreases. Due to the weak thermal signal at UV wavelengths and the large measurement distance (6-10 m), the use of sensitive, low-noise opto-electronics was required. A double monochromator was used for efficient rejection of longer wavelength stray-light. The monochromator was coupled to a photomultiplier tube with limited spectral sensitivity to further suppress the unwanted long-wavelength radiation. A lock-in amplifier was used for signal detection.

2.2.3 Flash-assisted multi-wavelength pyrometry

Flash-assisted multi-wavelength pyrometry (FAMP) [42, 49–52] is an active method that was developed at the Paul Scherrer Institute to address the challenge of temperature measurement in concentrated solar facilities. It enables the simultaneous and *in-situ* determination of true temperature, sample reflectance and solar irradiance in the presence of intense external radiation, and hence the ability to infer chemical or physical changes of the surface by monitoring the reflectivity time-series

The setup (Fig. 2.2) requires a cold, Lambertian reference target of known reflectance ρ^{ref} that should be exposed to the same radiative flux (I_0) as the sample of interest and an external light source — an electric flash whose intensity I_{flash}

should be strong enough to be detected when it is superimposed on the concentrated irradiance I_0 .

The method assumes that the sample is Lambertian and that the relative spectral irradiance of the incoming concentrated solar radiation is the same both on the sample and on the reflectance reference [42] ($I_{0,\text{sample}} \approx I_{0,\text{ref}}$).

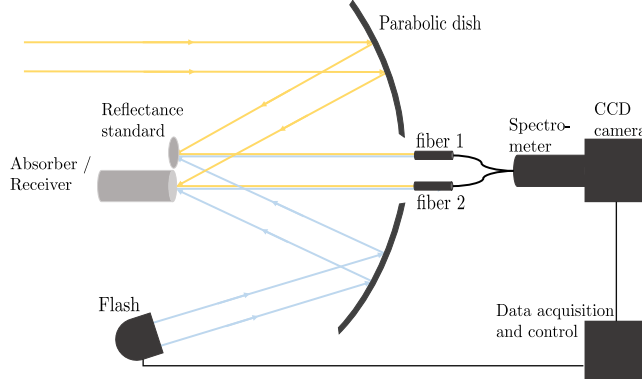


Figure 2.2: Experimental setup for the flash-assisted multi-wavelength pyrometry (FAMP). Adapted from Fig. 1 of [42].

First, prior to measurements, the ratio of the flash intensities at the location of the sample and of the reference $q_n = I_{\text{flash},n}^{\text{sample}} / I_{\text{flash},n}^{\text{ref}}$ is measured by placing a Lambertian reference target at the position of the sample. Then, spectral radiosity measurements at N wavelengths are collected from the sample and from the reference, with and without flash. Per measurement period and per wavelength n , four radiosity measurements are recorded. Without the external flash, radiosity measurements from the sample ($I_{\text{sample}}^{\text{flash}=0}$) and the reference ($I_{\text{ref}}^{\text{flash}=0}$) at the n^{th} wavelength are recorded:

$$\begin{aligned} I_n^{\text{sample,flash}=0} &= \rho_n^{\text{sample}} \cdot I_{0,n}^{\text{sample}} + (1 - \rho_n^{\text{sample}}) \cdot I_{\text{bb}}(T) \\ I_n^{\text{ref,flash}=0} &= \rho_n^{\text{ref}} \cdot I_{0,n}^{\text{ref}} \end{aligned} \quad (2.9)$$

Then, a pulse of broadband light from the electric flash is superimposed on the sample and the reference and measurements at the n^{th} wavelength are taken:

$$\begin{aligned} I_n^{\text{sample,flash}=1} &= \rho_n^{\text{sample}} \cdot I_{0,n}^{\text{sample}} + (1 - \rho_n^{\text{sample}}) \cdot I_{\text{bb}}(T) + \rho_n^{\text{sample}} \cdot I_{\text{flash},n} \\ I_n^{\text{ref,flash}=1} &= \rho_n^{\text{ref}} \cdot I_{0,n}^{\text{ref}} + \rho_n^{\text{ref}} \cdot I_{\text{flash},n} \end{aligned} \quad (2.10)$$

The sample reflectance can then be computed:

$$\rho_n^{\text{sample}} = \frac{\rho_{\text{ref}} \frac{I_{\text{sample}}^{\text{flash}=1} - I_{\text{sample}}^{\text{flash}=0}}{I_{\text{ref}}^{\text{flash}=1} - I_{\text{ref}}^{\text{flash}=0}}}{q} \quad (2.11)$$

By comparing the reflected radiance off the target and off the reference, the spectral bi-directional reflectance of the sample ($\rho_{\text{sample}}(\theta', \theta)$) is calculated. From this value, the directional-hemispherical reflectance ($\rho_{\text{sample}}(\theta', \cap)$) can be obtained assuming a Lambertian sample. Finally, for an opaque sample, the directional emissivity can be retrieved based on Kirchhoff's law.

The temperature (T) and the irradiance (I_0) can then be obtained by fitting the spectrum measured from the sample without flash ($I_n^{\text{sample, flash}=0}$) with an analytical model of the emitted and superimposed reflected external radiation.

Two modes of FAMP have been developed that both share the same operating principle outlined above. In the non-imaging mode [42, 51, 52], the temperature, as well as the irradiance and reflectance spectra at the selected spot are obtained, while in the imaging mode [49, 50] the same information is obtained for each pixel of a calibrated CCD camera. Hence, the spatial distribution of temperature, irradiance and reflectivity spectra can be obtained.

FAMP is a powerful method of absolute radiometry, but it requires an elaborate calibration procedure and a fairly complicated experimental setup: the use of an electric flash whose intensity has to be on a par with the intensity of the concentrated irradiance and the presence of a reference sample close to the hot zone.

Chapter 3

Theory

In the present chapter, first a general background of pyrometry (Sec 3.1-3.5) is provided and subsequently the theory of double modulation pyrometry (Sec 3.6-3.6.5) is formulated.

3.1 Planck's law

All objects glow (emit thermal radiation) as a consequence of their internal energy state which is macroscopically described by temperature. Spectral radiance is the radiant flux [W] that may be emitted, reflected, absorbed or transmitted by a surface per unit wavelength [nm], per unit solid angle [sr], per unit projected area [m²]. For an ideal object in thermodynamic equilibrium, the amount of thermal emission is only a function of wavelength and temperature. Planck's radiation law provides a quantitative relationship between the amount of thermal radiation $I_b(\lambda, T)$ an ideal object emits at a specified wavelength and temperature:

$$I_b(\lambda, T) = \frac{c_1}{\lambda^5} \cdot \frac{1}{\exp(\frac{c_2}{\lambda T}) - 1} \quad (3.1)$$

where $c_1 = 2\pi hc_0^2 = 3.7418 \times 10^{-16} \text{ W} \cdot \text{m}^2$ and $c_2 = hc_0/k = 1.4388 \times 10^4 \text{ } \mu\text{m} \cdot \text{K}$ are Planck's first and second radiation constants. For the range of temperature ($T < 3000 \text{ K}$) and wavelength ($\lambda < 1.5 \mu\text{m}$) examined in this thesis, it holds that $\lambda T \ll c_2$, so that the term -1 can be neglected in Eq. 3.1, leading to Wien's law,

$$I_b(\lambda, T) = \frac{c_1}{\lambda^5} \cdot \frac{1}{\exp(\frac{c_2}{\lambda T})} \quad (3.2)$$

3.2 Emissivity

The spectral radiance emitted by a real surface element within an infinitesimal solid angle is a fraction of $I_b(\lambda, T)$, i.e. of the spectral radiance a black body would emit within that solid angle. For a body at temperature T , the fraction emitted per unit area, per solid angle, per wavelength is defined as the spectral directional surface emissivity $\varepsilon(\lambda, \theta, T)$. ε is the effectiveness with which a surface is able to communicate its own internal energy with the environment. On that scale, a black body is the ideal emitter ($\varepsilon = 1$), a perfect mirror is an ideal reflector ($\varepsilon = 0$), while for real surfaces ε takes intermediate values. Note that emissivity is an intrinsic material property referring to a clean and polished surface of the material, while surface emittance incorporates sample specific surface effects such as contamination, impurities, corrugations or imprinted patterns during material processing.

The emission spectrum of a surface at temperature T is the product of the Planck $I_b(\lambda, T)$ and emittance $\varepsilon(\lambda, \theta, T)$ spectra.

A direct measurement of $\varepsilon(\lambda, \theta, T)$ is a realization of the definition of emissivity, whereby the spectral radiance emitted by the surface of interest is compared against the radiance emitted by an ideal black body.

For an opaque sample, an indirect measurement of $\varepsilon(\lambda, \theta, T)$ can be obtained by first measuring the directional-hemispherical spectral reflectivity $\rho(\lambda, T)$ and then using Kirchhoff's law $\varepsilon(\lambda, T) = 1 - \rho(\lambda, T)$.

3.3 Radiance Temperature

Here we make the distinction between radiance temperature and thermodynamic temperature of the surface. The relation is reflected in the following equation.

$$I_{\text{th}}(\lambda, T) = I_b(\lambda, T_r) = \varepsilon(\lambda, T) \cdot I_b(\lambda, T) \quad (3.3)$$

The radiance temperature $T_r(\lambda)$ is the thermodynamic temperature of an ideal black body which at the wavelength of observation λ has the same thermal footprint ($I_{\text{th}}(\lambda)$) as the observed surface. The radiance temperature ($T_r(\lambda)$) can be defined as the surface temperature of an ideal black body that if it were to be swapped with the observed surface would yield the same amount of thermal emission (I_{th}) measured by the instrument. Substituting ε from Eq. 3.3 into the inequality $\varepsilon \leq 1$, it is deduced that $T_r \leq T$. As such, $T_r(\lambda)$ serves always as a lower bound to the true surface temperature (T). The difference between T_r and T is the systematic temperature error due to the unknown emittance that we explicitly define as $\Delta T_\varepsilon = T_r - T$.

3.3.1 Radiance Equation

An explicit relation between true (T) and radiance (T_r) temperature for a surface of emittance ε at a specific wavelength λ can be derived by solving Eq. 3.3 for T , i.e. the true temperature. Note that I_b is provided by Eq. 3.1. The resulting expression is the radiance equation,

$$T = \frac{c_2}{\lambda} \cdot \ln \left(\varepsilon \cdot \left(\exp \left(\frac{c_2}{\lambda \cdot T_r} \right) - 1 \right) + 1 \right)^{-1} \quad (3.4)$$

Equation 3.4 is useful in pyrometric measurements, because it can be used to recover the true temperature T from observations (T_r) acquired with an implicit assumption of $\varepsilon = 1$, when the true ε becomes known a posteriori. Introducing the Wien approximation ($c_2/\lambda T_r \gg 1$) into Eq. 3.4, the simplified expression is derived,

$$\frac{1}{T} = \frac{1}{T_r} + \frac{\lambda}{c_2} \ln \varepsilon(\lambda, T) \quad (3.5)$$

3.3.2 Effective Emissivity

Assuming that pyrometric measurement of brightness temperature (T_r) can be associated with a known fixed point (T) of the material, then Eq. 3.3 can be solved for $\varepsilon(\lambda, T)$ to obtain an effective emissivity. Such might be the case when a pyrometer obtains radiance temperature measurements of a material undergoing phase change, and the phase change event can be located in the time-series data.

$$\varepsilon(\lambda, T_r, T) = \frac{I_b(\lambda, T_r)}{I_b(\lambda, T)} = \frac{\exp \left(\frac{c_2}{\lambda \cdot T} \right) - 1}{\exp \left(\frac{c_2}{\lambda \cdot T_r} \right) - 1} \approx \exp \left(\frac{c_2}{\lambda} \left(\frac{1}{T} - \frac{1}{T_r} \right) \right) \quad (3.6)$$

where I_b is provided by Eq. 3.1.

3.3.3 Emissivity Error ΔT_ε

A formula that expresses the temperature error as a function of emissivity error can be derived from Wien's law,

$$\frac{\partial T}{T} = \frac{\lambda \cdot T}{c_2} \cdot \frac{\partial \varepsilon}{\varepsilon} \quad (3.7)$$

The temperature error caused by emissivity error scales linearly with the operating wavelength. This suggests that the error propagation becomes favorable at shorter wavebands. For example, for a 10% emissivity error at 2000 K, a shift

in the operating wavelength from 0.9 to 1.2 would result in an approximately 30% increase of the temperature error (Fig. 3.1).

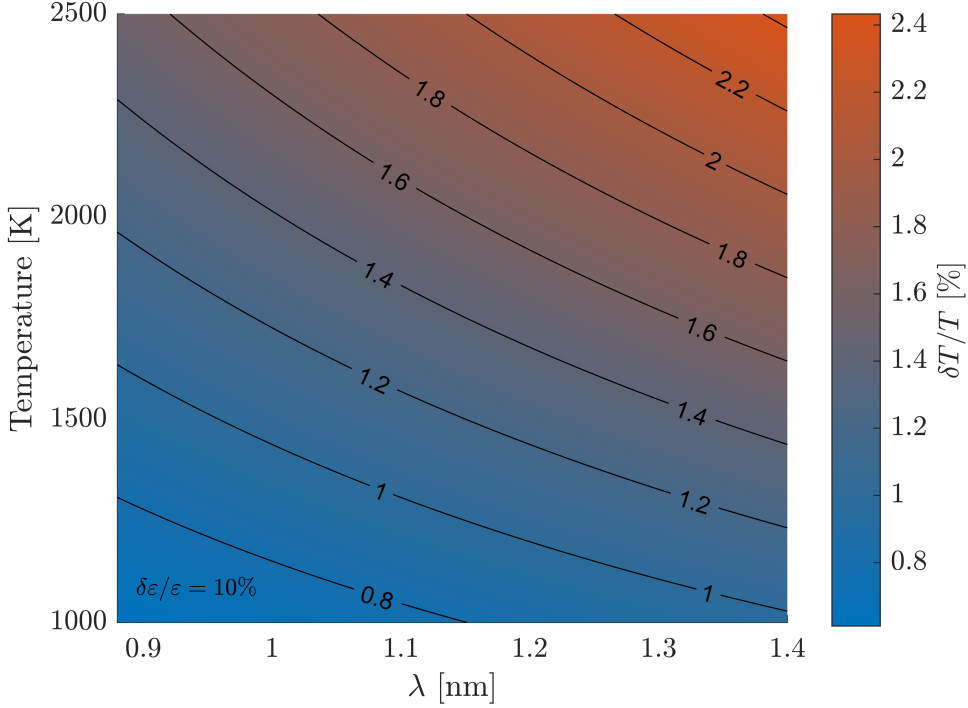


Figure 3.1: Relative temperature error $\delta T/T$ arising from a 10% error in emissivity $\delta\varepsilon/\varepsilon$, plotted as a function of wavelength and temperature.

3.4 Lambertian Surface

Lambert's cosine law states that the radiant flux per unit solid angle per wavelength (Φ [W/sr/nm]) being emitted from a unit surface (δA) exhibits a cosine dependence on the observation angle θ , where $\cos\theta = \hat{n} \cdot \hat{r}$ (see Fig. 3.2). Since the apparent surface — the projected area — also scales with $\cos\theta$, the radiant flux per unit solid angle per wavelength per unit surface (I [W/sr/nm/m²]) remains constant. Surfaces whose spectral intensity (Φ) obeys Lambert's law — and hence their spectral radiance I is independent of θ — are called *Lambertian*. A Lambertian surface reflects all incident light and appears equally bright from all viewing directions, i.e. it is an diffusely reflective surface. Such surfaces are characterized by an apparent brightness that is invariant under changes in the direction of observation.

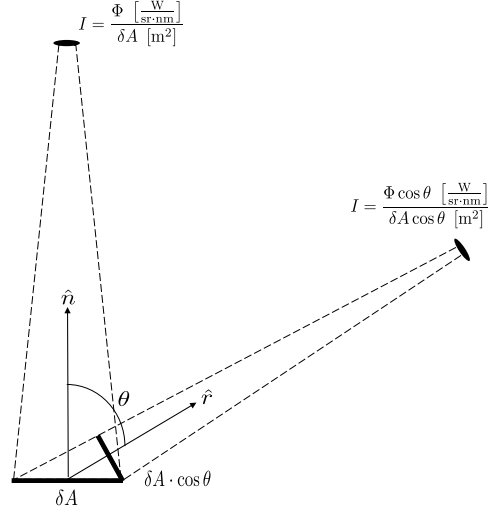


Figure 3.2: Lambertian surface δA . \hat{n} is the surface normal unit vector, while \hat{r} is the unit vector along the oblique observation angle.

3.5 Measurement equation

We can think of Planck's law (Eq. 3.1) as describing the measurement equation of an ideal radiometric sensor with responsivity 1 and an operating waveband of infinitesimal width. For such an instrument, an analytic solution for T could be obtained by solving the algebraic equation. In contrast, the measurement obtained by a real radiometric sensor is related to temperature via an integral equation that contains the thermal radiance of the surface $\varepsilon(\lambda) \cdot I_b(\lambda, T)$ integrated over the range of wavelengths $[\lambda_0, \lambda_1]$ defined by the optical filter and weighted by the spectral responsivity of the detector $S(\lambda)$ and the spectral transmittance of the filter $\mathcal{T}(\lambda)$,

$$S(T) = K \cdot \int_{\lambda_0}^{\lambda_1} \varepsilon(\lambda) \cdot \mathcal{T}(\lambda) \cdot S(\lambda) \cdot I_b(\lambda, T) d\lambda \quad (3.8)$$

To facilitate the temperature calculation in the case of a narrow band radiometer, the integral equation (Equation 3.8) can be approximated with negligible systematic error by the following algebraic expression,

$$S = \varepsilon \cdot \frac{k_1}{\exp\left(\frac{c_2}{k_2 \cdot T + k_3}\right) - 1} \quad (3.9)$$

This is the Planck version of the Sakuma-Hattori equation [85–89] that has been shown to provide the best fit in calibrating single waveband pyrometers [88]. The

model error introduced by the approximation amounts to a few mK at 3300 K [88] and decreases for lower temperatures. The Sakuma-Hattori equation (Eq. 3.9) retains the algebraic form of Planck's law (Eq. 3.1) and the accuracy of the integral equation (Eq. 3.8). Solving Eq. 3.9 for temperature one obtains,

$$T = \frac{c_2}{k_2 \cdot \log\left(\frac{\varepsilon \cdot k_1}{S} + 1\right)} - \frac{k_3}{k_2} = f_{\mathbf{k}}(S, \varepsilon) \quad (3.10)$$

Eq. 3.10 is parametrized by three calibration coefficients [85] that absorb any information about the spectral responsivity $S(\lambda)$ and solid angle of observation. Specifically, the coefficients k_1 , k_2 and k_3 are related to the detector spectral responsivity $S(\lambda)$ (mean wavelength λ_0 , variance σ^2 and total area under curve $\int_0^\infty S(\lambda)d\lambda$) and the geometry of the optical setup (K), with

$$k_1 = K \frac{c_1}{\lambda_0^5} \left(1 + 15 \frac{\sigma^2}{\lambda_0^2}\right) \int_0^\infty S(\lambda)d\lambda, \quad (3.11)$$

$$k_2 = \lambda_0 \cdot \left(1 - 6 \frac{\sigma^2}{\lambda_0^2}\right) \quad (3.12)$$

$$k_3 = \frac{c_2}{2} \frac{\sigma^2}{\lambda_0^2} \quad (3.13)$$

One approach is to calculate the coefficients from Eq. 3.11,3.12,3.13 which requires measuring the spectral responsivity $S(\lambda)$. Determining k_1 would require absolute spectral radiance measurements on the detector and determination of the geometry factor K . Evaluating k_2 and k_3 would require only knowledge of the shape of the responsivity curve that can be more easily extracted by relative radiance measurements. Note that $\lambda_0 = \frac{\int_0^\infty \lambda S(\lambda)d\lambda}{\int_0^\infty S(\lambda)d\lambda}$ and $\sigma^2 = \frac{\int_0^\infty (\lambda - \lambda_0)^2 S(\lambda)d\lambda}{\int_0^\infty S(\lambda)d\lambda}$. The approach followed in this work is estimation of the coefficients by calibrating Eq. 3.10 to a set of S, T data points — where T is provided from a reference source.

3.6 Operating principle of double modulation pyrometry

To illustrate the working principle of double modulation pyrometry [90], we first assume a radiometric detector observing an opaque lambertian surface of reflectance ρ in the focus of a solar simulator and follow the light path from source to detector: concentrated light (I_0) directly irradiates the surface, where it is partially $(1 - \rho)$ absorbed causing the surface to heat up to a temperature T , and partially (ρ) reflected. The radiosity $(\rho \cdot I_0 + \varepsilon \cdot I_b(T))$ exiting the surface within a narrow

cone subtended by the lens aperture, is collected, coupled to an optical fiber and detected. In this scenario, there are two points along the optical path where we lose the ability to separate our signal of interest ($\varepsilon \cdot I_b(T)$) from the unwanted contribution caused by I_0 and noise: (a) The first is the target surface after which I_0 is mixed with the thermal self-emission. (b) The second is the detector where the radiosity signal may pick up optical noise in the form of either background or stray radiation, or 1/f noise.

3.6.1 Double modulation

To separate $\rho \cdot I_0$ from $\varepsilon \cdot I_b(T)$, first the flux (I_0) approaching the surface is modulated at a frequency ω_1 . In doing so, a fraction M_1 of the power of I_0 shifts to ω_1 and is therefore immune to the mixing with the thermal radiation that occurs at the surface. Second, the radiosity signal is intercepted at the distal end of the optical fiber and amplitude-modulated at a frequency ω_2 . Hence, a fraction M_2 of the radiosity shifts to ω_2 and is therefore immune to the low frequency noise (1/f noise, background or stray radiation) that is predominantly added at the detector. The spectral separation is illustrated in the simplified Fourier-spectrum (Fig. 3.3) showing the frequency content of the detector output $D(t)$. Note, that we only consider the DC term and the fundamental frequency - all other terms have been omitted.

The modulation function $m_2(t)$ — applied on the collected beam at the exit of the optical fiber — is implemented by a small chopper, physically contained in the measurement setup next to the lock-in amplifiers and detector. In contrast, it is more challenging to implement the modulation $m_1(t)$ of the concentrated flux, since the design has to take into account the geometry of the experimental setup.

3.6.2 Phase sensitive detection

In the previous section, we saw that that $m_1(t)$ modulation spectrally separates the irradiance and radiosity signals prior to their mixing. The shifted parts of the two signals can now be tracked by the two phase-sensitive detectors LIA₁ and LIA₂. The outputs of the two lock-in amplifiers are the two observable quantities on which DMP builds to calculate the temperature. In this section, the time-domain representation of these signals is formulated.

Assuming a sinusoidal modulation and ignoring higher-order harmonics, the time-domain representation of the amplitude modulation function applied to the surface irradiance ($i = 1$) and surface radiosity ($i = 2$) is of the form:

$$m_i(t) = 1 - 0.5M_i(1 + \cos \omega_i t) \quad (3.14)$$

Hence, the time-domain representation of the detector output is

$$D(t) = (\rho(t)I_0(t)m_1(t) + \varepsilon(t)I_{\text{th}}(t)) \cdot m_2(t) \quad (3.15)$$

$D(t)$ is fed in parallel to the two lock-in amplifiers (LIA) that are phase-locked to ω_1 and ω_2 , thereby extracting respectively,

$$\begin{aligned} \text{LIA}_1(t) &\propto G_1 \cdot M_1 \cdot \rho(t) \cdot I_0(t) \\ \text{LIA}_2(t) &\propto G_2 \cdot M_2 (\varepsilon(t) \cdot I_b(t) + \rho(t) \cdot I_0(t)) \end{aligned} \quad (3.16)$$

where M_1, M_2 are the modulation amplitudes. G_1, G_2 are the gains of the two optoelectronic paths that encapsulate all characteristic factors related to the geometry of the setup, the collection optics, the detector and LIA gains. Note that M_1, M_2, G_1, G_2 remain constant for a given instrument configuration.

The lock-in outputs (Eq. 3.16) are intermediate results. Assuming linearity of the detector and electronics, LIA_1 and LIA_2 are linear functions of $\rho \cdot I_0$ and $\rho \cdot I_0 + \varepsilon \cdot I_b(T)$ respectively. From these we wish to obtain the thermal signal because it contains the temperature information. We observe that Eq. 3.16 would yield a determined system of two equations that could then be solved for $I_b(T)$ provided that the modulation amplitudes (M_1, M_2), path characteristics (G_1, G_2) and ε were characterized. A more direct approach is via a simple experimental procedure, the gain calibration.

3.6.3 Gain calibration

It is evident in Eq. 3.16 that the thermal signal could be obtained as the difference of the two LIAs, if both were scaled properly. Due to the different modulation functions and lock-in gains, this is not the case. Nevertheless, there is a linear relationship. Estimating it is the goal of gain calibration step.

By comparing into the two LIA outputs in Eq. 3.16, we observe that if we were to constrain $I_b(T) \rightarrow 0$ and then obtain measurements of LIA_1 and LIA_2 at different predetermined levels of intensity I_0 , then the linear relationship between LIA_1 and LIA_2 can be estimated by least-squares fitting. The best-fit line obtained based on the measurements represents a characteristic of the instrument, determined by its slope (g_1) and intercept (g_0), referred to as the gain calibration coefficients. In summary, g_0, g_1 are obtained as the least-squares fitted estimates that scale LIA_1 so that $\text{LIA}_2 - (g_1 \cdot \text{LIA}_1 + g_0) \rightarrow 0$ for a cold target.

The procedure is realized by using a water-cooled white lambertian target (Al_2O_3 coated Cu). Inserting different neutral density filters in the optical path allows to perform the calibration over a large dynamical range.

Once LIA_1 and LIA_2 have been scaled properly, they act as a balanced-pair where a certain observable $\rho \cdot I_0$ flux induces identical voltage responses. Upon

subtracting the two outputs, the common-mode signal is rejected and their difference yields a voltage signal S that is a linear function of the thermal emission. Now, the thermal emission of a hot sample can be measured,

$$S(t) = \text{LIA}_2 - g \cdot \text{LIA}_1 \quad (3.17)$$

Note, that changes to the pyrometer that affect both signals in identical ways, such as changing the band pass filter, do not affect the gain calibration.

3.6.4 *In-situ* indirect measurement of spectral directional emissivity

According to Eq. 3.16 the output of LIA_1 contains the product of reflectance and irradiance, i.e. $\text{LIA}_1(t) \propto \rho(t) \cdot I_0(t)$. Assuming that at time t_0 the output of $\text{LIA}_1(t_0)$ is recorded while observing a water-cooled white lambertian target of known reflectance $\rho(t_0)$. Then $\forall t$, the output $\text{LIA}_1(t)$ is recorded while observing a surface of unknown reflectance $\rho(t)$. We take the ratio of the LIA_1 output at these two instants and solve for the unknown $\rho(t)$,

$$\frac{\text{LIA}_1(t)}{\text{LIA}_1(t_0)} = \frac{\rho(t) \cdot I_0(t)}{\rho(t_0) \cdot I_0(t_0)} \Rightarrow \rho(t) = \rho(t_0) \cdot \left(\frac{I_0(t)}{I_0(t_0)} \right)^{-1} \frac{\text{LIA}_1(t)}{\text{LIA}_1(t_0)} \quad (3.18)$$

By observing Eq. 3.18 we note that the presence of the ratio $I_0(t)/I_0(t_0)$ entails that it is sufficient to measure the value of I_0 at time t relative to its value at t_0 . In addition, ρ can be assumed an approximation of the *hemispherical, directional, spectral* reflectance (ρ_Ω, θ) ([91]). This is because in a CSP facility, samples are irradiated approximately hemispherically, while the collection optics of the narrow-band sensor subtend a relatively small solid angle. Hence, for an opaque sample $\varepsilon = 1 - \rho$ is a good approximation of the directional spectral emittance.

In a solar furnace facility, a relative measure of $I_0(t)$ can be obtained experimentally from the product of normalized DNI and effective transmittance of the shutters τ_{shutter} ,

$$I_0(t) \propto \text{DNI}(t) \cdot \tau_{\text{shutter}}(t) \quad (3.19)$$

where DNI is available from a pyheliometer, while $\tau_{\text{shutter}} \in [0, 1]$ is obtained from the shutter control system. In a solar simulator, I_0 may be obtained by measuring with a photo-detector the ambient flux.

3.6.5 Temperature calibration

In the previous section, we derived the voltage signal (S) that is a linear function of the thermal emission only. In this section, we briefly discuss the mapping from the voltage scale to the temperature scale. As discussed in Sec. 3.5, a measurement equation (Eq. 3.10), based on the Sakuma-Hattori algebraic equation [85, 88, 89], is used to map the measured voltage signals S (Eq. 3.17) and ρ (Eq. 3.18) to the temperature scale, allowing estimation of the true temperature. ($f_{\mathbf{k}} : [S, \rho] \xrightarrow{\mathbf{k}} T$).

We calibrate against a gray body surface (such as Platinum), where T_{ref} is obtained by a reference pyrometer, while $\varepsilon(\lambda, \theta)$ is either obtained *in-situ* via Eq. 3.18 or assumed known. The optimal coefficients can be obtained by fitting the non-linear equation $f_{\mathbf{k}}$ to the S and T_{ref} data obtained from the DMP and reference pyrometer respectively:

$$\mathbf{k}_{\text{opt}} = \underset{\mathbf{k}}{\text{argmin}} (f_{\mathbf{k}}(S, 1 - \rho) - T_{\text{ref}})^2 \quad (3.20)$$

where $f_{\mathbf{k}}$ is the non-linear function from Eq. 3.10. The fitting is implemented by using a Matlab implementation of the trust-region reflective algorithm [92, 93]. Note that changes applied to the modulation function $m_1(t)$ are absorbed by the gain calibration coefficients and do not affect the temperature calibration coefficients. In contrast, modifying m_2 will affect all calibration coefficients.

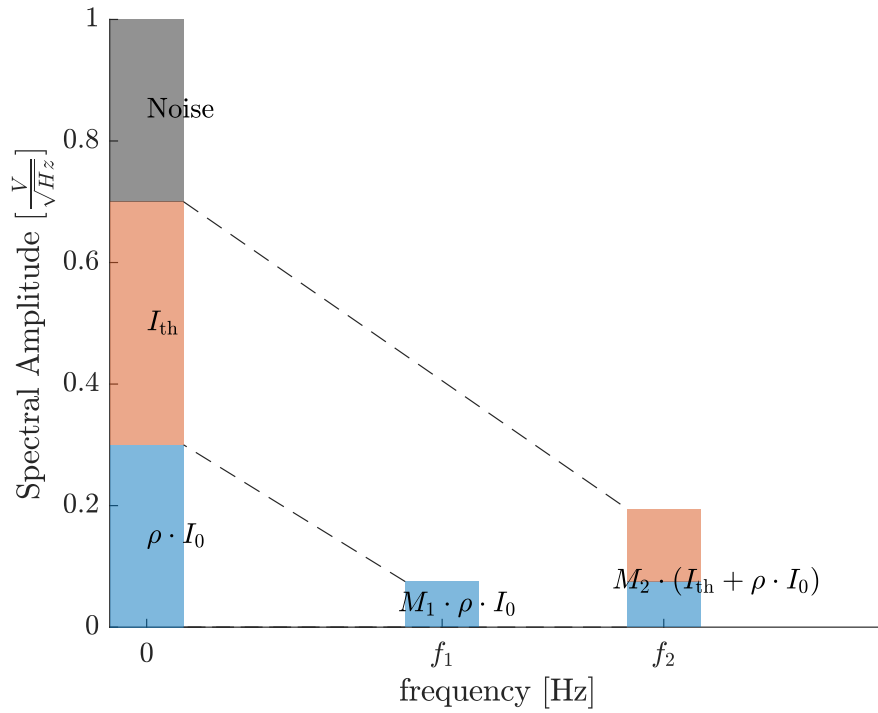


Figure 3.3: Simplified schematic of the frequency spectrum of the detected signal $D(t)$. At 0 Hz, the two main signal components are mixed. At f_1 and f_2 , the independently modulated components appear corresponding to the radiosity and the reflected irradiance. The components are stacked in the same order as they would appear if we were to traverse the optical path from source to detector: First, a fraction M_1 of I_0 is shifted to f_1 . Then, I_0 gets reflected and mixed with the thermal self-emission. A fraction M_2 of that mixture is shifted to f_2 . Finally at the photodetector, background radiation and electronic noise are added to the mixture.

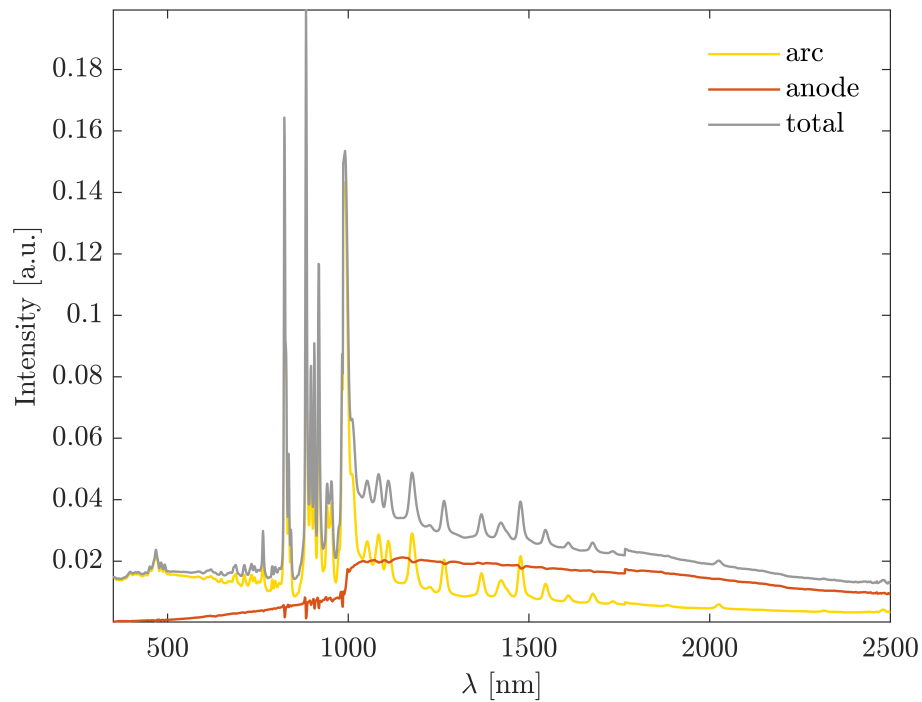


Figure 3.4: Breakdown of the spectrum of a Xenon-arc lamp to its main constituents, the arc and electrode contributions. Distribution of light-intensity over wavelength for various components of a short discharge Xenon-arc lamp. Data taken from [48]

Chapter 4

Double Modulation Pyrometry: A radiometric method to measure surface temperatures of directly irradiated samples¹

The design, implementation, calibration and assessment of double modulation pyrometry to measure surface temperatures of radiatively heated samples in our 1 kW imaging furnace is presented. The method requires that the intensity of the external radiation can be modulated. This was achieved by a rotating blade mounted parallel to the optical axis of the imaging furnace. Double modulation pyrometry independently measures the external radiation reflected by the sample as well as the sum of thermal and reflected radiation and extracts the thermal emission as the difference of these signals. Thus a two-step calibration is required: First, the relative gains of the measured signals are equalized and then a temperature calibration is performed. For the latter we transfer the calibration from a calibrated solar blind pyrometer that operates at a different wavelength. We demonstrate that the worst case systematic error associated with this procedure is about 300 K but becomes negligible if a reasonable estimate of the sample's emissivity is used. An analysis of the influence of the uncertainties in the calibration coefficients reveals that one (out of five) coefficients contributes almost 50% to the final temperature error. On a low emission sample like platinum the lower detection limit is around 1700 K and the accuracy typically about 20 K. Note, that these moderate specifications are specific for the use of double modulation pyrometry at the imaging furnace. It is mainly caused by the difficulty to achieve and maintain good overlap of the hot zone (diameter of about 3 mm FWHH) and the measurement spot which

¹Material in this chapter has been published in Potamias, D., Alxneit, I. and Wokaun, A. (2017). Double modulation pyrometry: A radiometric method to measure surface temperatures of directly irradiated samples. *Review of Scientific Instruments*, 88(9), 95112. <https://doi.org/10.1063/1.4987129>

both are of similar size.

4.1 Introduction

Temperature measurement in the presence of intense background radiation is a recurrent problem in many applications. In the field of solar energy research where means to convert concentrated solar radiation into more useful forms of energy are developed solar blind pyrometry [42, 43] is often used. Solar blind pyrometers operate in narrow spectral bands where the solar radiation is completely absorbed by the atmosphere. Thus, they are immune to reflected solar radiation and selectively detect the thermal emission of the sample.

In the last decade, significant activity has developed using solar simulators [37]. These devices provide concentrated radiation with a spectrum similar to the terrestrial solar spectrum. They provide weather-independent, reproducible experimental conditions and serve as test bed for prototype testing of novel solar technologies. Solar simulators are usually built from several modules. Each module consists of a point-like, bright, broadband and non-collimated radiation source — typically a Xe short arc lamp — positioned at the focal point of an ellipsoidal specular reflector. Radiation converges at the conjugate focus that is made to coincide for all modules. Flux densities equivalent to concentration ratios of a few thousand suns are attained, where $1 \text{ sun} = 1 \text{ kWm}^{-2}$. The equivalent of solar blind pyrometry is not feasible in solar simulators since the Xenon-arc spectrum consists of discrete emission lines superimposed on a continuous black body spectrum. In contrast, the terrestrial solar spectrum contains narrow spectral bands where solar radiation has been attenuated due to atmospheric absorption. Solar blind pyrometers operate in these wavelength bands where no solar radiation is present.

Several non-contact methods to measure surface temperatures under intense external radiation have been developed, such as Flash Assisted Multi-wavelength Pyrometry (FAMP) [49, 51, 52] or pyro-reflectometry [56, 57, 74]. Both methods are in addition capable to determine *in-situ* the emissivity of the sample. However, both methods also require a second source of external radiation with an intensity comparable to the concentrated (solar) radiation as well as a cold reflectivity reference. An alternative method, double modulation pyrometry (DMP), that requires neither an additional light source nor a cold reflectivity reference can be used if the intensity of the external radiation can be modulated at high frequency compared to the thermal time constant of the sample observed.[90] The method uses phase sensitive detection at two different frequencies to discriminate between thermal emission and reflected external radiation similar to a setup described earlier [70].

Here, we will describe the implementation of DMP in our 1 kW imaging furnace [94, 95] where modulation of the external radiation cannot easily be achieved. After

recapitulating the theory of DMP the design of a mechanical modulator and its theoretical performance will be discussed. Experimental results obtained will be discussed and the performance of DMP in the imaging furnace tested. Finally an error analysis will be presented to locate significant sources of error in the measurements.

4.2 Theory of Double Modulation Pyrometry

Radiometric temperature measurement methods sample radiation L originating from the observed surface and correlate it to its true surface temperature T via the Planck formula

$$L(\varepsilon, \lambda, T) = \varepsilon \cdot \frac{c_1}{\lambda^5} \cdot \frac{1}{\exp\left(\frac{c_2}{\lambda T}\right) - 1} = \varepsilon \cdot L_{\text{BB}}(\lambda, T) \quad (4.1)$$

with c_1 and c_2 the first and second radiation constants. Knowledge of the emissivity ε is required to derive temperature as a function of the measured radiance by solving Eq. 4.1 for the temperature. All radiation observed, including reflected external radiation, is interpreted as thermal emission of the sample. Spectral filtering cannot be applied to discriminate between thermal and reflected radiation when working with a continuous radiation source that emits in the same wavelength region as the thermal emission. Thus, an active method based on frequency filtering instead has been developed that operates according to the schematic in Fig. 4.1. A periodic perturbation $m_1(t)$ with frequency ω_1 is enforced on the intensity of background radiation prior to it reaching the sample. Radiation originating from the sample within a solid angle subtended by the aperture of the collection optics contains the sum of thermally emitted and modulated reflected radiation. Prior to reaching the detector it is modulated by $m_2(t)$ at a frequency ω_2 . This allows to simultaneously detect the reflected radiation and the sum of thermal and reflected radiation by feeding the signal of the detector to two lock-in amplifiers (LIA) that use ω_1 and ω_2 as reference signals (for details see [90]). If we analyze the paths that the radiation responsible for the signals S_1 and S_2 in phase with ω_1 and ω_2 contain, we find (for simplicity the wavelength dependence has been dropped)

$$S_1 = I_0 \rho_{\cap, \theta} \quad (4.2)$$

$$\begin{aligned} S_2 &= I_0 \rho_{\cap, \theta} + \varepsilon L(\varepsilon, T) \\ &= I_0 \rho_{\cap, \theta} + (1 - \rho_{\cap}) L_{\text{BB}}(T) \\ &= I_0 \rho_{\cap, \theta} + I_{\text{th}} \end{aligned} \quad (4.3)$$

Here we assume an opaque sample and use Kirchhoff's law that connects ρ , ε , and α . $\rho_{\cap, \theta}$ is the reflectivity observed under a solid angle of θ when the sample is

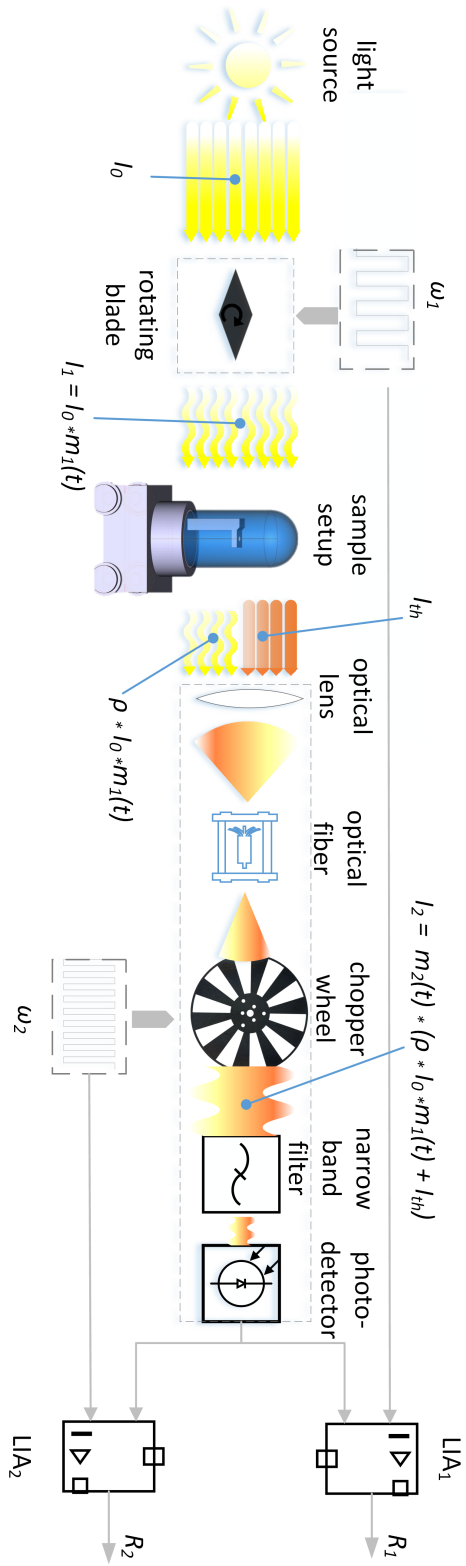


Figure 4.1: Setup: Light emitted by the lamp, a fraction of it modulated at ω_1 by a rotating blade, is focused onto the sample. Radiation from the sample is coupled by a lens into a fiber. After the fiber, radiation is chopped at ω_2 and projected by an achromat onto a detector after passing a narrow band pass filter. Signal components in phase with ω_1 and ω_2 are analyzed by two lock-in amplifiers (LIA).

illuminated at a solid angle of π as is the case in our setup. Assuming a Lambertian sample $\rho_{\Omega,\theta} = \rho_{\Omega}$, the thermal signal can be extracted as the difference of Eq. 4.3 and Eq. 4.2.

4.3 Calibration Procedure

Two separate calibration steps are required for DMP. First, the conversion gain ($[\text{Wsr}^{-1}\text{nm}^{-1}] \rightarrow [\text{V}]$) for the two LIA has to be made equal (gain calibration). This is achieved by scaling R_1 as $R'_1 = g_0 + g_1 \cdot R_1$ with g_0 and g_1 determined in the calibration procedure. The difference between R_2 and R'_1 is only a linear function of the thermal flux I_{th} .

$$R_{\text{th}} = R_2 - \underbrace{(g_0 + g_1 R_1)}_{R'_1} = h(R_1, R_2, \mathbf{g}) \quad (4.4)$$

Then, a temperature calibration has to be performed to connect R_{th} to a temperature scale by determining the calibration constants k_1 , k_2 , and k_3 of Eq. 4.5.

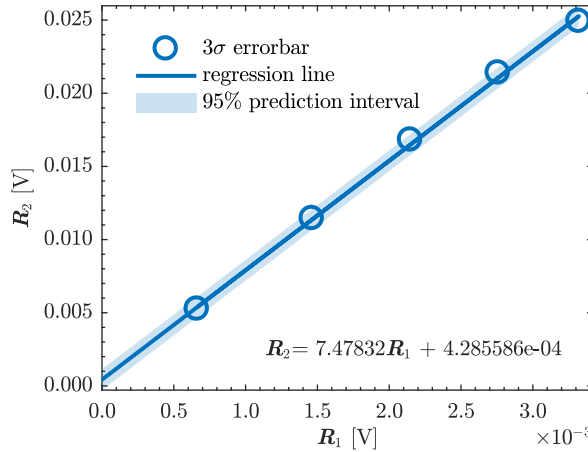


Figure 4.2: R_1 and R_2 off a cold target measured with neutral density filters ($\tau = 19.86\%$, 43.35% , 64.47% , 84.24% and 100%) inserted in the optical path. Result of the least-squares fit (solid line) and 95% confidence interval (colored band) are also indicated.

4.3.1 Gain Calibration

If a cold target is observed S_1 and S_2 are equal as $I_{\text{th}} = 0$ (Eq. 4.3). This situation is realized by observing a water-cooled target (Al_2O_3 coated Cu) in the imaging

furnace but with the external radiation turned on. Inserting different neutral density filters in front of the band pass filter allows to perform the calibration over a large dynamical range and to recognize possible saturation of the detector.

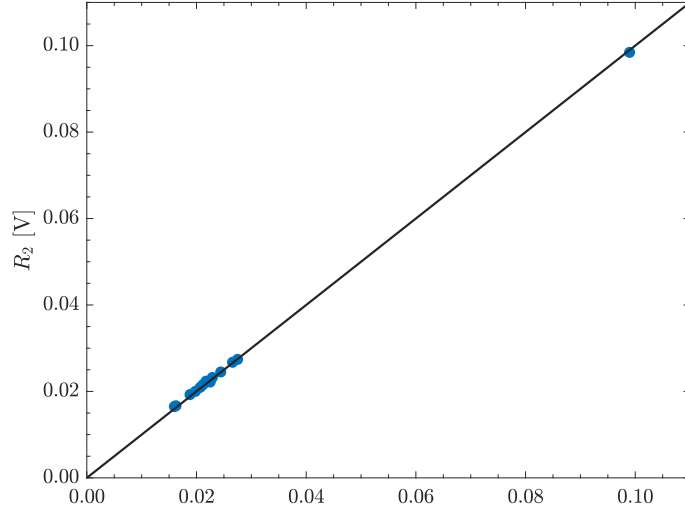


Figure 4.3: R_1' and R_2 from gain calibrations sessions spanning a one-month period. Outlier corresponds to a new operation wavelength of $1.2 \mu\text{m}$.

In Fig. 4.2 we report typical gain calibration data from which g_0 and g_1 are estimated by linear regression. The slope of the curve describes the relative gains of the two LIA. Note, that changes to the pyrometer that affect S_1 and S_2 in identical ways, such as e.g. changing the band pass filter, do not require recalibration as they affect both signals identically. This is illustrated in Fig. 4.3 where data collected during gain calibrations spanning approximately a one-month period and at two different operation wavelengths ($1.2 \mu\text{m}$ for the bulk of the data and $1.0 \mu\text{m}$ for the outlier) all lie on the same line.

4.3.2 Temperature Calibration

To establish a temperature calibration the thermal signal R_{th} is recorded at discrete temperatures on a sample with known ε . Typically, a black-body source ($\varepsilon=1.0$) that can be operated in the temperature range foreseen for the pyrometer is used. Here, we chose an alternative route: Transfer of the calibration from a calibrated solar blind pyrometer. The setup is reported in Fig. 4.4. A platinum strip is mounted at the focus of the imaging furnace, its temperature varied by forced convective cooling using air. The reference pyrometer operating at 1385 nm , [42] observes the back of the sample and is not influenced by the external radiation. The DMP observes the front surface at $1.2 \mu\text{m}$.

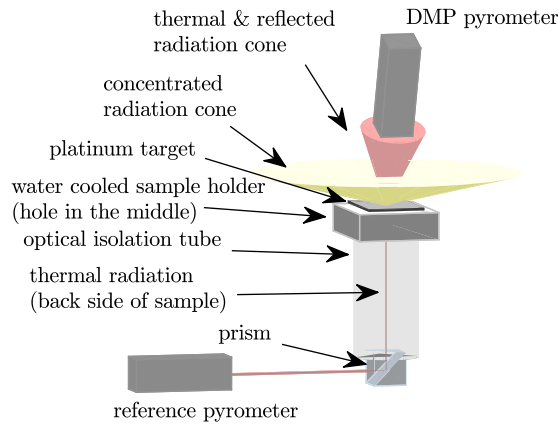


Figure 4.4: Temperature calibration setup.

Note, that due to the emissivity dependence $\epsilon_{\text{eff}}(\lambda, T, \vartheta)$, this procedure is strictly valid under the assumption that the two sides share the same optical properties and surface temperature, and that the two pyrometers operate at the same wavelength and observation angle. The sample can be assumed isothermal due to the high thermal diffusivity and small thickness (0.127 mm) of the sample. Due to the weak wavelength dependence of its emissivity [96, 97] identical brightness temperatures for the front and back are assumed too. Note, that the wavelength difference introduces a systematic temperature error in the calculation of the brightness temperature that is discussed later if an incorrect value of ϵ is used. A typical temperature calibration is reported in Fig. 4.5.

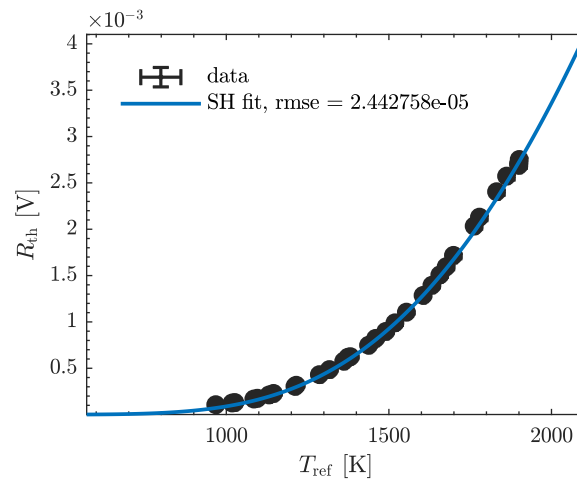


Figure 4.5: Temperature calibration curve for DMP operated at $1.2 \mu\text{m}$ and $\epsilon_{\text{eff}} = 1.0$. T_{ref} is from solar blind pyrometer. Calibration curve is obtained from non-linear least-squares fit of Eq. 4.6

To facilitate the calculation of the calibration function the algebraic Sakuma-Hattori approximation [85, 87–89]

$$R_{\text{th}} = \frac{k_1}{\exp\left(\frac{c_2}{k_2 \cdot T + k_3}\right) - 1} \quad (4.5)$$

is used. This approximation has been shown to provide the best fit in calibrating single waveband pyrometers [88]. The model error introduced amounts to a few mK at 3300 K [88] and decreases for lower temperatures. Hence, the model error introduced by the use of Eq. 4.5 is negligible compared to the order of magnitude larger errors that are introduced during the temperature calibration procedure and during measurement as a result of the emissivity uncertainty. k_1 , k_2 and k_3 are calibration constants that are explicit functions of known parameters of the setup such as e.g. the spectral response of the detector or the transmission curve of the band pass filter. To avoid absolute radiometric measurements the constants were determined by a least-squares fit of Eq. 4.6, i.e. Eq. 4.5 solved for T .

$$T = \frac{c_2}{k_2 \cdot \log\left(\frac{k_1}{R_{\text{th}}} + 1\right)} - \frac{k_3}{k_2} = f(R_{\text{th}}, \mathbf{k}) \quad (4.6)$$

Eq. 4.6 is a non-linear function of the form $T = f(R_{\text{th}}, \mathbf{k})$, that relates the independent variable R_{th} , obtained from Eq. 4.4, to the response variable T_{dmp} . $\mathbf{k} = [k_1, k_2, k_3]$ denotes the coefficients to be estimated. For the calibration the data set with $n \gg 3$ data pairs $(R_{\text{th}}, T_{\text{ref}})$ (see Fig. 4.5) is used to formulate the nonlinear regression problem,

$$\hat{\mathbf{k}} = \underset{\mathbf{k}}{\operatorname{argmin}} (T_{\text{ref}} - f(R_{\text{th}}, \mathbf{k})) \quad (4.7)$$

with T_{ref} the response variable, R_{th} the predictor variable, and $\hat{\mathbf{k}}$ the optimal calibration coefficients obtained from the Levenberg-Marquardt nonlinear least-squares algorithm [98].

4.4 Implementation of double modulation pyrometry at the 1 kW imaging furnace

Modulation of the background radiation can be achieved by modulating either the electrical power fed to the arc lamp or by mechanically chopping its radiation before it reaches the target. In the first case, only the intensity of the arc is modulated as the thermal time constant of the anode is much too long and its emission thus essentially constant. In the setup used to demonstrate DMP [90],

emission from the electrodes did not reach the conjugate focus because the arc lamp was mounted perpendicular to the optical axis. Only the arc's radiation reached the sample. In the imaging furnace, however, the lamp axis coincides with the optical axis and the emission from the anode significantly contributes to the radiative flux at the conjugate focus.

The relative contribution of the electrode's thermal emission at $\lambda = 1.2 \mu\text{m}$ was determined by recording the reflected radiation as the lamp was turned off. The dynamic response is characterized by two time scales with estimated time constants of $\tau_1 \approx 60 \mu\text{s}$ and $\tau_2 \approx 10 \text{ s}$. The latter is attributed to the electrode's thermal emission that contributes about 40% to the total radiative flux (see Fig. 4.6). Preliminary tests revealed that the electrode takes a long time to reach thermal equilibrium and thus its contribution to the total radiation slowly increases during an extended experiment. Additionally, this contribution also changes with the lamp's age.

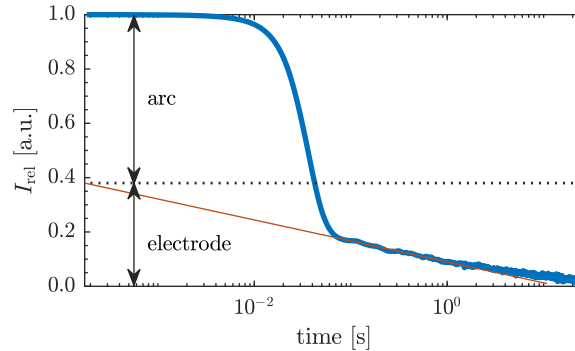


Figure 4.6: Shut down behavior of arc lamp. The relative contribution of the anode's thermal emission is obtained by extrapolation (red line).

4.4.1 Mechanical Modulation

In the imaging furnace a chopper wheel cannot be placed in front of the hemispherically irradiated sample and at the same time allowing its unobstructed observation. However, due to the axial symmetry of the reflector module, each sector spanning an azimuthal angle $\Delta\theta$ contributes with a fraction of $\Delta\theta/2\pi$ of both, arc and anode, to the total flux at the conjugate focus. Thus, intercepting an angular sector is equivalent to intercepting the full beam (as with a conventional chopper wheel). Thus, a rotating blade (see Fig. 4.7) mounted parallel to the optical axis modulates the *total* output of the lamp i.e. radiation from the arc *and* the anode.

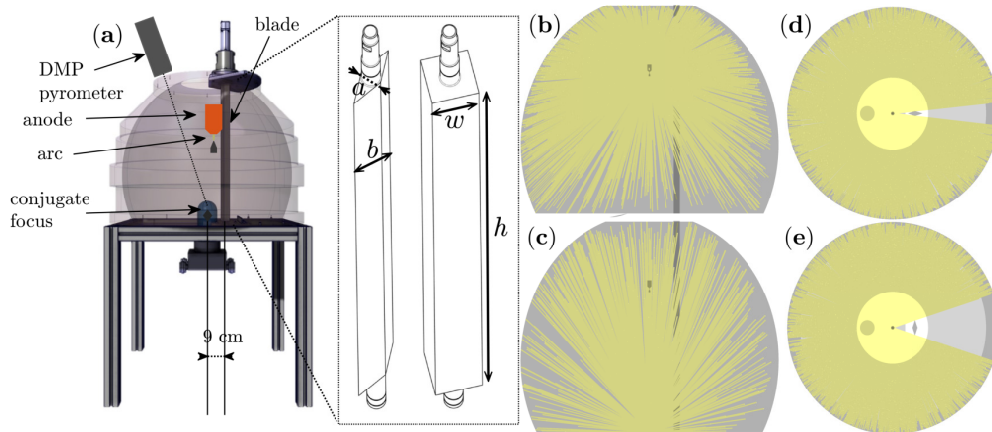


Figure 4.7: (a) Imaging furnace with the xenon-arc lamp, pyrometer, conjugate focus and rotating blade. Implemented blades: square ($a/b = 1$) and rhomboidal ($a/b = 1/3$). $w_{\blacksquare} = 4.25$ cm, $w_{\blacklozenge} = 3.16$ cm. (b) Rays emanating from the xenon-arc lamp intersect the ellipsoidal reflector and (c) are reflected to converge at the conjugate focus. (d-e) Top-view showing the rhomboidal blade blocking minimum (d) and maximum (e) sector of rays.

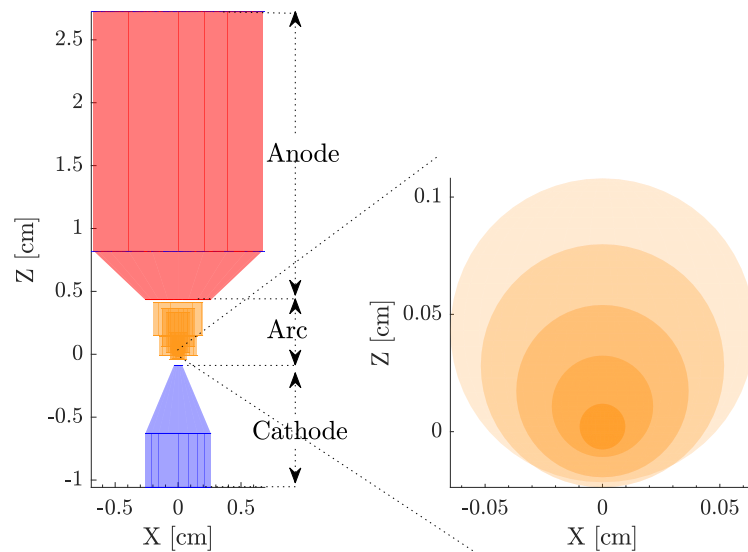


Figure 4.8: Lamp model. Non-transparent anode that emits diffusely from its surface. Rays intercepted by the anode are either reflected (micro faceted) or absorbed and then reemitted from a random position on the electrode. The arc consists of several transparent cylinders and spheres each emitting uniformly from their volumes. Cold, non-emitting cathode that absorbs or reflects intercepted rays.

Several blade designs were evaluated before selecting one with a rhomboidal cross section, length h , and width w of the faces (see Fig. 4.7). The resulting modulation function $m(\theta)$ was optimized as function of d (distance to the optical axis) and a/b (aspect ratio of the blade's cross section). Monte-Carlo geometrical ray tracing [99] was used to calculate $m(\theta)$ and the thermal load on the blade. The lamp's arc and anode was modeled by a combination of spherical, cylindrical, and conical sources (see Fig. 4.8). Measured spectra for arc and anode were used [48]. The reflector was modeled as micro-faceted surface (Gaussian distribution of local surface normals with $\sigma = 0.8$) with spectral reflectivity of Aluminum [100, 101]. The model reproduces the measured [95] flux distribution at the conjugate focus. The blade's surface was modeled as a micro-faceted surface ($\sigma = 0.123$) with the measured spectral reflectivity of oxidized Aluminum (see Fig. 4.9).

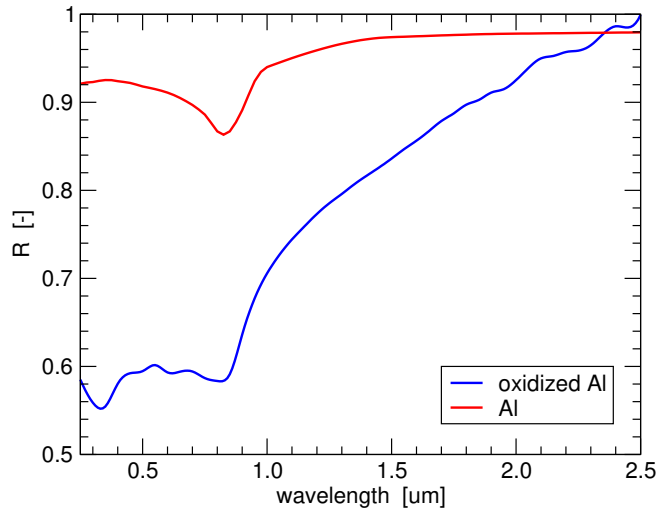


Figure 4.9: Measured spectral reflectivities of pure and oxidized aluminum.

The thermal load on the blades (See Fig. 4.10) was estimated to be on the order of 30 W with a hot-spot of 1.6 kW/m^2 at the height of the light source, resulting in an estimated peak temperature of $62 \text{ }^\circ\text{C}$. The temperature is low enough to use aluminum as construction material especially in view of the forced convective cooling caused by the rotation of the blade. The lowest eigenfrequencies of the two blades of Fig. 4.7 were calculated in ANSYS [102] as 97 Hz (rhombus) and 277 Hz (square).

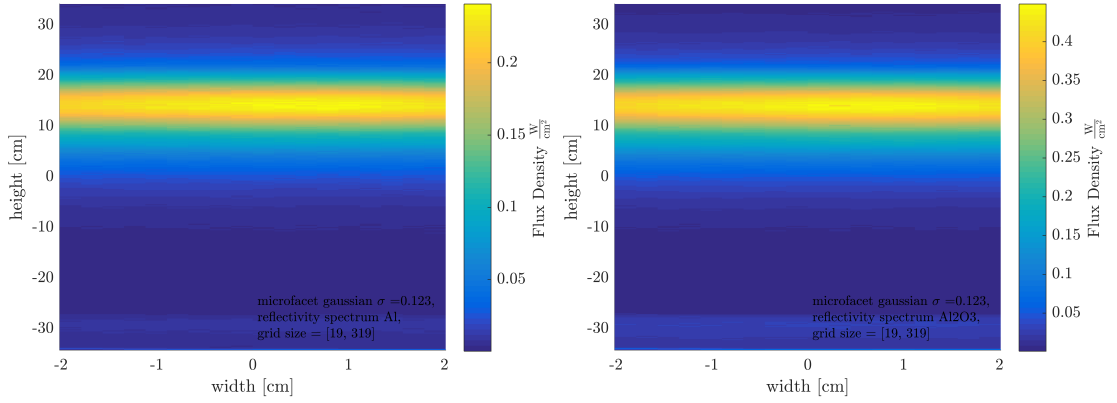


Figure 4.10: Calculated (absorbed) flux distribution on blade with a square cross section and one side facing the source at $d = 9$ cm, 800 W. (left) aluminum blade, (right) oxidized aluminum blade. Reflectivity spectra of Fig. S3 were used.

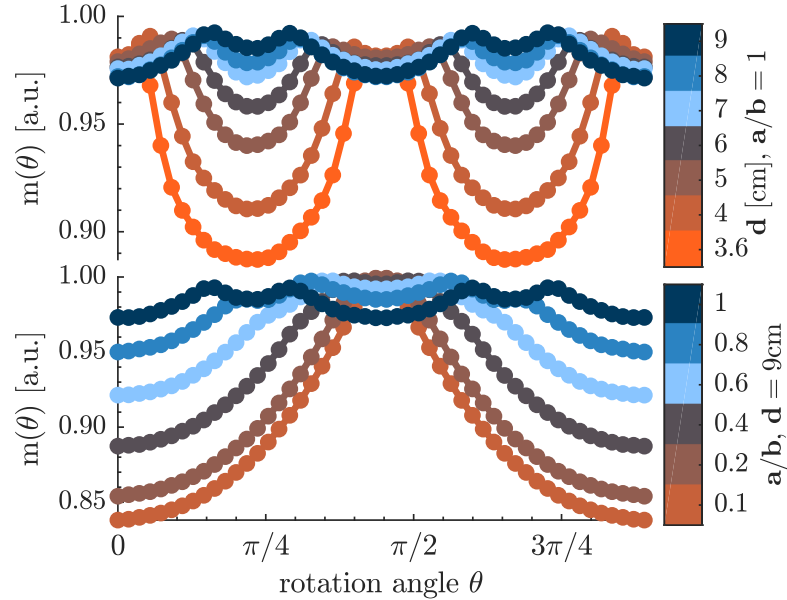


Figure 4.11: $m(\theta)$ as function of aspect ratio a/b , $d = 9$ cm (bottom) and distance from the optical axis d , $a/b = 1$ (top).

$m(\theta)$, i.e. the relative flux density at conjugate focus, as function of the aspect ratio (at $d = 9$ cm) and distance from the optical axis (at $a/b = 1$) is reported in Fig. 4.11. Because of the two-fold symmetry of the rhombus the calculation were limited to $\theta \in [0, \pi]$. As the aspect ratio tends to unity, the modulation depth decreases while secondary minima develop at $\theta = \pi/4$ or $3\pi/4$. For the square cross section, $m(\theta)$ was also calculated as a function of d which affects the relative

depth of the minima at $\theta = \pi/2$ versus $\theta = \pi/4$ or $3\pi/4$. At $d \approx 7$ cm all minima are equal because at this position the long cross section blocks the same angle $\Delta\theta$ at $\theta = \pi/2$ as the side does at $\theta = \pi/4$ or $3\pi/4$ because the side sits closer to the optical axis (Details see Fig. 4.12).

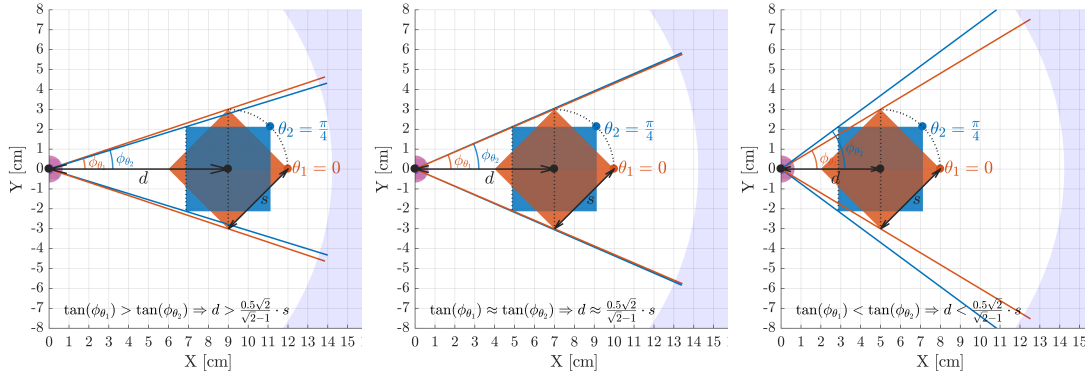


Figure 4.12: At $d = 7$ cm (middle) the same angle ϕ is covered at $\theta = 0$ and $\theta = \pi/4$ and radiation is modulated at $4f$. At $d < 7$ cm (bottom) $\phi_2 > \phi_1$ while at $d > 7$ cm (top) $\phi_2 < \phi_1$. In the latter two cases, both, $4f$ and $2f$, are present.

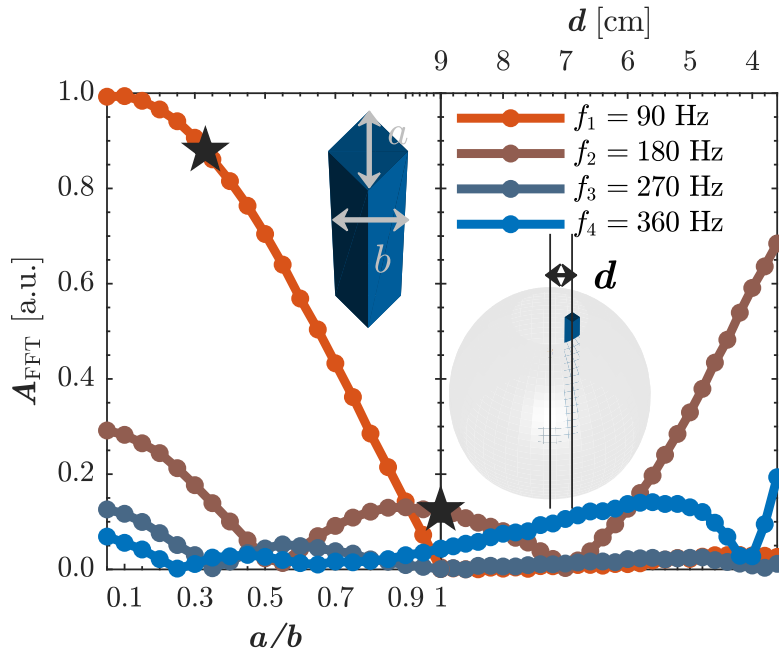


Figure 4.13: The first four harmonics of the blade's modulation function as function of a/b (left) and d (right). Blades built are marked with \star .

Assuming a rotation frequency of $f_0 = 45$ Hz the fundamental modulation

frequency will be at $f_1 = 2f_0 = 90$ Hz. The Fourier transform of the modulation functions reported in Fig. 4.11 was used to identify the dominant harmonics. The results are shown in Fig. 4.13 where the contribution of the first few harmonics are reported as a function of a/b and d . The designs built, marked with \star in the figure, correspond to $d = 9$ cm ($d = 7$ cm could not be realized due to spatial constraints) at $a/b = 1/3$ (f_1 dominates) and $a/b = 1$ (f_2 dominates). Note, that moving the rotation axis of the blade to about 7 cm would suggest operation at f_4 .

4.5 Evaluation of the performance of double modulation pyrometry at the 1 kW imaging furnace

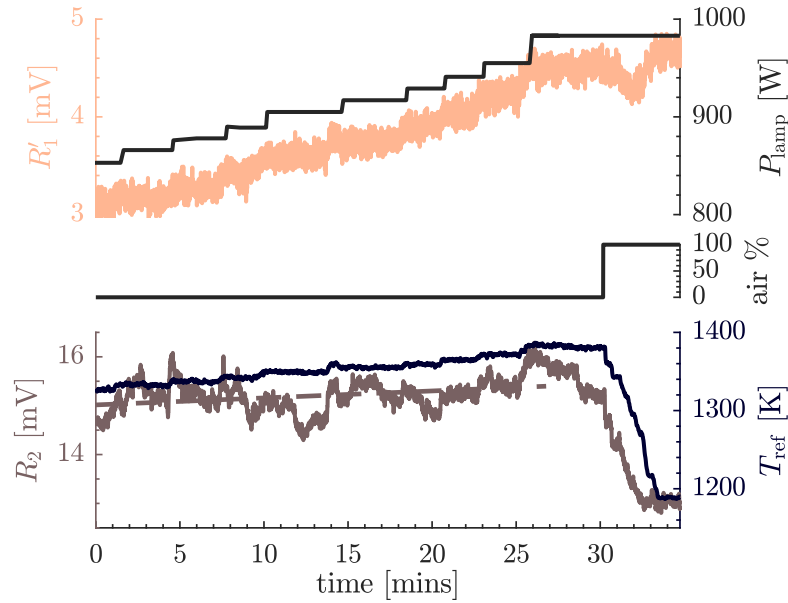


Figure 4.14: Response of R'_1 (top) and R_2 (bottom) to changes in I_0 and T .

To verify that R'_1 records the external radiation I_0 while R_2 records both, I_0 and I_{th} , the same setup as during calibration was used. The platinum strip was exposed to a constant radiative flux until a brightness temperature ($\epsilon = 1.0$) of $T_{ref} = 1300$ K was reached ($t = 0$) (see Fig. 4.14). Then, I_0 is gradually increased by increasing the power P supplied to the lamp from 860 W to 980 W. During this interval, R'_1 follows P , i.e. I_0 . T_{ref} increases slightly during the same period as the sample's temperature increases. The increases in both external and thermal radiation contribute to the observed increase of R_2 . At about $t = 1750$ s, forced air cooling starts. Both R_2 and T_{ref} immediately decrease as the sample

cools rapidly. R'_1 , however, remains undisturbed as it is sensitive to the external radiation only. Note that the initial small and rapid dip in R'_1 is due to the change ρ_{Pt} during cooling since R'_1 represents the external radiation reflected by the target, i.e. $R'_1 \propto I_0 \cdot \rho_{Pt}$. This is consistent with the decrease and subsequent increase observed in Fig. 4.15 during the heating of the sample.

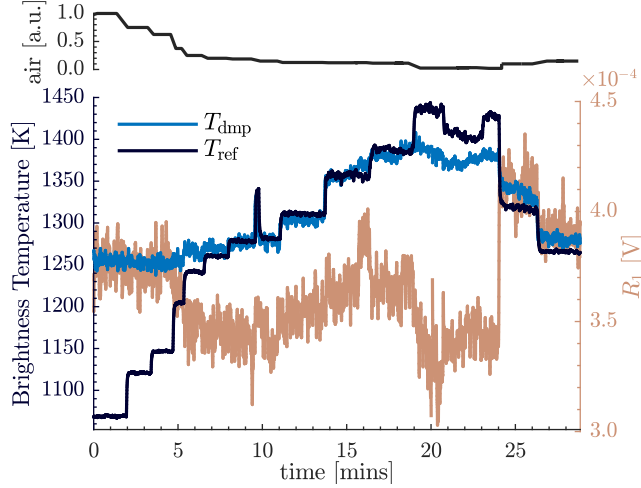


Figure 4.15: Comparison of true temperature recorded with solar blind pyrometer (T_{ref}) and DMP (T_{DMP}) while varying the relative strength of the cooling air flow (air). R'_1 is used to track changes in the sample's reflectivity.

The same setup is used to demonstrate the main features and limitations of DMP implemented at the imaging furnace. In Fig. 4.15, brightness temperatures ($\epsilon_{\text{eff}} = 1$) recorded by the solar-blind pyrometer and DMP are compared while the platinum sample is heated and then cooled under constant radiative flux by changing the convective cooling rate in steps. Under these conditions, the detection limit of DMP is ≈ 1700 K. Note, that this is not an inherent weakness of the method, but a consequence of the specific implementation at the imaging furnace. The blade that results in a low modulation depth and the low emissivity of platinum both lead to a high detection limit.

While the sample is heated, the two brightness temperatures coincide within ≈ 20 K. At $t = 19$ min they suddenly diverge. At the same time a pronounced drop of R'_1 is observed. Starting at $t = 24$ min the convective cooling is increased in steps and both temperatures drop in parallel while R'_1 suddenly increases. During cooling the difference between T_{ref} and T_{dmp} has increased to 30 K. After the experiment, we noticed that the sample had melted forming a liquid film that later solidified to form a mirror-like surface (see Fig. 4.16).

With this information the data of Fig. 4.15 can be understood. While the sample is heated both pyrometers report the same brightness temperature because

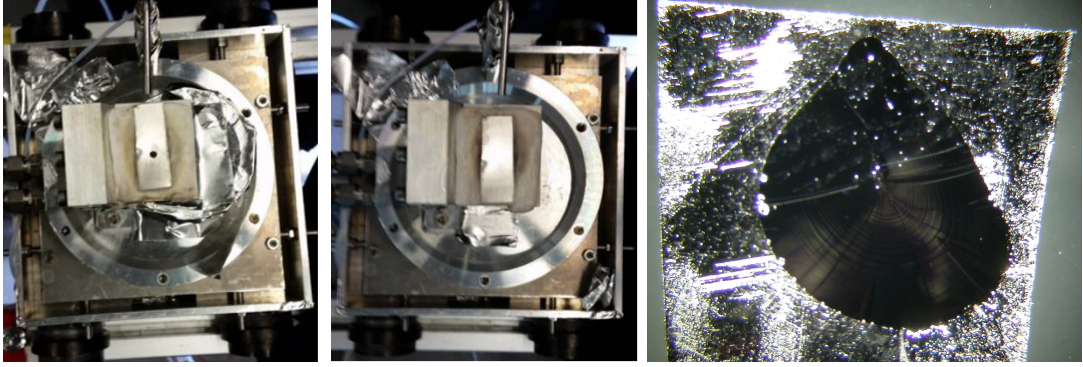


Figure 4.16: Picture of Pt sample after (left) and before (center) the experiment. Note the huge difference in ϵ_{eff} (no hole is formed in the sample!). (Right) Melted sample at higher magnification. Bright spots on dark solidified film are dust particles. Larger bright spots at the edge (center left) are molten impurities, most probably from grinding cloth used to roughen the surface of the sample before the experiment.

the sample has an identical ϵ_{eff} as the sample used for calibration. During the temperature increase at $t = 19$ min the sample comes close to the melting point and its emissivity increases by 16% [103] probably also due to restructuring of the surface by sintering. The corresponding decrease in reflectivity causes the drop of R'_1 . At $t = 21$ min the sample melts and forms a self-sustained, specular liquid film. As the two pyrometers observe the sample at different angles they now experience different ϵ_{eff} . During cooling, once the sample has solidified, both temperatures parallel each other again. However, their difference has increased markedly. This is a consequence of our calibration procedure (see later discussion) and the fact that now ϵ_{eff} is drastically different from the value during the calibration.

The brightness temperatures observed during the melting of the Platinum sample ($t \approx 21$ mins in Fig. 4.15) are $T_{\text{dmp}} = 1390$ K and $T_{\text{ref}} = 1435$ K respectively. These observations differ from the nominal value $T_{\text{mp}} = 2041.4$ K by about 651 K and 606 K. The brightness values are provided as input to Eq 3.6 to determine the effective emissivity ϵ_{eff} . Specifically, $\epsilon_{\text{eff}}(T = 2041.4 \text{ K}, \lambda = 1.2 \mu\text{m}) = 0.08$ and $\epsilon_{\text{eff}}(T = 2041.4 \text{ K}, \lambda = 1.385 \mu\text{m}) = 0.12$ were determined based on the DMP and solar-blind data respectively by applying Eq 3.6. While the ϵ_{eff} value obtained from DMP is markedly lower than the one obtained from the reference pyrometer, they both lie close to the range of emissivity values (0.2 – 0.3) reported in the literature [96, 97]. Differences between individual values are attributed to different surface morphologies of the samples used. The values of ϵ_{eff} (calculated at $t=21$ min) allow conversion from brightness temperatures to true temperatures by applying Eq 3.4, under the simplistic assumption that the emissivity remains

constant throughout the experiment. The true temperature calculated based on this assumption is plotted in Fig. 4.17. Note that melting occurred at a point in time ($t \approx 21$ mins) when T_{dmp} and T_{ref} had diverged. Hence, if the correction point is selected to coincide with the melting point, a constant offset error arises (Fig. 4.17a). Instead, selecting a correction point just prior to the divergence preserves the agreement between the two instruments but leads to invalid temperature values for the reference pyrometer (Fig. 4.17b). Note that changes observed in R_1' are caused by changes in the product $(1 - \epsilon_{\text{eff}})L_{\text{ext}}$. As in our case the stability of L_{ext} is moderate at best even on a time scale comparable to the time the data was collected R_1' is not a good indicator of relative changes in emissivity.

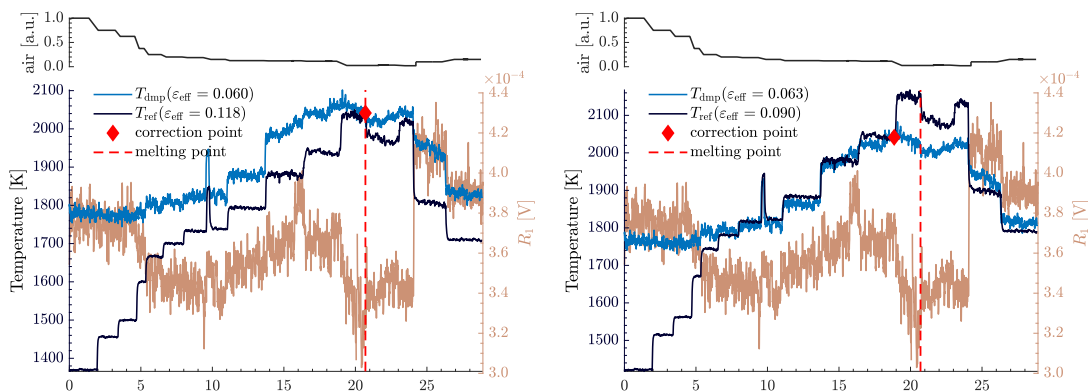


Figure 4.17: Results of Fig. 4.15 shown with corrected temperature scale. (Left) Correction point coincides with melting. (Right) Correction point prior to melting.

4.6 Error Analysis

The main systematic error is introduced during the temperature calibration where the brightness temperature ($\epsilon = 1$) is used by the two pyrometers operating at different wavelengths. In Fig. 4.18 we report the temperature error introduced as function of the emissivity error $\delta\epsilon = \epsilon_{\text{true}} - \epsilon_a$. ϵ_a , the emissivity *assumed* during the temperature calibration, is used as independent variable and ϵ_{true} , the true emissivity of the sample, as parameter. The emissivity error during the calibration was large ($\delta\epsilon \approx -0.85$) and results in a high temperature error of about 50 K (see filled circle in Fig. 4.18). Assuming a more correct emissivity (e.g. $\epsilon = 0.15$ [96, 97]) makes the systematic error negligible.

The statistical error is assessed by propagating the uncertainties introduced during calibration and during the actual measurement as outlined in the flowchart

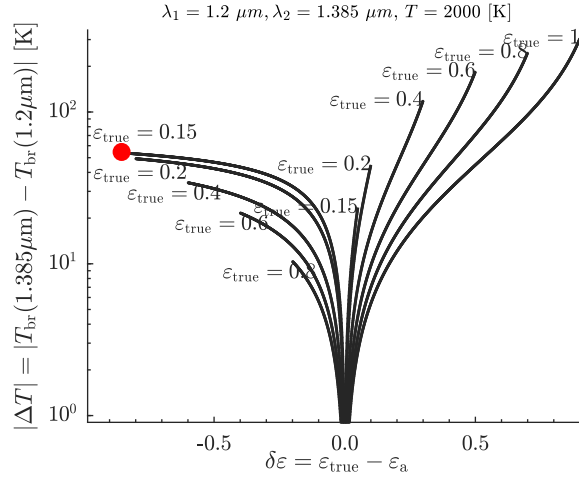


Figure 4.18: Absolute temperature error due to transfer of calibration from reference operating at $\lambda_1 = 1.385\mu\text{m}$ to DMP operating at $\lambda_2 = 1.2\mu\text{m}$ as function of emissivity error at $T_{\text{true}} = 2000$ K.

of Fig. 4.19 by a Monte-Carlo simulation. Probability densities of the input quantities are modeled after the histograms of measured data. Samples are drawn from these distributions and propagated according to Fig. 4.19 to generate samples of T_{dmp} . The same data as used in Fig. 4.5 was used to model the input data for the temperature measurement but $\epsilon = 0.12$ determined at T_{mp} of Pt was used to calculate the temperatures. The result of this simulation is reported in Fig. 4.20. In the upper part of the figure probability distributions for g_0, g_1 and k_1, k_2, k_3 are shown. Note that the skewness observed in the distributions of k_1 and k_3 is caused by the non-linear function used for temperature calibration.

At the bottom of Fig. 4.20 probability densities of the 21 values of T_{dmp} of Fig. 4.5 covering the range of 1000–1900 K are reported taking into account the statistical error of all calibration coefficients. The width of the individual distributions, i.e. the expected statistical error ($2\sigma = \text{FWHM}$) is in the range of ± 6 to ± 22 K and seems to generally decrease towards higher temperatures.

To identify the crucial calibration coefficients a local sensitivity analysis was performed. The effect of the perturbation of a single calibration constant on T_{dmp} while the other calibration constants are kept at their mode was performed. The result of these simulations is reported in Fig. 4.21. T_{dmp} is most sensitive on the quality of the temperature calibration, notably on k_2 , and much less on the gain calibration. The non-linearities of the influence of k_1 and k_3 can be traced to the inverse of Eq 4.5 and manifest themselves also in the asymmetric probability densities (see Fig. 4.20). T_{dmp} is much less sensitive to the gain calibration partly due to the small statistical error of g_0 and g_1 that results in narrow probability

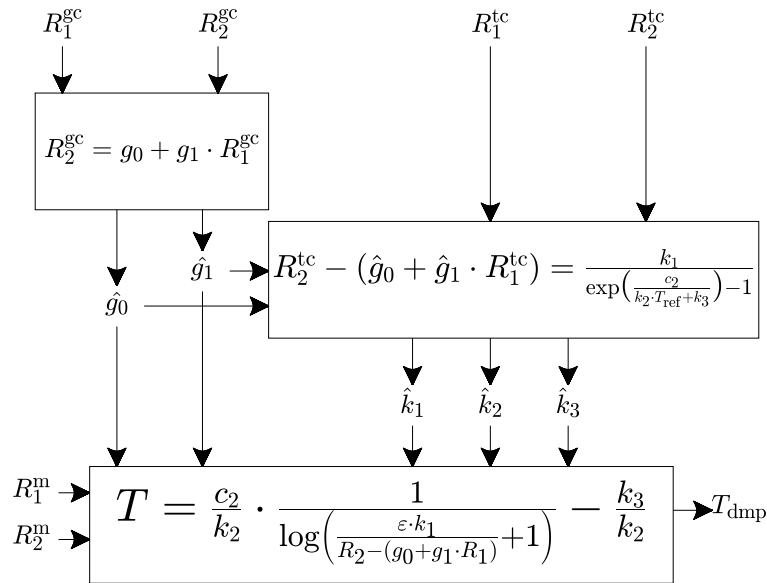


Figure 4.19: Error propagation during calibration and measurement.

density distributions. In addition their significance is damped as their logarithms occur in the inversion of Eq. 4.5.

4.7 Conclusion

The implementation of Double Modulation Pyrometry (DMP), a new radiometric method to measure the true surface temperature of radiatively heated samples, in PSI's 1 kW imaging furnace has been presented. Application of phase sensitive detection at two different frequencies allows to extract the sample's thermal emission as the difference between two measured signals. The specific geometry at the imaging furnace required the development of a mechanical modulator capable of modulating the intensities of the radiation originating in the arc *and* from the glowing electrode of the arc lamp. This was achieved by a rotating blade mounted parallel to the optical axis of the furnace. Optimization of the basic design and assessment of its characteristics was performed by Monte-Carlo geometric ray-tracing simulations. We find that a modulation depth of about 5% is achieved by a rhomboidal blade with aspect ratio 1/3 positioned 9 cm away from the optical axis.

The two-step calibration of the pyrometer is demonstrated (gain equalisation and transfer of the calibration from solar-blind pyrometer) and the systematic error of the calibration method discussed. The performance of the method is demonstrated by measurements on a thin platinum strip. Typically, front surface

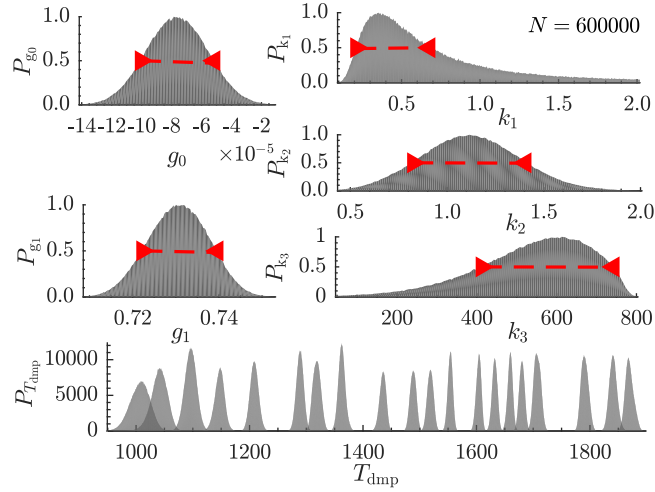


Figure 4.20: Probability density distributions of calibration constants (top) and combined uncertainty of T_{dmp} . Point bracketing the FWHH of the distributions are marked by triangles

temperatures measured by DMP coincide within about 20 K with back surface temperatures determined by the solar-blind pyrometer. Melting of platinum was observed in one of the experiments by DMP and allowed to determine $\epsilon_{\text{eff}}(T = 2041 \text{ K}, \lambda = 1.2 \mu\text{m})$ of the sample. Thus, using this value brightness temperatures could be converted to true surface temperatures.

The propagation of the uncertainties in the calibration constants and the sensitivity of the temperature measured on their error was studied by Monte-Carlo simulations. For these simulation probability densities determined from measured data were used as input. These simulations reveal that two of the temperature calibration coefficients exhibit clearly asymmetric error bounds due to the non-linear Sakuma-Hattori equation and that a single coefficient contributes to about 50% of the total temperature error.

To summarize, double modulation pyrometry works well under the harsh conditions in the imaging furnace and is able to measure surface temperatures with a typical error of about 20 K for low emission samples such as platinum. The method is also sensitive to changes of ϵ_{eff} which can be used to determine melting of the sample. A specific limitation of the implementation at the imaging furnace is that overlap of the hot zone (diameter of about 3 mm FWHH) and the measurement spot, both of similar size, is difficult and not easily maintained.

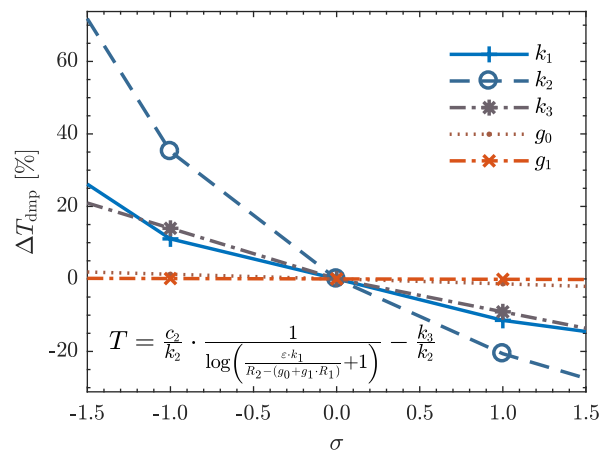


Figure 4.21: Sensitivity of T_{DMP} on the calibration coefficients. σ has been obtained from Fig. 4.20 and is asymmetric for the skewed distributions of k_1 and k_3 .

Chapter 5

Double modulation pyrometry with emissivity correction based on *in-situ* reflectance measurements applied to surfaces with dynamic optical properties²

The accuracy of radiometric temperature measurement in radiatively heated environments is severely limited by the combined effects of intense reflected radiation and unknown, dynamically changing emissivity which induces two correlated and variable error terms. While the recently demonstrated Double Modulation Pyrometry (DMP) eliminates the contribution of reflected radiation, it still suffers from the shortcomings of single-waveband pyrometry: it requires knowledge of the emissivity to retrieve the true temperature from the thermal signal. Here, we demonstrate an improvement of DMP incorporating the *in-situ* measurement of reflectance. The method is implemented in PSI's 50 kW high-flux solar simulator and used to measure the temperature of ceramic foams (SiSiC, ZrO₂, and Al₂O₃) during fast-heat-up. The enhancement allows DMP to determine the true temperature despite of a dynamically changing emissivity and to identify well-documented signature changes in ZrO₂ and Al₂O₃. The method also allows us to study the two dominant error sources by separately tracking the evolution of two error components during heat-up. Furthermore, we obtain measurements from a solar receiver, where the cavity reflection error limits measurement accuracy. DMP can be used as an accurate radiometric thermometer in the adverse conditions of concentrated radiation, and as a diagnostic tool to characterize materials with dynamic optical

²Material in this chapter has been accepted for publication in Potamias, D., Alxneit, I., Koepf, E., and Wokaun, A. (2018). Double modulation pyrometry with emissivity correction based on in-situ reflectance measurements applied to surfaces with dynamic optical properties. *Journal of Solar Energy Engineering*. <http://dx.doi.org/10.1115/1.4040842>

properties. Its simple design and ability to correct for both errors makes it a useful tool not only in solar simulators but also in concentrated solar facilities.

5.1 Introduction

The temperature T of an irradiated surface is a key parameter in many high-temperature applications. In the field of concentrated solar power (CSP), materials are exposed to concentrated solar flux I_0 and thereby brought to high temperatures. During heating they might undergo chemical reactions or experience phase changes that alter their optical properties. In this setting, experimental determination of T by radiometric measurements is challenging due to the combined effects of intense reflected radiation and an unknown, dynamically changing emissivity (ε). First, the reflected flux $\rho(t) \cdot I_0(t)$ is also sampled by the optics and contributes to the response of the instrument. This induces a variable temperature error ΔT_ρ that scales with the product $\rho(t) \cdot I_0(t)$. Second, measurement accuracy is further limited due to the often insufficient information about the thermo-optical properties of the sample. Emissivity values, especially at high temperatures, are often missing or show a large scatter since ε is sensitive to the sample's surface morphology. In addition, ε might change due to chemical reactions and phase changes.

In solar furnaces, where I_0 is provided by natural sunlight, solar blind pyrometers eliminate ΔT_ρ by measuring in one of the spectral windows, where I_0 has been significantly attenuated due to atmospheric absorption by CO_2 or H_2O (1.4, 1.9, 2.7, 4.3, and 6.0 μm) [43]. In a solar simulator, the continuous spectrum of the artificial light source prevents application of this technique. Double Modulation Pyrometry (DMP) [90] as recently demonstrated [104] in a 1 kW solar simulator is capable of eliminating the contribution of reflected radiation. The method uses phase sensitive detection to measure both, the irradiance (I) and radiosity ($I + I_{\text{th}}$) of a surface, to obtain the pure thermal signal as their difference.

Although DMP eliminates ΔT_ρ , it still suffers from the shortcomings of single-waveband pyrometry: it requires knowledge of ε to retrieve T_{true} from the thermal emission. If this knowledge is missing or if ε dynamically changes during the measurement, a variable temperature error, ΔT_ε , is introduced. Its magnitude cannot be known or verified, unless ε were to be measured. *In-situ* detection of emissivity not only eliminates ΔT_ε but also provides valuable information on the optical properties at high temperatures, where data is scarce.

Here, we demonstrate an improvement of DMP incorporating the in-situ measurement of the reflectance $\rho(t)$ used to eliminate ΔT_ε . The method is implemented in PSI's 50 kW high-flux solar simulator [28] and used to measure the temperature of different ceramic foams (SiSiC , ZrO_2 , and Al_2O_3) used as functional materials in CSP applications. SiC foams are considered as volumetric solar

receivers [105, 106] while ZrO_2 and Al_2O_3 are mostly used as high temperature insulation or construction materials. These materials were chosen due to their well-documented thermo-optical properties: ZrO_2 exhibits a very distinct drop in reflectance as a phase transition from a monoclinic to a tetragonal phase occurs at ≈ 1478 K [107]. The reflectance of Al_2O_3 changes more slowly due to chemical reactions observed e.g. on laser heated samples.[108], while SiSiC exhibits a mostly constant reflectance independent of temperature [109, 110]. Finally, we obtain temperature measurements from a cavity-type solar receiver during temperature cycling.

In the following, the theory of DMP is summarized, the methodology for the in-situ reflectance measurement is introduced and its application to dynamically correct the sample's emissivity is demonstrated. The implementation of the method in PSI'S solar simulator is then discussed. Data collected for three different ceramic foams are presented. Reflectance and emissivity errors with their temperature and wavelength dependencies are discussed and the performance of DMP is assessed.

5.2 Methodology of Double Modulation Pyrometry

A schematic of the double modulation pyrometer is reported in Fig. 5.1 while a detailed signal flow graph is presented in Fig. 5.2. The instrument records the surface radiosity of the sample that includes the reflected external radiation, I_0 , its intensity modulated by m_1 . Phase sensitive detection allows to decompose the detected radiation into the thermal radiance $\varepsilon \cdot I_{\text{bb}}(T) =: S$ and the reflected radiance $\rho \cdot I_0 =: R$. ε has to be known to extract the sample's temperature from S according to Eq. 5.1. R provides an estimated emissivity, $\hat{\varepsilon}$, relative to a reflection standard under the assumption that I_0 remains constant.

$$T = \frac{c_2}{k_2 \cdot \log \left(k_1 \cdot \left(\frac{S}{\hat{\varepsilon}} \right)^{-1} + 1 \right)} - \frac{k_3}{k_2} = f_{\mathbf{k}}(S, \hat{\varepsilon}) \quad (5.1)$$

Fig. 5.2 provides a representation of the measurement process. In the left side, the unobserved physical processes as well as the related true quantities (ρ , ε) are combined to yield the observed detector signal (center). The measurement chain (right) aims at estimating the true quantities, in order to recover ultimately a reliable temperature estimate. The square boxes represent functions (modulation function, Planck formula and Sakuma-Hattori equation) and the triangles represent scalar quantities (lock-in gain, emissivity). The colors encode relation of boxes between the two sides of the figure (the generative side and the detection side).

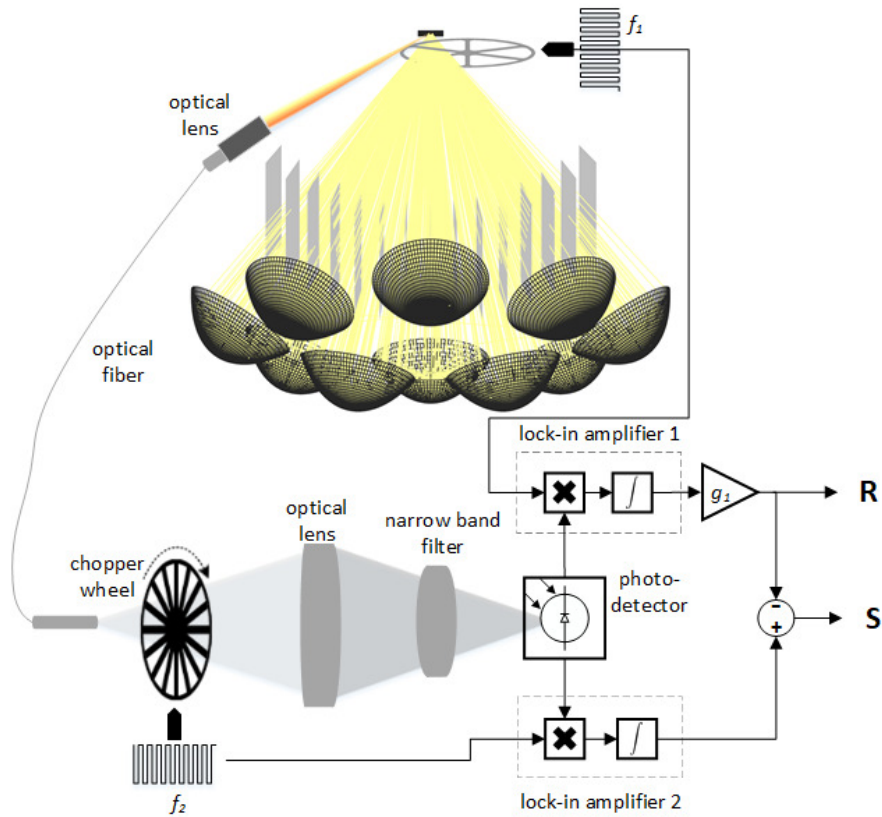


Figure 5.1: Schematic of DMP. External radiation, I_0 , passes through a chopper, m_1 , before it converges on the sample. Surface radiosity within a fixed solid angle is collected by a lens, chopped at m_2 and then projected on the detector who's output is analyzed by the two lockin amplifiers to give the raw signals R and S .

The response of a sample subjected to intense external radiation (see Fig. 5.3) is governed by its optical properties $(\alpha, \rho, \varepsilon)$. In the case of an opaque sample Kirchoff's law of thermal radiation ($\alpha = \varepsilon = 1 - \rho$) applies and the three parameters are just different representations of the same physical property. The two components of the surface radiosity, reflected radiation, R , and thermal emission, S , are also governed by the same three parameters.

The two branches of Fig. 5.3 have the error terms ΔT_ρ and ΔT_ε associated with them and contribute time-dependent, correlated errors to the measurement according to

$$T_{\text{measured}} = T_{\text{true}} + \Delta T_\varepsilon + \Delta T_\rho \quad (5.2)$$

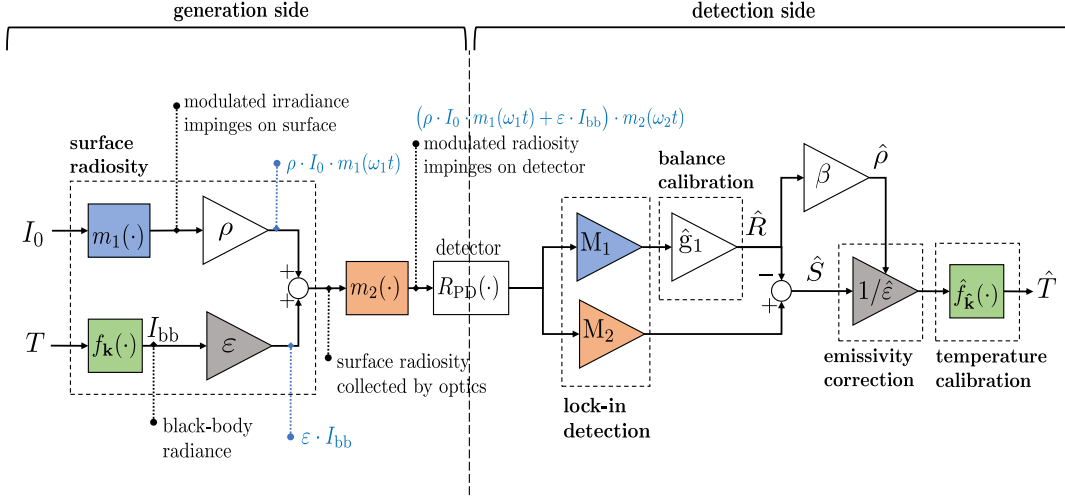


Figure 5.2: The irradiance I_0 is modulated by $m_1(t)$ and the radiosity leaving the surface $\rho I_0 + \varepsilon I_{bb}(T)$ by $m_2(t)$. The detected signal is fed into two lock-in amplifiers. LIA2 extracts the radiosity ($M_2(\rho I_0 + \varepsilon I_{bb}(T))$) and LIA1 extracts the reflected component ($M_1 \rho I_0$) which is scaled and subtracted. Thus, R is balanced to yield the thermal signal $S \propto \varepsilon I_{bb}(T)$, which is fed into the calibrated measurement equation to output \hat{T} . In green color is the Planck function generating the thermal emission (left) and the measurement equation (right) that aims to approximate that process. In gray is the true emissivity (left) and the emissivity correction (right). In blue, is the flux modulation (left) and detection (right). In orange is the radiosity modulation (left) and detection (right).

Reflectance ρ can be determined *in-situ* by measuring the attenuation of the known I_0 by the sample relative to a standard of known reflectivity. The calibration measurement with the reflectance standard is performed prior to the measurement and remains valid as long as I_0 remains constant. If I_0 fluctuates $I(t)$ must be provided simultaneously by an independent measurement as R represents the product $\rho(t) \cdot I(t)$. Simultaneously measured DNI provides this data in a solar furnace. Proper operating conditions of the solar simulator promote constant spectral irradiance $I(t)$: healthy lamp state, constant electric power and current control help to keep fluctuations to within $\approx 2\%$. [111] Current control is important as arc lamps exhibit a low dynamic impedance that amplifies small voltage fluctuations into large changes in lamp current and radiance. Furthermore, operating the lamp at 90% of the rated current further reduces output ripple to 0.2% RMS and min-

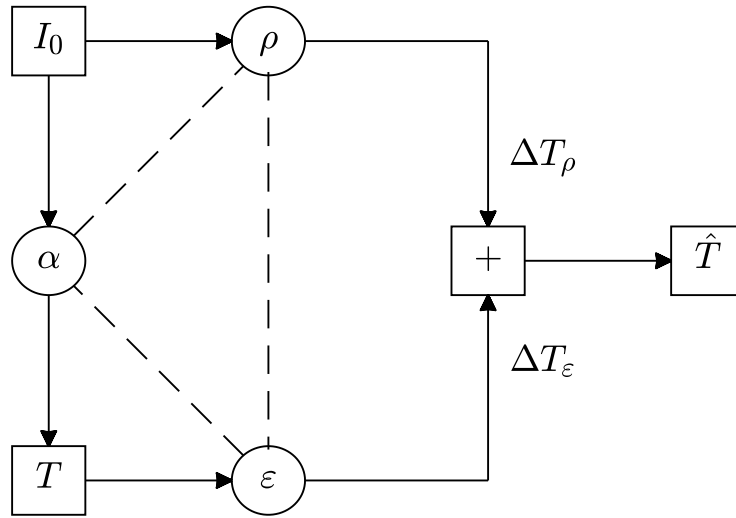


Figure 5.3: Optical properties affecting the response of an opaque sample subjected to external radiation I_0 .

imize arc-flares [112] and arc-wandering. The apparent temporal stability can be optimized by measuring at one of the arc's emission lines where saturation due to self-absorption minimizes the impact of current fluctuations.[112] A good estimate of lamp stability is obtained by measuring the reference reflectance target before and after any experiment. In our case fluctuations within $\approx 5\%$ were observed and lead to a 5% error in ρ and in ε and finally to a 1% error in temperature, assuming $\lambda = 1.2$, and $T=2000$ K according to

$$\frac{\partial T}{T} = \frac{\lambda \cdot T}{c_2} \cdot \frac{\partial \varepsilon}{\varepsilon} \quad (5.3)$$

5.3 Design of the Modulator

In this section, the design of the chopper to modulate the flux of a multi-source solar simulator [33, 37] is presented. An in-house developed ray-tracing code [99] was used to model PSI's solar simulator consisting of ten lamp-reflector pairs.

A chopper with six spokes was designed (see Fig. 5.4) to be placed at $d = 20$ cm in front of the focal plane. At this position the spots of the individual lamps have not yet converged and are bounded by an ellipsis. Radius r and the number of spokes N were chosen to fully contain the ellipsis while w was chosen comparable to the FWHH of the individual spots in the plane of the chopper. $d = 20$ cm was chosen as compromise limiting the size of the chopper while at the same time

keeping the flux on it manageable. Note, that the chopper has to be placed a some distance to the focal plane as the sample must be observed unobstructed by the chopper. Finally $w = 4$ cm, $r = 55$ cm and $N = 6$ were chosen. During operation of the chopper at 10 Hz and irradiation by 7 lamps, the temperatures measured with a FLIR E40 infra-red camera were below 400 K (Fig. 5.14).

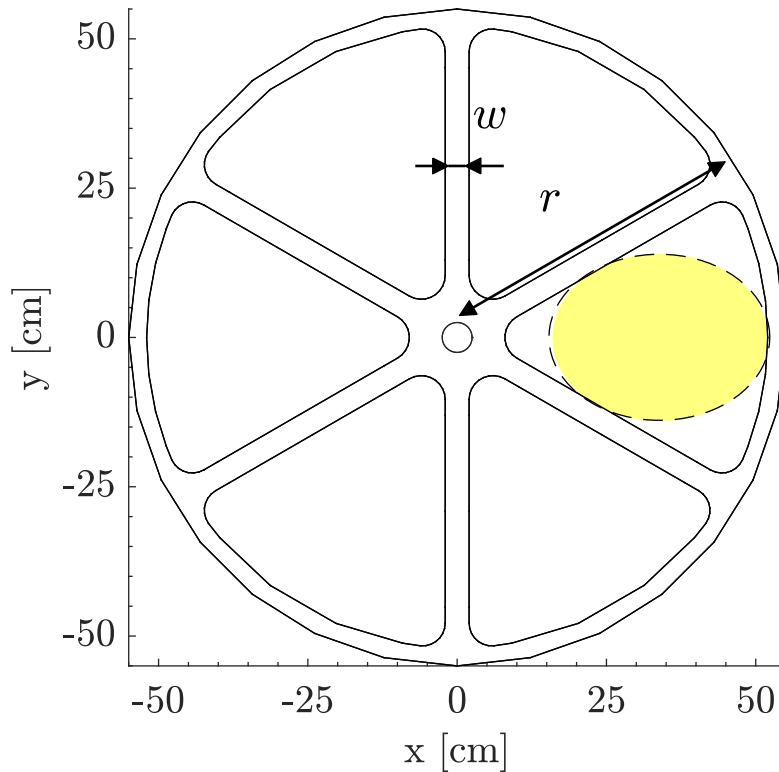


Figure 5.4: Final design of chopper wheel. Region bounding the radiative flux from the solar simulator is indicated in yellow (compare to Fig. 5.5, top).

In Fig. 5.5 the characteristic of the chopper as determined by ray-tracing is reported. At the top of the figure the situation at three different rotation angles of the chopper wheel is depicted where no (left), the central four (middle) or two (right) lamps are blocked. The resulting modulation function $m_1(t)$ is depicted in the lower part of the figure. Here, only 1/6 of a full rotation of the wheel is depicted as this contains all information due to the S_6 symmetry of the wheel.

Depending on the pattern of lamps in operation, the flux pattern intercepted by the chopper and thus the modulation function itself $m_1(t)$ changes. If for example, only the central two lamps are used, then only the central dip at 15° (see Fig. 5.5) will be present, while the lobes at 5° and 25° will be absent. Since the gain calibration constant g_1 depends on $m(t)$, calibration data have to be collected

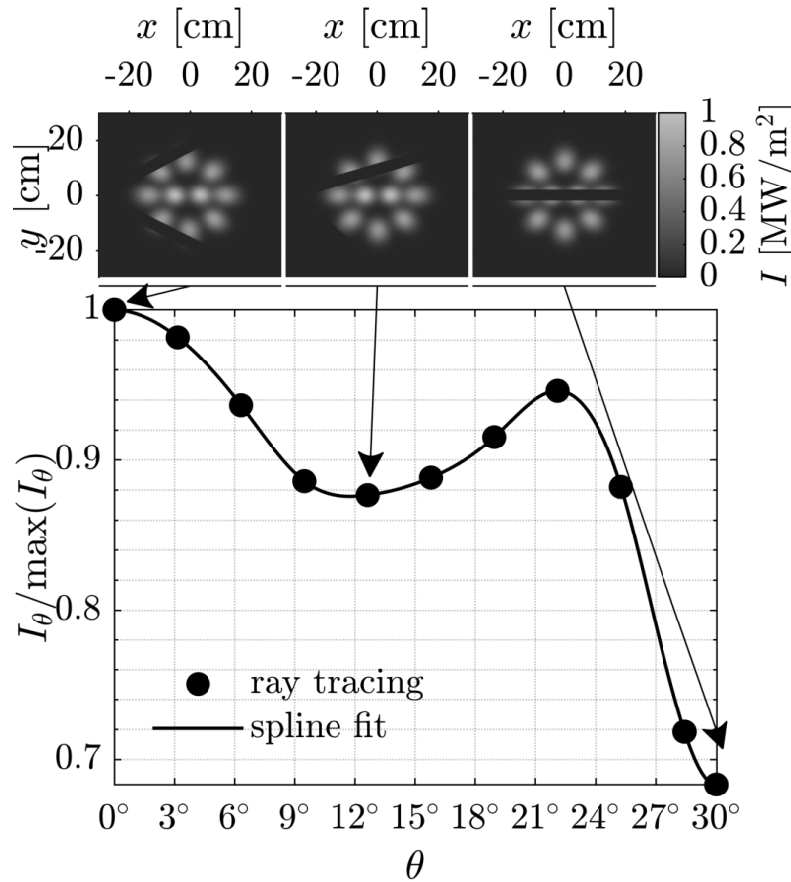


Figure 5.5: Modulation function $m_1(t)$ determined by monte-carlo ray-tracing for all ten lamps used.

for all foreseen lamp configurations.

In Fig. 5.6 the value of the gain calibration constant g_1 is reported for different configurations and for different operation wavelengths. A small value of g_1 results from a lamp configuration where the modulation depth is large and therefore the reflected external radiation is easily detected. All curves loosely follow the relative sensitivity of the detection as reported in Fig. 5.7. For a detailed discussion of the calibration procedures required for the instrument the reader is referred to Section 4.3.

5.4 Experimental Setup

The double modulation pyrometer was installed at PSI's solar simulator in a configuration reported in Fig. 5.1 (top). The samples are observed at an oblique

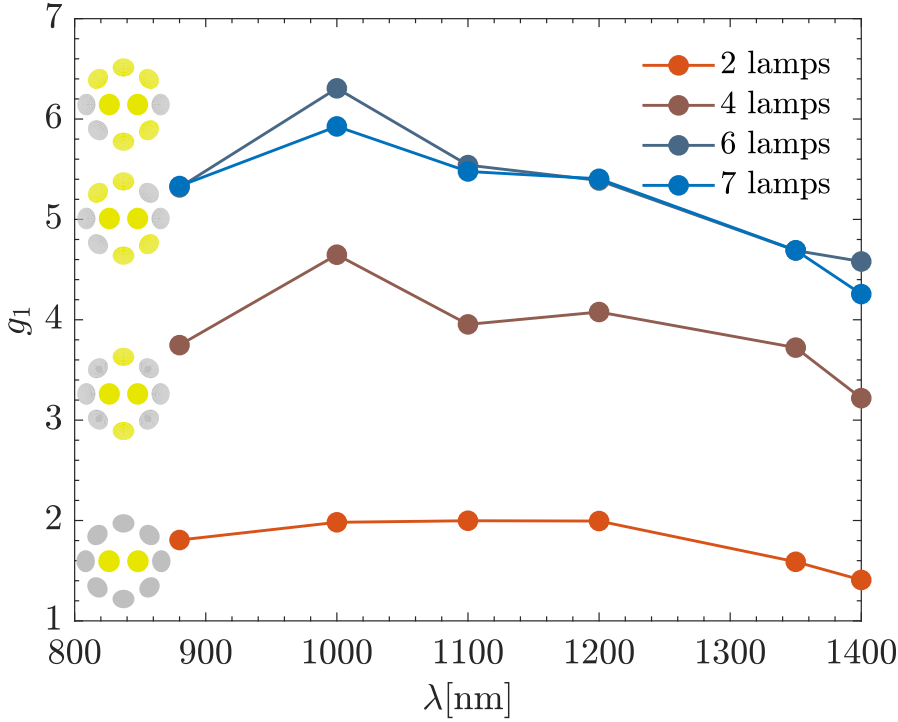


Figure 5.6: Calibration constant g_1 for different configurations of active light sources and operation wavelengths.

angle of $\Theta = 57^\circ$ that results in an elliptical observation area of approximately $0.5 \times 0.25 \text{ cm}^2$ comprising ≈ 9 pores. Radiation emerging from the sample is collected by a lens, coupled into an optical fiber (Thorlabs 0.22 NA, diameter $105 \mu\text{m}$) and focused by a double-achromat onto an InGaAs detector (Thorlabs PDA20CS-EC) sensitive in the wavelength range 800–1700 nm.

Narrow wavelength bands are selected by $\varnothing 1''$ dielectric narrow bandpass filters centered at $\lambda = 880, 1000, 1100, 1200, 1350, 1400 \text{ nm}$ (FB880-10, FB1000-10, FB1100-10, FB1200-10, FB1350-12, FB1400-12) mounted on a filter wheel. Transmission curves of the filters together with the spectral sensitivity of the detector and the lamp's emission spectrum are reported in Fig. 5.7. The resulting relative sensitivities of the instrument are indicated by \blacklozenge in the same figure.

Three ceramic foams, SiSiC, ZrO_2 , and Al_2O_3 purchased from EngiCer SA, Balerna, Switzerland were tested in the form of small cylinders of $6.5 \times 2.5 \text{ cm}^2$ ($d \times h$) with 20 pores per inch³. The samples were placed in focal plane of the simulator inside of an insulating structure made from Al_2O_3 bricks. Samples were considered opaque based on a study [113] stating that ZrO_2 species thicker than $\approx 0.41 \text{ cm}$ at room temperature and thicker than $\approx 0.13 \text{ cm}$ close to melting are opaque in the visible. A B-type thermocouple, attached to the back of the samples

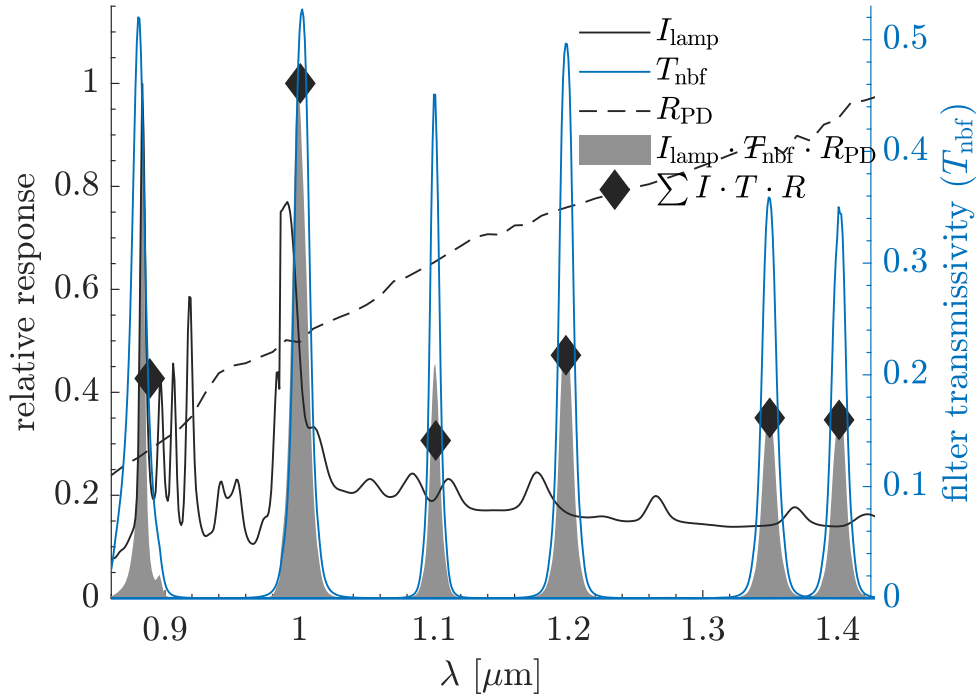


Figure 5.7: Relative spectral sensitivity of the DMP calculated from the spectral sensitivity of the detector (λ), the transmissivity of the filters and the spectral irradiance of the Xenon arc-lamp.

provides a lower bound of the temperature.

5.5 Results

In the following surface temperatures of the three ceramic foams measured by DMP while they are heated to around 2000 K are reported. Three temperature variants (see Eqs. 5.4) computed by use of Eq. 5.1 are reported to illustrate the advantage of DMP over other pyrometric methods. First, T_{pyro} (see Eq. 5.4a) based on a sensor that responds to the sum $S(t) + R(t)$ such as a standard pyrometer or a solar-blind pyrometer used in a solar simulator. Second, $T_{\text{dmp}}^-(t)$ (see Eq. 5.4b) based on a sensor that correctly responds only to $S(t)$. This is the case for a solar blind pyrometer operated in a solar concentrator. For simplicity $\varepsilon = 1$ is assumed for these two cases and thus T_{pyro} and $T_{\text{dmp}}^-(t)$ both correspond to brightness temperatures. Finally, $T_{\text{dmp}}^{\sim}(t)$ (see Eq. 5.4c) based on a sensor that responds to the thermal component only and uses the measured reflectivity $\hat{\rho}(t)$

to provide the true surface temperature.

$$T_{\text{pyro}}(t) = f_{\hat{\mathbf{k}}}(S(t) + R(t), \varepsilon = 1) \quad (5.4a)$$

$$T_{\text{dmp}}^-(t) = f_{\hat{\mathbf{k}}}(S(t), \varepsilon(t) = 1) \quad (5.4b)$$

$$T_{\text{dmp}}^{\sim}(t) = f_{\hat{\mathbf{k}}}(S(t), \hat{\varepsilon}(t) = 1 - \hat{\rho}(t)) \quad (5.4c)$$

All experiments start with the sample at room temperature, the lamps already on and in steady state and the shutter fully closed. At $t = 0$ the shutter starts to open and becomes fully open after about five seconds. As the shutter opens irradiance reaches I_0 . While the shutter opens reflections from the individual blades pass over the sample and the readings cannot be trusted during this time. More importantly, as I_0 is assumed constant to allow measuring the emissivity, $T_{\text{dmp}}^{\sim}(t)$ will be erroneous. In the following figures, this interval is marked grey. $\rho(t)$ is reported for several wavelength while temperatures are only reported for a single wavelength. Note that the confidence bands include only the temperature uncertainty that is caused by the uncertainty in the estimation of the temperature calibration coefficients k_1, k_2, k_3 .

In Fig. 5.8 the surface temperatures of Al_2O_3 is reported while the sample is radiatively heated. As the shutter of the solar simulator opens, all temperatures rise very fast. Once the shutter is fully open T_{pyro} is highest but continues to rise gradually until it becomes constant ($T = 1850$ K) at around 56 s. T_{dmp}^- exhibits a similar behavior. However, it only reads 1000 K after the shutter has opened but then converges to a temperature only slightly below T_{pyro} . The difference between these two temperatures corresponds to ΔT_{ρ} . ΔT_{ρ} becomes smaller in course of the experiment as the thermal signal S increases because the sample's temperature continues to increase. During the same time the reflectivity of Al_2O_3 decreases from $\rho = 0.85$ to $\rho = 0.4$ decreasing the relative contribution of R but increasing the relative contribution of S as $\varepsilon = 1 - \rho$. A rather different temperature evolution is recorded by $T_{\text{dmp}}^{\sim}(t)$. This temperature reading shows that the sample's surface temperature increases at a rather constant rate until it reaches a steady temperature of 2150 K after about 30 s. The quite distinct difference between T_{dmp}^- and $T_{\text{dmp}}^{\sim}(t)$ that constitutes ΔT_{ε} is evidence of the strong variation of alumina's reflectivity in accordance with previous experiments [114], where a spectral-directional emittance of 0.1360 was measured at 60° , $\lambda = 2\mu\text{m}$, 823 K.

After the experiment we found that the sample shows evidence of surface melting. With the melting point of Al_2O_3 at 2345 K this gives more confidence to the temperatures of ≈ 2200 K measured by T_{dmp}^{\sim} which are more consistent with the observed melting point than the other measurements. Temperatures recorded by

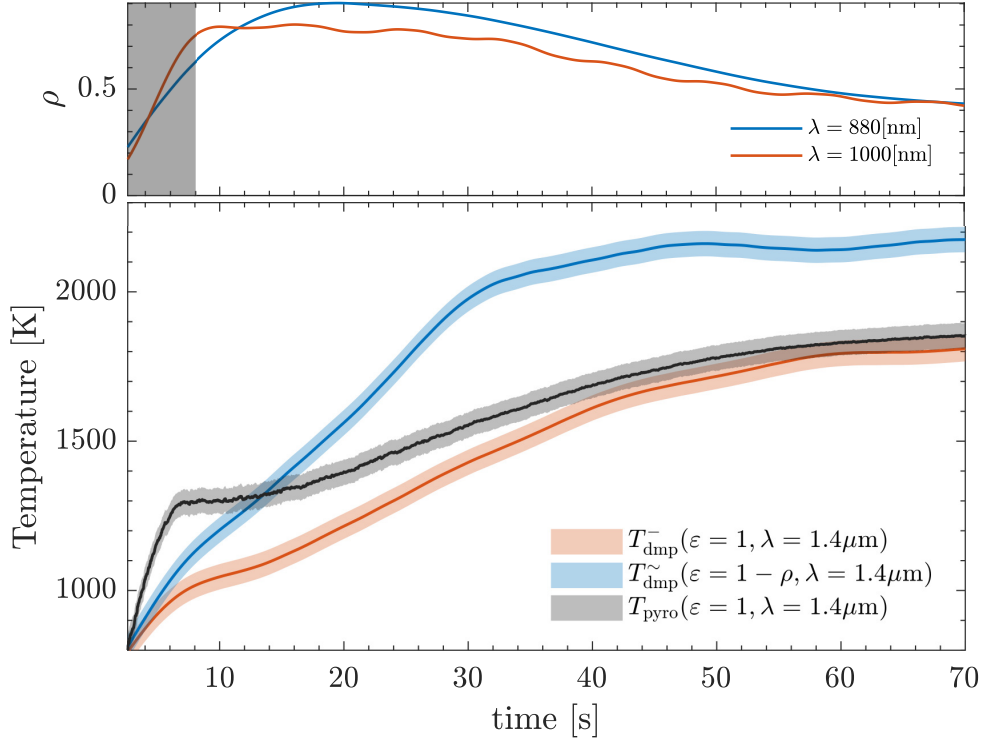


Figure 5.8: Temperatures and reflectivity measured on Al_2O_3 during heating of the sample.

the embedded thermocouple are not shown in the figure and remained below the ones determined pyrometrically due to the relatively low heat conductance of the porous sample.

In Fig. 5.9 surface temperatures measured on ZrO_2 foam under nominally identical conditions as for the Al_2O_3 sample are reported. In this case, all temperatures exhibit a very similar history. They rise very fast and reach steady state at about 10–15 s. All temperatures exhibit a distinct kink at $t = 7$ s that coincide with the sharp maxima in the reflectivity curves reported in Fig. 5.9 (top). The large decrease in reflectivity by between $\approx 70\%$ at $\lambda = 880$ nm and 45% at $\lambda = 1200$ nm is caused by the transition from the monoclinic to the tetragonal phase that becomes thermodynamically stable at ≈ 1478 K [107]. The observed behavior is consistent with multi-wavelength pyrometry measurements [51] of ZrO_2 felt in a solar furnace. In these experiments the reflectivity decreased abruptly by $\approx 90\%$ from 0.95 down to 0.5, once temperature had exceeded $T \approx 2000$ K. In addition, the high-temperature reflectance values in Fig. 5.9 agree with reported [113] values of 0.1 and 0.2 at 2715 K and 3010 K respectively.

Because the change in the optical properties of ZrO_2 is caused by a phase change

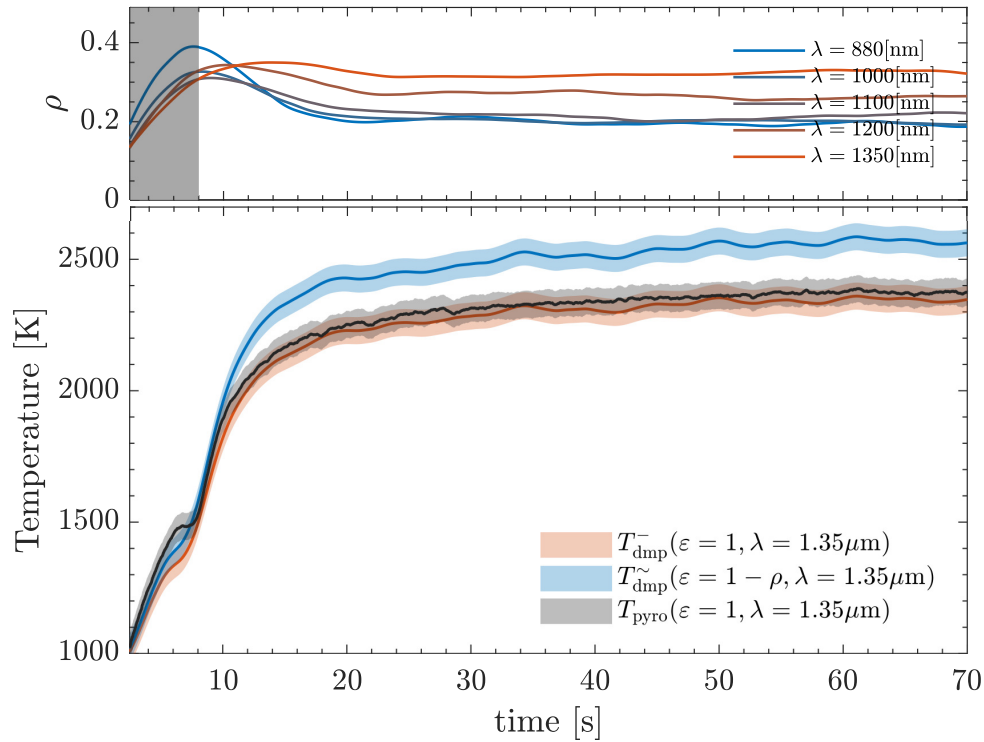


Figure 5.9: Temperatures and reflectivity measured on ZrO_2 during heating of the sample.

it is much faster than observed for alumina where it is most probably caused by (slow) partial reduction of the sample. Thus, during most of the measurement data could be collected under steady state conditions with constant errors ΔT_ρ and ΔT_ε . Thus, the history recorded by the three temperatures is identical, they only differ in their absolute values with T_{dmp}^\sim falling between the two brightness temperatures.

SiSiC (see Fig. 5.10) represents a benign case with low and constant reflectivity and correspondingly high emissivity. Reflectance and emissivity errors are negligible as shown by the convergence of the three temperatures reported in Fig. 5.10. Still, ρ increases during the experiment, most probably during the formation of an SiO_2 surface layer but the effect on the different temperatures is small as expected from Eq. 5.3.

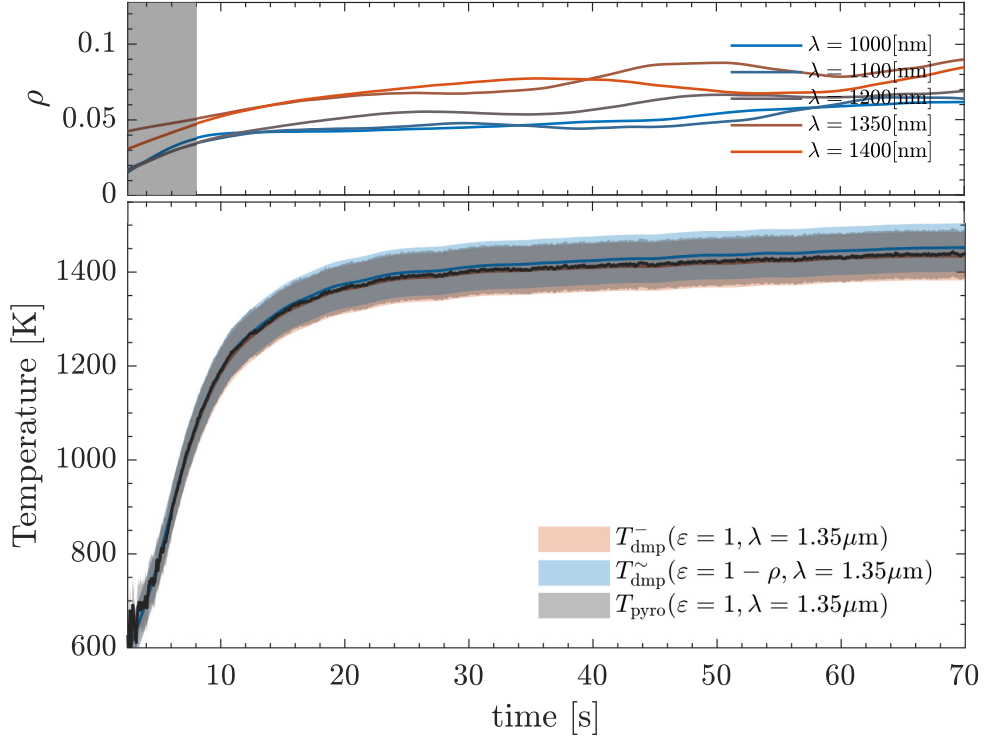


Figure 5.10: Temperatures and reflectivity measured on SiSiC during heating of the sample.

5.6 Discussion of the error terms

An error in the optical properties of the sample affects the two signal components, R and S , in opposite ways as is illustrated in Fig. 5.3. To facilitate the following discussion, the two error components, ΔT_ρ and ΔT_ε , were extracted from the data presented in Fig 5.8 and reported in Fig. 5.11.

ΔT_ρ represents the reflectance error and describes the overestimate of the temperature by attributing $R = \rho \cdot I_0$ to the thermal emission. For a high reflectance samples like Al_2O_3 this error can be huge while for a low reflectance like SiSiC it might be negligible.

ΔT_ε is caused by the mismatch between the true value, ε , and an uninformed estimate, $\hat{\varepsilon}$. If we take the brightness temperature ($\varepsilon = 1$) as reference this error term is always of opposite sign (see Fig. 5.11) as ΔT_ρ and the two errors tend to cancel out in favorable circumstances. Thus, using an educated guess for ε often leads to rather good temperature measurements.

However, if $\varepsilon(t)$ is not constant the situation changes completely. Relying on T_{pyro} as temperature indicator, the alumina sample seems to be heated very

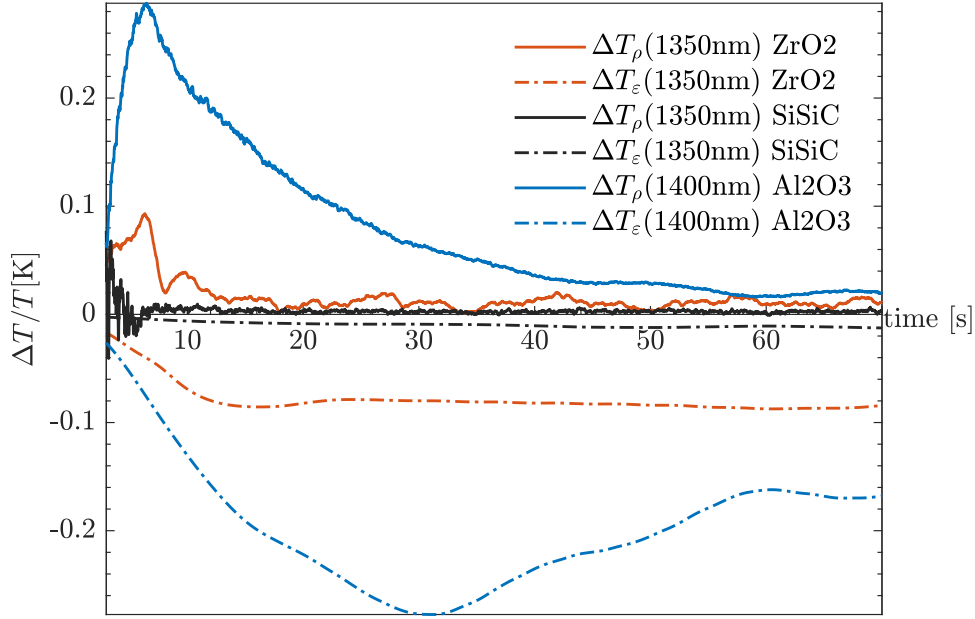


Figure 5.11: Evolution of reflectance (ΔT_ρ) and emissivity (ΔT_ε) induced temperature errors extracted from data of Fig 5.8.

rapidly to almost its final temperature within 8 s (see Fig. 5.8). Then, temperature increases only slightly during the next 45 s. Similar conclusions can be drawn from T_{dmp}^- . However the temperature increase after the fast initial heating is much more pronounced. The correct temperature history is only revealed by T_{dmp}^\sim : The sample takes 32 s to reach its steady state at an almost constant rate of heating!

In the case of Al_2O_3 , ΔT_ρ is dominant at low temperatures and becomes smaller as the experiment continues and temperature increases. This is a combined effect of the thermal radiation's exponential decrease with temperature while at the same time R increases due to increased reflectance. Together they explain the fast rise of T_{pyro} well above T_{dmp}^- within the first five seconds of the experiment.

In Fig. 5.12, the ratio of thermal to reflected components is reported as function of T_{dmp}^\sim for the different filters applied. For each filter, the lines trace an exponential function of the form $a \cdot \exp(b \cdot T)$ that is fitted to the point cloud of measured data. It provides a measure of the relative magnitude of $\Delta T_\rho(t)$, and shows how strongly it varies with temperature and wavelength. It generally increases exponentially with temperature, not only due the exponential increase of the thermal emission, but also due to the decreasing reflectance at high temperatures. Note that it is

also affected by the wavelength dependence of the xenon-arc spectrum, T_0 (see Fig. 5.7).

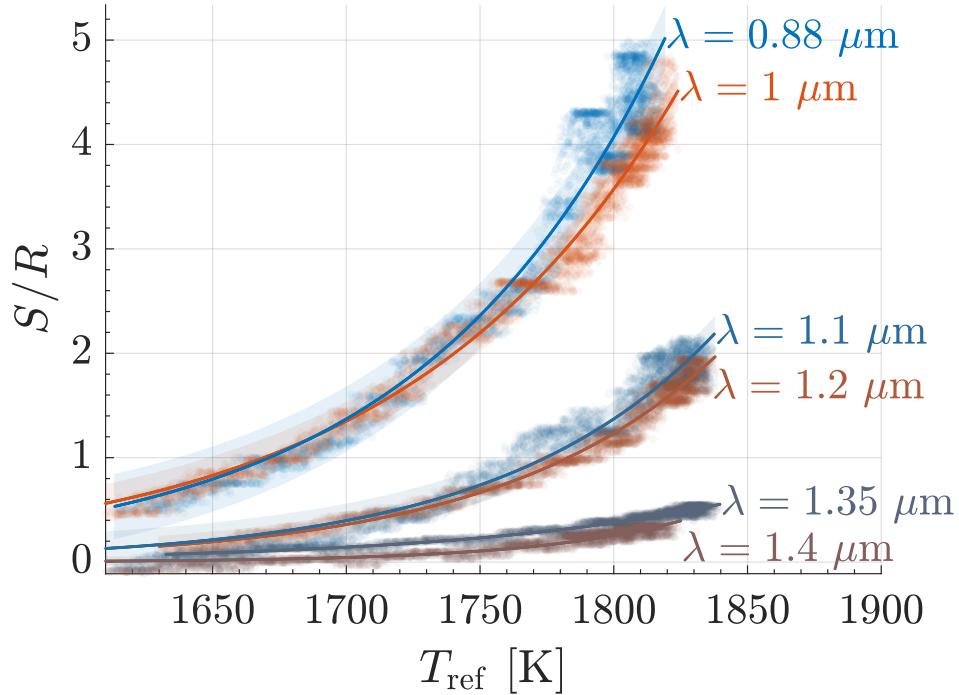


Figure 5.12: Ratio of thermal to reflected signals at all operating wavelengths as function of temperature based on the data presented in Fig. 5.8.

DMP offers relative freedom in selecting operating wavebands to suit the experimenter's needs. Note that the reflectance measurements are limited by the intensity of the source (Xenon-arc or solar radiation). The waveband selection entails a trade-off between the resolution of thermal (S) and reflected (R) signals (Fig. 5.12). Since S follows Planck's law its resolution is enhanced at longer wavebands (for the foreseen temperature range of 1000-3000 K), while R , whose strength scales with the Xenon-arc spectrum, is enhanced at shorter wavebands, where the Xenon-arc intensity peaks.

5.7 Temperature measurement in a solar receiver

In this section, we depart from the setup of free-standing surfaces and use DMP to measure the temperature of a solar receiver that comprises a cavity arrangement whose walls are made of CeO_2 in the form of a reticulated porous ceramic (RPC)

foam. Such reactors can be used in thermochemical redox cycle to split H_2O and CO_2 [115].

The receiver is shown in Fig. 5.13. DMP observes the inside of the cavity through the circular quartz window at an oblique angle ($\theta = 57^\circ$) with respect to the optical axis. The signal collected by the optics contains the following contributions:

$$I = \tau_w \left(\int_{\Omega} \rho(r', r) I_{\text{th}}(r') dr' + \varepsilon_s I_{\text{bb}}(\lambda, T_s) + \rho_s \cdot \tau_w \cdot I_0 \right) + \varepsilon_w I_{\text{bb}}(\lambda, T_w) + \rho_w I_0 \quad , \quad (5.5)$$

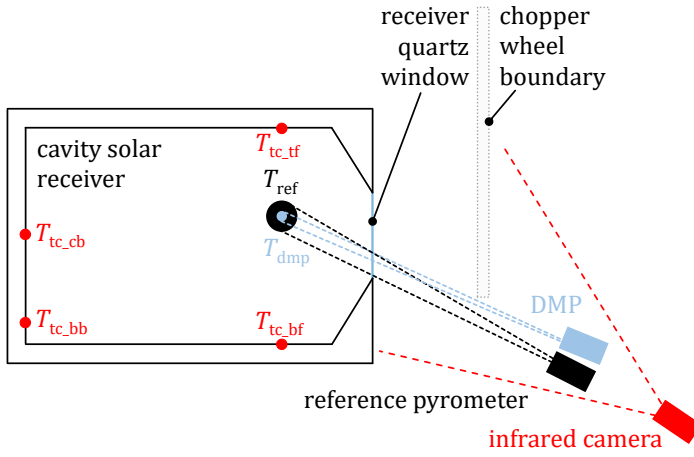


Figure 5.13: A simplified cross-section schematic of the reactor's cavity and window. The measurement spots of double modulation (blue) and solar blind (black) pyrometers are indicated on the sidewall of the cavity. The thermocouple locations are marked in red.

where τ_w , ε_w , ρ_w denote the transmittance, reflectance and emittance of the window at DMP's observation angle, and the subscript s denotes the spot observed by DMP. The last term ($\rho_w I_0$) is the lamp radiance (I_0) reflected off the front surface of the window, which can be neglected due to the oblique observation angle, and would be filtered out by DMP. The second term ($\varepsilon_w I_{\text{bb}}(\lambda, T_w)$) is due to the thermal self-emission of the window and is also negligible since typically $T_w \ll T_s$ (Fig. 5.14). The first term contains the transmissivity of the window multiplied by the radiosity of the observed spot, i.e. the thermal self-emission ($\varepsilon_s I_{\text{bb}}(\lambda, T_s)$) plus the spatial integral of the thermal radiation emanating from the rest of the

cavity walls within the domain Ω that has been reflected off the spot. The integral causes the cavity reflection error and prevents measuring the reflectivity of the cavity wall. The effect of the cavity on the observed spot can be accounted for by considering an effective value for emissivity in Eq. 5.1. Furthermore, the external transmittance of the glass window is calculated by use of the Fresnel equations for $n_{\text{glass}} = 1.5$, $n_{\text{air}} = 1$ and $\theta = 57^\circ$ to be $T \approx 0.86$. Hence, both cavity and window effects can be included in Eq. 5.1 by scaling the thermal signal $S(t)$ by the product of effective emittance and window transmittance, so that $T = f_{\mathbf{k}}(S, \hat{\varepsilon} \cdot \tau)$.

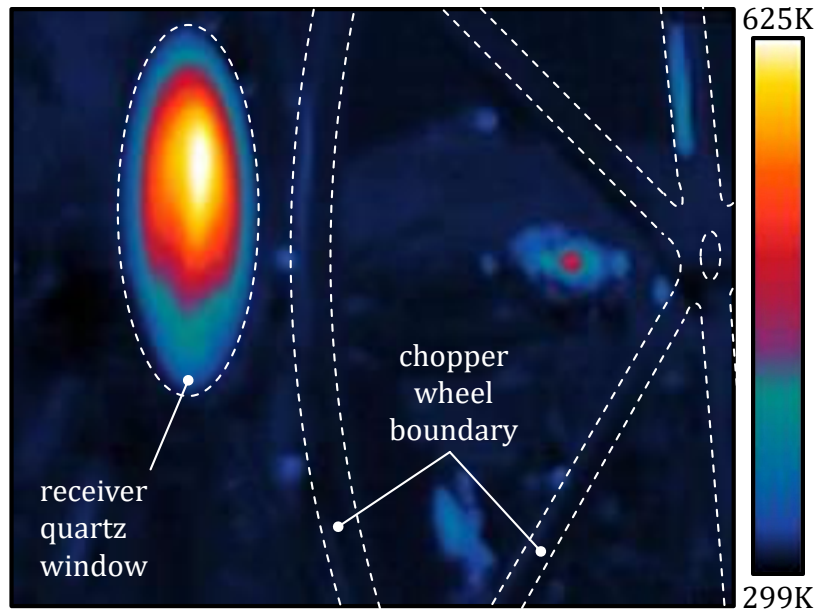


Figure 5.14: Temperature distribution of the glass window. The thermal emission can be neglected since $T_{w,\text{max}} = 533 \text{ K} \ll 1500 \text{ K}$. Furthermore, one can deduce by observing the surface of the chopper wheel that its surface is much colder.

A method has been proposed [44] that establishes uncertainty intervals for measurements in such a setup. It requires partitioning the inside surface into isothermal sectors whose emissivities are known, calculating their view factors either analytically or by Monte-Carlo simulation. Temperature and error are obtained from data collected on the individual sectors. Here, we do not quantify the cavity effect but establish an uncertainty interval bound by assuming the two extreme cases, no cavity when $\varepsilon_{\text{CeO}_2} = 0.6$ and a black-body cavity when $\varepsilon_{\text{CeO}_2} = 1$ taking into account the limited transmittance of the window in both cases. This estimate

could serve as a valuable base-case scenario in reactor modelling. Note, that the uncertainty interval can be further reduced by using ray-tracing to approximate the integral in Eq. 5.5 for a specific reactor model.

The temperature data collected from four thermocouples, the reference pyrometer and DMP during two consecutive heating cycles are plotted in Fig. 5.15. Both T_{ref} and T_{dmp} have been computed assuming $\varepsilon_s = 0.6$ and $\tau_w = 0.86$. The location of the sensors (Fig. 5.13) in the cavity affects the relative values of observed temperatures. $T_{\text{tc,cb}}$ is located in the back of the cavity, where due to direct irradiation of the solar simulator the highest temperatures are reached. During heat-up from 0 hours until 1.2 hours and from 2 hours until 3 hours into the experiment the slope of the curves from the two pyrometers (T_{dmp} and T_{ref}) matches the slope of $T_{\text{tc,cb}}$.

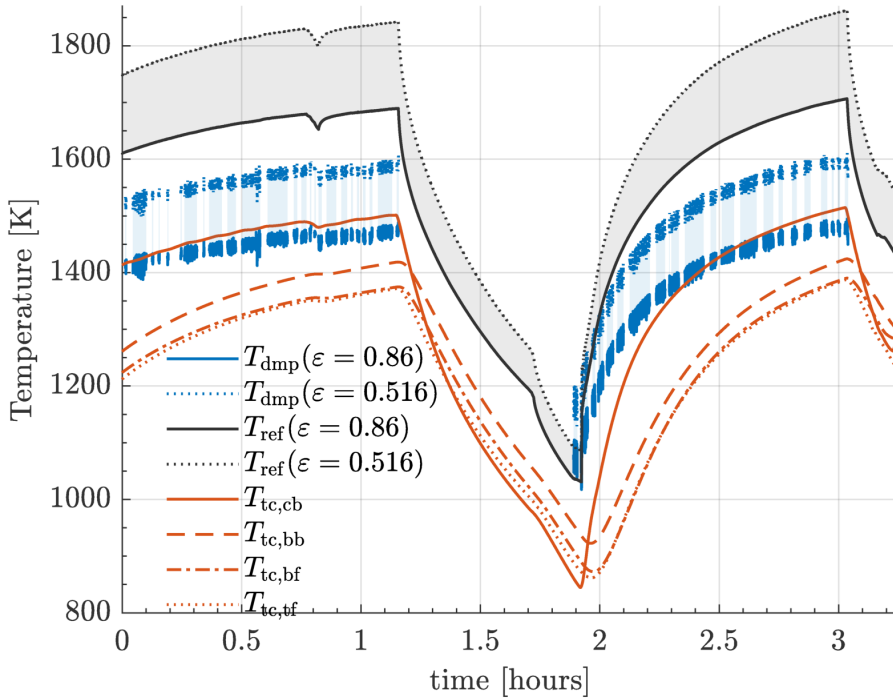


Figure 5.15: Temperature measurements during two heating cycles. The location of the sensors is indicated in Fig. 5.13.

Even though the side-wall of the reactor, monitored by T_{dmp} and T_{ref} , is significantly colder than the directly irradiated back side where $T_{\text{tc,cb}}$ is located, T_{dmp} and T_{ref} are significantly higher ≈ 100 K than $T_{\text{tc,cb}}$ throughout the experiment. Note, that this difference also persists during cooling (from 1.2 hours until 1.9 hours) when all lamps are off, so it is not due to reflected flux affecting T_{ref} . On the one

hand, thermocouples tend to underestimate the surface temperature due to their offset of more than 4 cm from the surface. On the other hand, DMP overestimates the surface temperature due to the presence of the cavity reflection error (integral in Eq. 5.5).

It is evident that when measuring inside a cavity receiver, not all parts are directly irradiated and hence the external flux signal is weak I_0 , so that $\rho_s \cdot I_0 \rightarrow 0$. Under these conditions, first, dynamic emissivity correction is not possible and one has to assume an emissivity value, which results in ΔT_ε error, as discussed in Section 5.6. Second, the cavity effect tends to reduce the magnitude of ΔT_ε since the observed spot more closely approximates a black-body. Third, due to both increased effective emissivity and diffuse irradiation, the reflection error in a conventional solar-blind pyrometer (T_{ref}) is minimal.

5.8 Conclusion

Here, we demonstrated emissivity correction utilizing a simple single-waveband technique. The results build on the reflectance correction implemented in DMP [104]. Since DMP already detects the reflected component R , and samples are typically irradiated in a hemispherical configuration, the functionality to calculate ε is readily built-into the instrument and does not require additional equipment or calibration steps. This is a departure from other methods (multiwavelength pyrometry, FAMP, pyro-reflectometry), where emissivity correction has been implemented in relatively complex set-ups requiring concurrent measurements of multiple wavebands.

We uncovered experimentally the two dominant error sources affecting temperature measurement under concentrated flux and tracked their individual error components, ΔT_ρ and ΔT_ε , during dynamic experiments involving fast heat-up of three representative ceramic materials (Al_2O_3 , SiSiC and ZrO_2). We found that the errors greatly varied with sample and temperature levels. These results highlight the severity of the ΔT_ε error a conventional pyrometric technique might incur due to lack of prior knowledge of emissivity. The enhancement allowed DMP to track the true temperature despite the variable ΔT_ρ and ΔT_ε errors. These findings demonstrate that DMP is a simple method that enables the temperature of samples with dynamic emissivity to be accurately measured in the adverse conditions of a solar simulator. Furthermore, we test the method in a solar receiver, where the presence of a quartz window and cavity reflection error enhance the measurement uncertainty. Due to diffusion of direct irradiation inside the cavity, the reflected component ($\rho_s \cdot I_0 \rightarrow 0$) is too weak to allow emissivity correction. Nevertheless, the cavity effect dampens the emissivity error.

Chapter 6

Assessment of Double Modulation Pyrometry as a diagnostic tool for use in concentrated solar facilities³

Double modulation pyrometry (DMP) is a pyrometric method that was developed to enable radiometric temperature measurements in solar simulators, where solar blind pyrometry (SBP) cannot be applied due to the continuous spectrum of the artificial light source. DMP has been characterized in two solar simulator facilities, but no direct comparison to a reference pyrometer was performed so far due to the limitations of applying pyrometry in solar simulators. Here, we report on a series of experiments conducted in concentrated natural sunlight where reference pyrometers are available. They demonstrate the performance enhancement gained by utilizing the inherent advantages of DMP, i.e. the *in-situ* reflectance measurement and the freedom to select the operation wavelength.

6.1 Introduction

In a typical experiment conducted under concentrated solar radiation the surface of interest with reflectance ρ is irradiated by a flux I_0 of a few thousand suns (1 sun = 1 kW/m²). In this situation, non-contact temperature measurement is challenging: The strong reflected component $\rho \cdot I_0$ is also detected by the optics of a conventional pyrometer and erroneously attributed to the thermal signal, causing a large error. Solar blind pyrometry (SBP) overcomes the problem by sampling the emitted thermal radiation in a narrow wavelength band where the solar spectrum has been attenuated by atmospheric absorption, and thus $\rho \cdot I_0$ is minimal. Alternatively, wavelengths where the solar radiation is absorbed by the concentration

³Material in this chapter has been submitted for publication as Potamias, D., Alxneit, I. and Wokaun, A. (2018). Assessment of Double Modulation Pyrometry as a diagnostic tool for use in concentrated solar facilities. *Solar Energy*

optics can be used. Application of SBP at $\lambda = 1.39 \mu\text{m}$ was demonstrated in [46], where a sample of high emittance was measured, with a relative bias of $\approx 5\%$ at 1223 K. Usually, the dominant measurement uncertainty results from the unknown emittance ε of the sample, particularly when low ε samples are measured. In [82], temperature measurements from two SBP observing the sample over a range of temperatures were combined to estimate ε and T . Thus, the method enables measurements where the emittance is unknown. ε has to be assumed independent of temperature but may be wavelength dependent. Nevertheless, to enable satisfactory convergence the method requires measurements spanning a wide range of temperatures, while assuming temperature independence of ε .

DMP was developed [90] to enable temperature measurement in solar simulators, where SBP cannot be applied due to the continuous spectrum of the xenon-arc light source. While SBP measures in the absence of external radiation, DMP actively tracks and filters out the reflected flux $\rho \cdot I_0$. Active filtering offers two distinct advantages that were recently assessed in a solar simulator facility [104, 116]. First, accuracy can be improved by the *in-situ* reflectance measurement. Second, the user is no longer limited to operate at one of the few solar-blind compatible wavelengths. Instead, DMP offers flexibility to select any wavelength band within the near-IR region of the spectrum that optimally fits the experimenter's need, in matching sample properties or falling within the range where emissivity data is available. Hence, these characteristics make DMP an interesting diagnostic tool also for experiments conducted in concentrated natural sunlight.

The objective of this paper is two-fold. First, to demonstrate how the free choice of the operation wavelength and the *in-situ* measurement of ρ can improve temperature diagnostics in a solar furnace facility. We demonstrate that $\rho(t)$ can be measured on-line by utilizing the readily available data of direct normal irradiance (DNI) proportional to $I_0(t)$. Second, to document the direct comparison of DMP (T_{dmp}) against a reference solar blind pyrometer on several samples with different optical and thermal characteristics. Such a direct comparison between the DMP and a reference pyrometer has not been possible so far in solar simulators, as no reference method insensitive the intense reflected radiation exists. So far, only measurements on a thin platinum sample that was assumed isothermal, where DMP observes the irradiated surface, while a conventional pyrometer observes the back side of the sample were reported [104].

In the following, we will present the methodology of DMP and elaborate on how usage of DNI data can be used to determine *in-situ* the reflectance of the samples. Then, we will introduce the experimental setup, present the relevant material properties of the samples and elaborate on the calibration and measurement procedure. Finally, we present temperature and reflectance measurements from experiments conducted on two metallic samples (copper, stainless steel 310S) and

three oxide ceramics (Al_2TiO_5 , ZrO_2 , CeO_2) and discuss the relative performance of DMP.

6.2 Theory

6.2.1 Double Modulation Pyrometer

Fig. 6.1 shows DMP installed in a vertical solar furnace at PROMES-CNRS: Quasi-parallel radiation from the heliostat passes through a shutter regulating its intensity I_0 . A fraction of the radiation is then intercepted by the rotating blade that modulates the flux I_0 at a frequency of ω_1 . A paraboloidal reflector focuses the radiation onto the target's surface, where it is in part absorbed and reflected (see Fig. 6.1). Both the reflected component ($\rho \cdot I_0$) and the thermal self-emission ($\varepsilon \cdot I_{\text{th}}$) leaving the hot surface within the narrow cone subtended by the DMP optics are collected, chopped at ω_2 and detected. The detector output $D(t)$ is fed in parallel to two lock-in amplifiers (LIA) that are phase-locked to ω_1 and ω_2 , thereby extracting respectively,

$$\begin{aligned} \text{LIA}_1(t) &\propto M_1 \cdot \rho(t)I_0(t) \\ \text{LIA}_2(t) &\propto M_2 \cdot (\varepsilon(t)I_{\text{th}}(t) + \rho(t)I_0(t)) \quad , \end{aligned} \quad (6.1)$$

where M_1 and M_2 are the modulation functions that remain constant for a given instrument configuration. More details about the DMP hardware and its operation principle can be found in [90, 104]. Note, that in the specific setup realized at PROMES-CNRS, M_1 increases as shutter transmittance (τ_{shutter}) is decreased because the rotating blade is positioned parallel to the shutter blades and is not shaded until the shutter closes substantially. Thus, as the shutter initially closes I_0 decreases but the absolute amount of radiation blocked by the rotating blade remains constant. Therefore, the blocked fraction of the solar flux and hence also the amplitude of M_1 increase as the shutter closes. Constant quantities such as the reflectance of the paraboloid, geometry factors related to the collection optics, and the detector gain are contained in the proportionality factor of Eq. 6.1. The thermal signal $S(t)$ is obtained as the difference, if both, $\text{LIA}_1(t)$ and $\text{LIA}_2(t)$, are properly scaled. The scaling factors \hat{g} are obtained from the observation of a cold reference ($I_{\text{th}} \rightarrow 0$) and allows the thermal emission of a hot sample to be determined as

$$S(t) = \text{LIA}_2 - \hat{g} \cdot \text{LIA}_1 \quad . \quad (6.2)$$

$\rho(t)$ can be obtained from $\text{LIA}_1(t)$ (Eq. 6.1) if the incident flux is either constant or can be measured independently. In our case a relative measure of $I_0(t)$ is readily

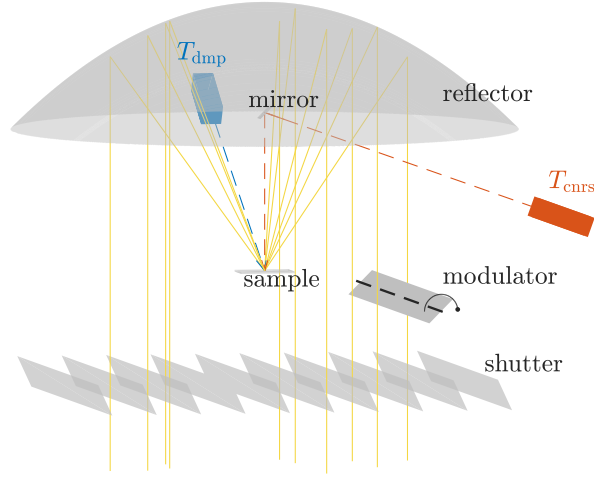


Figure 6.1: Experimental setup: Solar radiation from the heliostat passes a shutter where its total flux I_0 is controlled. A paraboloidal reflector focuses the radiation onto the sample. A rotating blade is mounted below the sample and imprints a modulation of a few per cent at $\omega_1 = 7$ Hz onto the solar flux. DMP observes the sample at an angle while the CNRS pyrometer measures normal to the sample's surface (via a small mirror).

available as the product of the measured DNI and effective transmittance of the shutters τ_{shutter}

$$I_0(t) \propto \text{DNI}(t) \cdot \tau_{\text{shutter}}(t) , \quad (6.3)$$

where $\text{DNI}(t)$ is available from a pyrheliometer, while $\tau_{\text{shutter}} \in [0, 1]$ is obtained the shutter control system. Here, we assume Lambertian and opaque samples where $\varepsilon = 1 - \rho$ is a good approximation of the directional spectral emittance.

The measured signal S combined with the measured ε is converted to a true temperature by the algebraic Sakuma-Hattori equation [85, 88, 89]

$$T = \frac{c_2}{k_2 \cdot \log \left(k_1 \cdot \left(\frac{S}{\varepsilon} \right)^{-1} + 1 \right)} - \frac{k_3}{k_2} = f_{\mathbf{k}}(S, \hat{\varepsilon}) , \quad (6.4)$$

where \mathbf{k} is a three-element vector that holds the calibration coefficients [85]. Their estimation is discussed in Section 6.5.

6.3 Experimental

Setup: The experiments were conducted at the vertical-axis solar furnace facility in Odeillo, France. The experimental setup is shown in Fig. 6.1. A heliostat at the base of the facility deflects radiation onto a 1.5 m diameter parabolic reflector. The system can deliver up to 800 W over an area of about 1 cm² giving rise to a peak concentration of 1500 W/cm² under nominal conditions of 1000 W/m² direct normal irradiance. DNI measurements are provided by a pyrliometer. The flux I_0 to the sample can be regulated a computer-controlled shutter system.

Samples: Disk shaped samples of copper, stainless steel 310S and Al₂TiO₅ (15 × 5 mm², d × h) as well as reticulate porous ZrO₂ and CeO₂ (65 × 25 mm², d × h) were used. Their thermal conductance and reflectance at $\lambda = 5.5 \mu\text{m}$ were determined before. The hemispherical emittance at high temperatures was measured using the MEDIASE setup (Moyen d' Essai et de Diagnostic en Ambiance Spatial Extreme) of the PROMES-CNRS Megawatt Solar Furnace [117].

Double modulation pyrometer: A lens that picks up radiation emanating from the sample is mounted onto the paraboloidal concentrator. The radiation is fed to the detection unit located outside the solar furnace by a fiber optical cable. The rotating blade modulator is located between the sample and the shutter (Fig. 6.1). Details on the detection and analysis components used in the DMP can be found in [90, 104, 116].

Solar blind pyrometer: Installed at the facility is a reference pyrometer (Heitronics KT19 reporting T_{cnrs}) that operates at 5.5 μm and has an effective observation angle of $\theta = 0^\circ$. It observes the sample via a tilted mirror above the focal plane. The radiometer used as pyrometer has been calibrated in this configuration against a black body reference. Values of ε calculated from previously measured reflectance values were used to determine T_{cnrs} .

Still images: A Nikon DSLR camera was used to shoot movies of the experiments that assist in the interpretation of the pyrometric observations (Fig. 6.12).

Modulator design: The flux modulator consists of a rotating blade mounted to a pair of high speed ball bearings fixed in an aluminum structure and driven directly by a 750 W industrial brushless motor. It is located between the shutter and the focal plane of the furnace (Fig. 6.1) where it intercepts the parallel beam from the heliostat. Due to the low stiffness of the blade, the modulation frequency is limited to below 10 Hz. The modulation depth M_1 can be varied in the range 14–4% by changing the position of the blade relative to the optical axis of the furnace. M_1 and thus the calibration coefficient g_1 (Fig. 6.2) is also slightly affected (up to 2%) by τ_{shutter} . Because of the low modulation frequency, temperature measurement on samples with a high thermal conductivity will be difficult as temperatures will fluctuate with a frequency of ω_1 in these cases. Most samples selected (ceramics) exhibit high enough thermal time constant to not be affected.

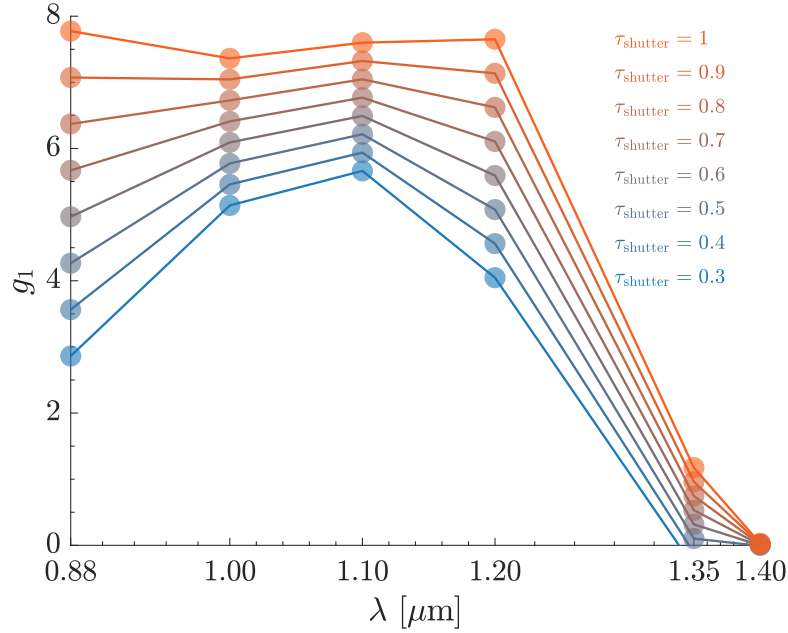


Figure 6.2: Gain calibration coefficient g_1 as function of operation wavelength and shutter transmission (τ_{shutter}).

Operation wavelength: Narrow band transmission filters (typically 10 nm band pass) centered at $\lambda = 0.88, 1.0, 1.1, 1.2 \mu\text{m}$ were mounted on a filter wheel allowing to easily switch between these operation wavelengths while keeping the rest of the optoelectronic pathway identical.

6.4 Gain Calibration

On a cold target, i.e. when the thermal radiation at the operation wavelength band is negligible, the ratio of $\text{LIA}_2(t)/\text{LIA}_1(t)$ represents the relative sensitivity of the two detection channels. Data collected at various values of τ_{shutter} and λ should therefore lie on straight lines as reported in Fig. 6.3. For each pair of τ_{shutter} and λ , data have been collected with different neutral density filters inserted in the optical path to increase the dynamic range of the measurement. Operation of LIA_1 at the low frequencies required by the flux modulator results in a very low signal-to-noise ratio. Thus, the measurements are scattered predominantly along the LIA_1 axis. Since DMP's thermal signal is $S = \text{LIA}_2 - (g_1 \cdot \text{LIA}_1 + g_0)$, the instrument's performance is ultimately limited by the high variance of LIA_1 . To somewhat counteract this adverse effect, $\text{LIA}_1(t)$ is filtered with a rolling window of about 4 s width and zero phase.

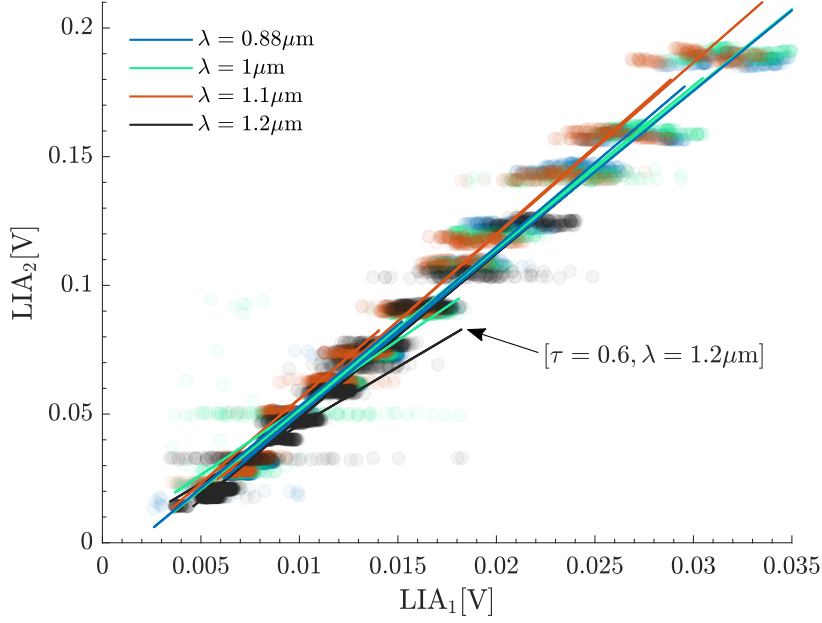


Figure 6.3: $LIA_2(t)$ versus $LIA_1(t)$ fitted straight lines while observing a cold Lambertian reference. Data series recorded for different shutter transmissions (τ_{shutter}) and operation wavelengths of $\lambda = 0.88\mu\text{m}$, $1\mu\text{m}$, $1.1\mu\text{m}$, $1.2\mu\text{m}$ are plotted using different colors.

In Fig. 6.2, the calibration constant g_1 is plotted versus operation wavelength for various values τ_{shutter} . g_1 should ideally be independent of wavelength and τ_{shutter} . This seems to be the case for the shorter four wavebands and for $\tau_{\text{shutter}} \geq 0.8$. Nevertheless, two systematic trends are observed. First, g_1 decreases as the shutter closes, an effect also noticeable in Fig. 6.3. The rotating blade is initially not shaded as the shutter closes. Thus the blocked fraction of the solar flux increases as the shutter closes leading to a higher modulation depth, an increased signal and a decreased g_1 . Second, $g_1 \rightarrow 0$ for $\lambda = 1.35\mu\text{m}$ and $\lambda = 1.4\mu\text{m}$ due to the overlap with the H_2O absorption band that causes $I_0 \rightarrow 0$. For the cold target, both $LIA_1(t)$ and $LIA_2(t)$ approach their respective noise levels at these wavebands. Since LIA_1 operates at a higher gain setting, its noise floor is higher than LIA_2 , causing g_1 to reach 0. Thus no data was collected at $\lambda = 1.35\mu\text{m}$ and $\lambda = 1.4\mu\text{m}$.

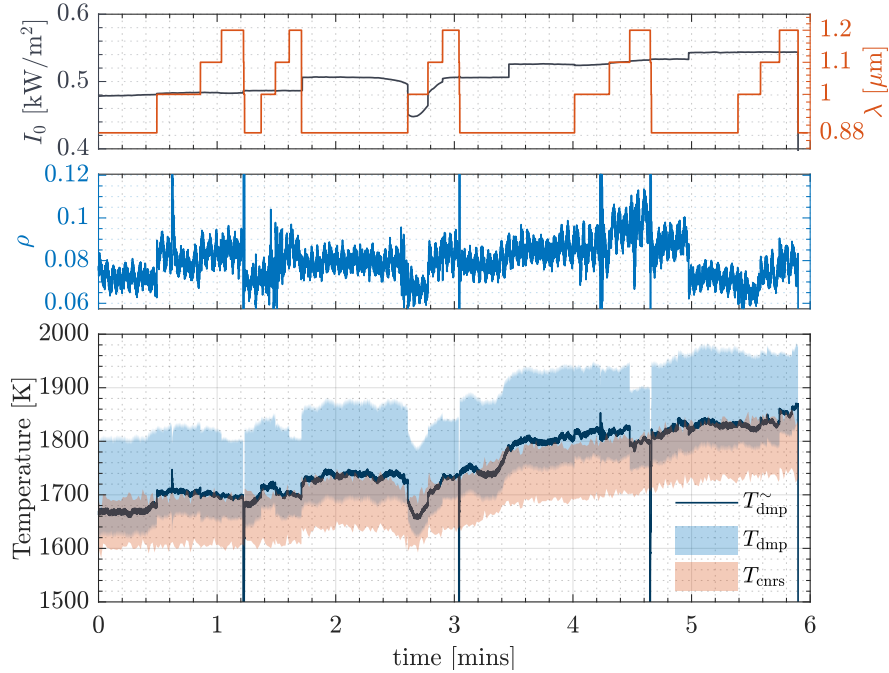


Figure 6.4: Summary of data measured on a stainless steel sample used for temperature calibration. DNI and operation wavelength (top), reflectance measured *in-situ* by DMP (middle) and temperatures (bottom). T_{dmp} and T_{cnrs} are presented as prediction intervals (shaded area), where the lower bound corresponds to the brightness temperature ($\varepsilon = 1$) and the upper bound assumes constant emittance measured *ex-situ* ($\varepsilon(\lambda = 5.5\mu\text{m}) = 0.85$). Note that T_{dmp} traces the reference, i.e. the upper bound of the T_{cnrs} interval.

6.5 Temperature Calibration

Data obtained for the 310S stainless steel sample (see Fig. 6.4) is used to calibrate DMP at the four operation wavelengths versus the reference pyrometer operated at $\lambda = 5.5\mu\text{m}$. For the reference pyrometer a constant emissivity of $\varepsilon = 0.73$ is assumed while for DMP ε is measured *in-situ* and used in the calibration. Measured values of ρ are consistent with those determined before ($\varepsilon(\lambda = 5.5\mu\text{m}) \approx 0.85$). To fit the nonlinear equation,

$$\mathbf{k}_{\text{opt}} = \underset{\mathbf{k}}{\text{argmin}} (f_{\mathbf{k}}(S, 1 - \rho) - T_{\text{cnrs}})^2 \quad (6.5)$$

where $f_{\mathbf{k}}$ is the non-linear Sakuma-Hattori equation (see Eq. 6.4), a Matlab implementation of the trust-region reflective algorithm [92, 93] was used.

The general quality of the fits is reported in Fig. 6.5 that demonstrates that all data lie close to the 45° reference line. The spread of the data represents

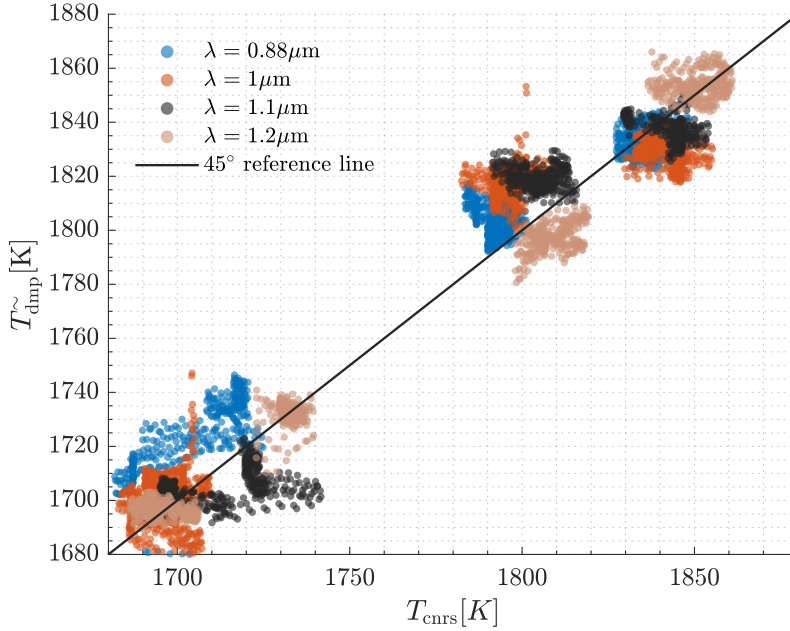


Figure 6.5: Assessment of the temperature calibration for the four operation wavelengths ($\lambda = 0.88, 1.0, 1.1, 1.2 \mu\text{m}$).

the temperature bias which amounts to about ± 15 K. The largest error source is attributed to the low S/N ratio of $\text{LIA}_1(t)$ caused by the very low modulation frequency close to the lower limit at which the instrument can be operated. For a discussion of the error introduced by operating the reference pyrometer at a different wavelength than DMP see [104]. T_{dmp}^{\sim} , the temperature using the on-line measured emittance, reported in Fig. 6.4 is slightly higher than the reference temperature T_{cnrs} because of the lower values of ρ measured *in-situ* by the DMP.

6.6 Results and Discussion

In the following we present a direct comparison of T_{dmp} with T_{cnrs} data for three samples (Copper, Al_2TiO_5 and Steel 310S) where the optical and thermal properties have been characterized before. In addition, measurements are reported for two reticulate porous ceramic samples (ZrO_2 and CeO_2 [116]), which are frequently used as thermal insulation for solar receivers or as active materials in thermochemical cycles. DMP data are presented for four different operation wavelength bands ($\lambda = 0.88, 1.0, 1.1, 1.2 \mu\text{m}$) which are easily accessible with our current detector.

In all the following figures, the results reported for each instrument are the brightness and emissivity-corrected temperatures that are visually grouped as the

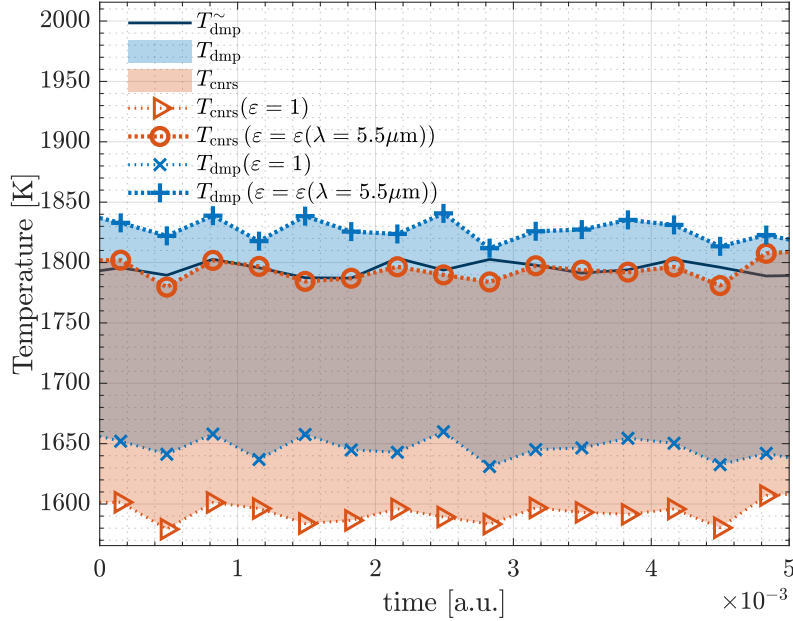


Figure 6.6: The two shaded areas serve to visually group the brightness (bottom) and emissivity-corrected (top) temperature observations belonging to the two instruments (DMP) and (CNRS). For both instruments, the lower bound is formed by the brightness temperature ($\varepsilon = 1$) and the upper bound is formed by the constant emittance that had been measured at an observation angle and wavelength that match those of the CNRS pyrometer.

lower and upper bounds of a shaded area. Specifically, the lower bound is formed by the brightness temperature ($\varepsilon = 1$) and the upper bound is formed by using the constant emittance that had been measured at a normal observation angle and at a wavelength of $5.5\mu\text{m}$. Note that this constant emittance that is used to correct the brightness temperature of both instruments, only matches the CNRS pyrometer's observation angle and wavelength. The bounds of the shaded areas are explicitly shown and explained in the legend of Fig. 6.6, but are omitted in the following results figures to avoid clutter. In addition, T_{dmp}^{\sim} — which includes the emissivity values measured on-line by DMP (see Table 6.1) — is plotted as a separate line. Reflectance of the sample, reported in the middle panel in all figures, were determined on-line from the signal of LIA_1 (see Eq. 6.1 and using Eq. 6.3 for $I_0(t)$). Emittance was calculated from the in-situ measured reflectance as $\varepsilon = 1 - \rho$ i.e. assuming opaque and Lambertian samples.

Symbol	Instrument	Type	Description (Eq. 6.4)	ρ
T_{dmp}^{\sim}	DMP	line	$f_{\mathbf{k}}(S, \varepsilon = 1 - \rho)$	<i>in-situ</i>
T_{dmp}	DMP	interval	$[f_{\mathbf{k}}(S, \varepsilon = 1), f_{\mathbf{k}}(S, \varepsilon(\lambda = 5.5\mu\text{m}))]$	<i>ex-situ</i>
T_{cnrs}	solar-blind	interval	$[f_{\mathbf{k}}(S, \varepsilon = 1), f_{\mathbf{k}}(S, \varepsilon(\lambda = 5.5\mu\text{m}))]$	<i>ex-situ</i>

Table 6.1: Symbols of measured temperatures

6.6.1 Copper

Cu_2O and CuO are the two thermodynamically stable phases of the copper oxygen system [118] at 700–900°C. X-ray diffraction studies [119] of high-temperature Copper oxidation have identified the presence of CuO and Cu_2O as two distinct layers. Cu_2O forms next to the Cu substrate, while the CuO phase forms the outer layer, due to the higher oxygen partial pressure [120]. The melting points of Cu, Cu_2O and CuO are 1358 K, 1505 K and 1599 K, respectively.

Two different Copper samples, $\text{Cu}^{(A)}$ and $\text{Cu}^{(B)}$ were subjected to concentrated solar radiation while temperatures were measured. An embedded thermocouple in sample $\text{Cu}^{(A)}$ provided the additional T_{tc} . Both samples had been preoxidized forming a CuO layer on their surface and were optically homogeneous.

In Fig. 6.7 the temperatures measured with the different instruments are reported for the $\text{Cu}^{(A)}$ sample. Initially, temperatures are too low to be measured by a pyrometer. Only T_{tc} is valid. Once temperatures reach about 800 K at $t = 3$ min, T_{cnrs} becomes valid and reports similar temperatures as T_{tc} . DMP exhibits a higher minimum temperature that can be detected and becomes valid only after about 10 min. At about 7 min, T_{cnrs} coincides with T_{tc} revealing that there is negligible temperature difference between the exposed surface and the inside of the sample. This suggests the existence of a thin surface oxide layer and that the bulk of the sample is still predominantly Cu. As the oxidation proceeds thermal conductance decreases and the difference temperature difference increases between T_{cnrs} and T_{tc} during the interval 10–24 min.

At about 21 min, I_0 increases significantly and a steep decrease of $\rho(t)$ is observed. A further increase of I_0 at about 24 min leads to partial melting of the sample that coincides with a further decrease in ρ . While T_{cnrs} is now in excellent agreement with T_{tc} , DMP does not seem to provide data anymore most probably because it now observes a strongly curved specular surface at a high observation angle. As the experiment continues, the molten region slowly extends radially, until at about 35 min a hole forms in the melt. This is probably facilitated by the hole in the center of the sample that provides access to the thermocouple.

A similar experiment for the $\text{Cu}^{(B)}$ sample is reported in Fig. 6.8: The shutters open within ≈ 1 s to $\tau_{\text{shutter}} = 0.4$ and the sample is rapidly heated while DMP observes at $0.88 \mu\text{m}$. Once a steady-state temperature has been reached, the

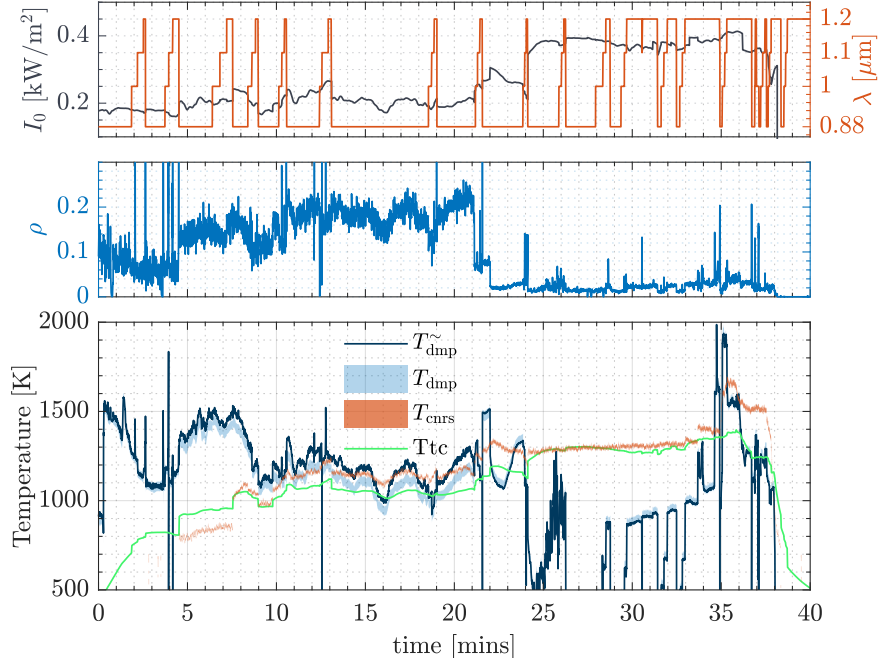


Figure 6.7: Summary of data measured on copper (sample A). DNI and operation wavelength (top), reflectance measured *in-situ* by DMP (middle) and temperatures (bottom). T_{dmp} and T_{cnrs} are presented as prediction intervals (shaded area), where the lower bound corresponds to the brightness temperature ($\varepsilon = 1$) and the upper bound assumes constant emittance measured *ex-situ* ($\varepsilon(\lambda = 5.5\mu\text{m}) = 0.9$).

sample is rapidly cooled. The cycle is repeated at $\lambda = 1.0, 1.1, 1.2 \mu\text{m}$.

Independent of operating wavelength a steady state temperature of about 1500 K is detected by T_{dmp} . At all wavelength ρ decreases as the temperature increases consistent with previous observations [121, 122]. The distinct bump observed in $\rho(t)$ is attributed to small distortion of the sample's surface caused either by thermal expansion or continued surface oxidation. T_{cnrs} is not affected as it observes the sample perpendicular to its surface and applies a constant value for the emittance. T_{dmp} , however, exhibits the same bump as it uses the measured reflectance.

The values for ρ determined *in-situ* for both $\text{Cu}^{(A)}$ and $\text{Cu}^{(B)}$ are in good agreement with [121], where the value for the normal total emittance of stably oxidized copper at 1033 K approaches 0.9. The values are also consistent with the high solar absorptivity that copper oxide surfaces exhibit [123].

It has also been reported [120] that ε decreases and thus ρ increases with increasing polar angle. This is consistent with our observation that the *in-situ* determined emittance at high polar angles is smaller than the normal emittance

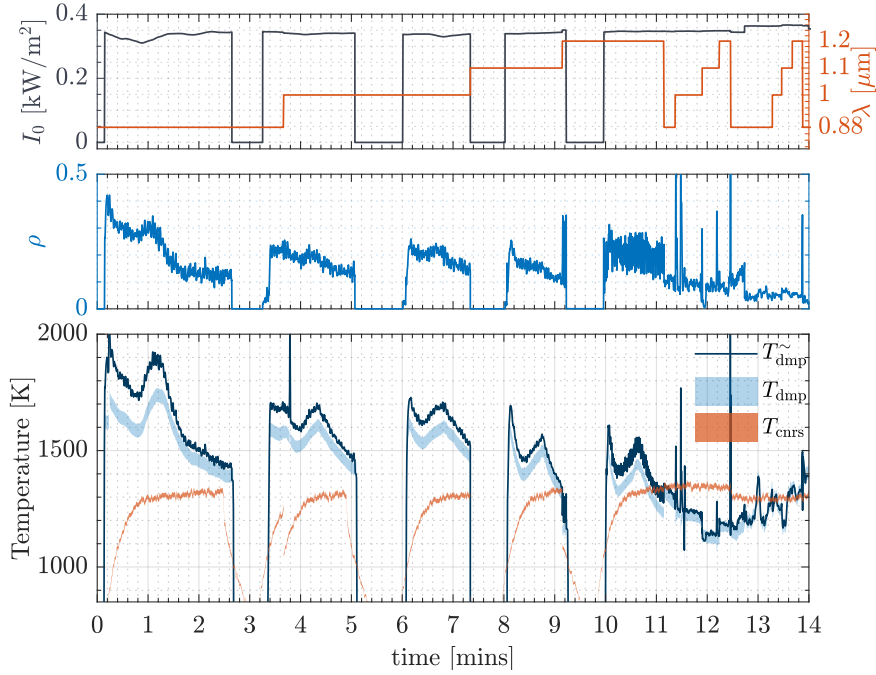


Figure 6.8: Summary of data measured on copper (sample B). DNI and operation wavelength (top), reflectance measured *in-situ* by DMP (middle) and temperatures (bottom). T_{dmp} and T_{cnrs} are presented as prediction intervals (shaded area), where the lower bound corresponds to the brightness temperature ($\varepsilon = 1$) and the upper bound assumes constant emittance measured *ex-situ* ($\varepsilon(\lambda = 5.5\mu\text{m}) = 0.9$)

determined before. As a consequence, T_{dmp}^{\sim} that relies on the *in-situ* measurement systematically overshoots the upper bound of the T_{dmp} interval in both copper samples (see Figs. 6.7 and 6.8).

The two copper experiments highlight significant limitations of the DMP implementation. During the first 9 mins of the $\text{Cu}^{(A)}$ experiment (Fig. 6.7)— while temperature is below the DMP detection limit — the invalid T_{dmp} values overshoot the thermocouple and T_{cnrs} measurements as well as the subsequent valid T_{dmp} measurements. Furthermore, during the repeated heating-cooling cycles of the $\text{Cu}^{(B)}$ experiment (Fig. 6.8), T_{dmp} exhibits a consistent downward trend on which an upward bump is superimposed – this is at odds with the upward temperature curve obtained by the reference pyrometer (T_{cnrs}). Across the five heat-up experiments, the bump appears always at a constant T_{cnrs} value which may hint at temperature induced sample movement. Nevertheless, the likelihood of the bump being caused by a sample-related movement is small due to the fact that such an event should have also been observed in the T_{cnrs} signal. In addition, significant correlation between DMP’s thermal (T_{dmp}) and reflected (ρ) signals can be ob-

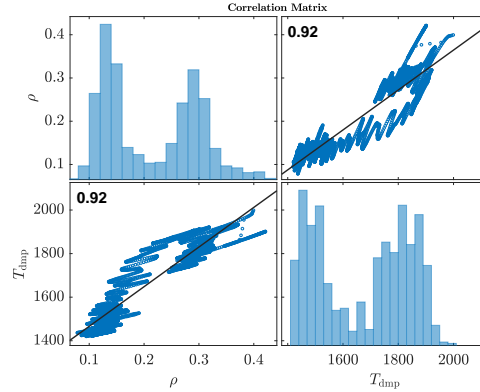


Figure 6.9: The T_{dmp} and ρ values collected during the first 3 mins of the Cu^B experiment (see Fig. 6.8) are highly correlated ($\rho = 0.92$). Also, the distribution of ρ observations (top-left panel) is similar to the distribution of T_{dmp} observations (bottom-right panel).

served throughout the heat-up curves of Fig. 6.8. In particular, a closer look into the first ≈ 3 mins of the Cu^B experiment reveals that the two DMP signals — ρ and T_{dmp} — exhibit a very high correlation ($\rho = 0.92$) and strong similarities in their distributions (Fig. 6.9). It is plausible that due to the high thermal diffusivity of copper and the low mechanical modulation frequency of the rotating blade both thermal and reflected components are modulated at ω_1 . In this case, LIA1 would track the composite signal — just like LIA2 does. Under this scenario, the calibration would not be valid and it would be hard to defend the validity of the DMP observations.

6.6.2 Stainless Steel 310S

Austenitic stainless steel 310, containing 25% Cr, 20% Ni, 0.6% Si, is corrosion resistant at high temperatures and deformation resistant due to the added carbon [124]. Thanks to these properties it is of interest for use in high temperature applications in excess of 1400 K under oxidizing atmospheres.

A similar experiment as for sample $\text{Cu}^{(B)}$ has been performed on the steel sample and is reported in (Fig. 6.10). The sample is rapidly heated, kept at high temperature until steady state conditions are reached and then left to cool. Temperature and reflectance are measured by the various pyrometers as the procedure is repeated for $\lambda = 0.88, 1.0, 1.1, 1.2 \mu\text{m}$.

Surface temperatures typically reach $\approx 90\%$ of their peak values within a second and then continue to increase slowly until they reach their final values. During the whole experiment, T_{dmp} parallels T_{cnrs} and the two prediction intervals over-

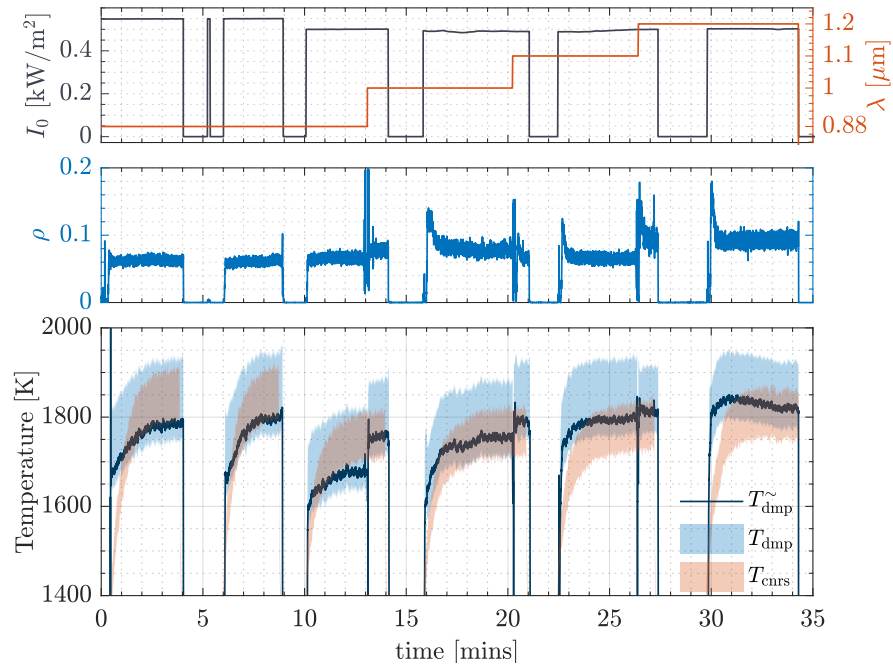


Figure 6.10: Summary of data measured on a stainless steel sample. DNI and operation wavelength (top), reflectance measured *in-situ* by DMP (middle) and temperatures (bottom). T_{dmp} and T_{cnrs} are presented as prediction intervals (shaded area), where the lower bound corresponds to the brightness temperature ($\varepsilon = 1$) and the upper bound assumes constant emittance measured *ex-situ* ($\varepsilon(\lambda = 5.5\mu\text{m}) = 0.85$)

lap significantly. The best agreement between the two pyrometers is attained for $\lambda = 1.1\mu\text{m}$, where T_{dmp}^{\sim} tracks the upper bound of T_{cnrs} . This is because — as shown in Fig. 6.6 — the upper bound of T_{cnrs} is the best estimate provided by the CNRS solar-blind pyrometer, since it makes use of the emissivity measurement that matches the operating wavelength and angle of observation of the CNRS pyrometer. Similarly, T_{dmp}^{\sim} is DMP’s best estimate since it makes use of an in-situ measured emissivity that matches DMP’s operating wavelength and angle of observation. The surface endures the high temperatures in excess of 1500 K without any significant changes, as is evident by visual inspection after the experiment.

Given that the emittance of solid stainless steel 310S is sensitive to sample preparation and exact surface state, literature values are scattered. Nevertheless, magnitude, as well as wavelength and temperature dependence of ρ measured in Fig. 6.10 are consistent with previous studies. Specifically, the *in-situ* ρ measurements agree well with the reflectance values determined before at CNRS and the previously reported emissivity values of about 0.95 [124] and 0.9–0.97 [125]. The wavelength dependence of ρ is in agreement with [124] (see Fig. 5 in [124]), in that ρ increases with wavelength ($\rho \approx 0.06, 0.08, 0.08, 0.1$ for $\lambda = 0.88, 1.0, 1.1, 1.2 \mu\text{m}$).

In addition, we infer that ρ decreases with increasing temperature: The transient surge in ρ that appears at the beginning of each of the three heat-up curves at $t = 16, 23, 30$ min is an artifact caused by the fast increase of I_0 that masks the temperature dependent decrease of ρ [124, 126].

6.6.3 Al_2TiO_5

Al_2TiO_5 exhibits excellent thermal shock resistance due to its low thermal expansion coefficient, low thermal conductivity (1.5 W/mK) and high melting point that lies between 2073 and 2133 K [127].

In Fig. 6.11 we report data measured on Al_2TiO_5 as it is heated up to its melting point and above. Melting occurs around 1 min where the sample becomes highly specular evidenced by an abrupt decrease of ρ from approximately 0.5 to about 0.1. The molten film is maintained for the duration of the experiment resulting in a relatively stable value of $\rho \approx 0.1$. Stochastic variations of the texture of the molten surface affect the apparent reflectance and are recorded by DMP. They are also evident in the still frames reported in Fig. 6.12. Most notably, the shallow dip of ρ observed around 8 min that lasts for approximately 1 min is noticeable as a sequence of darker still frames.

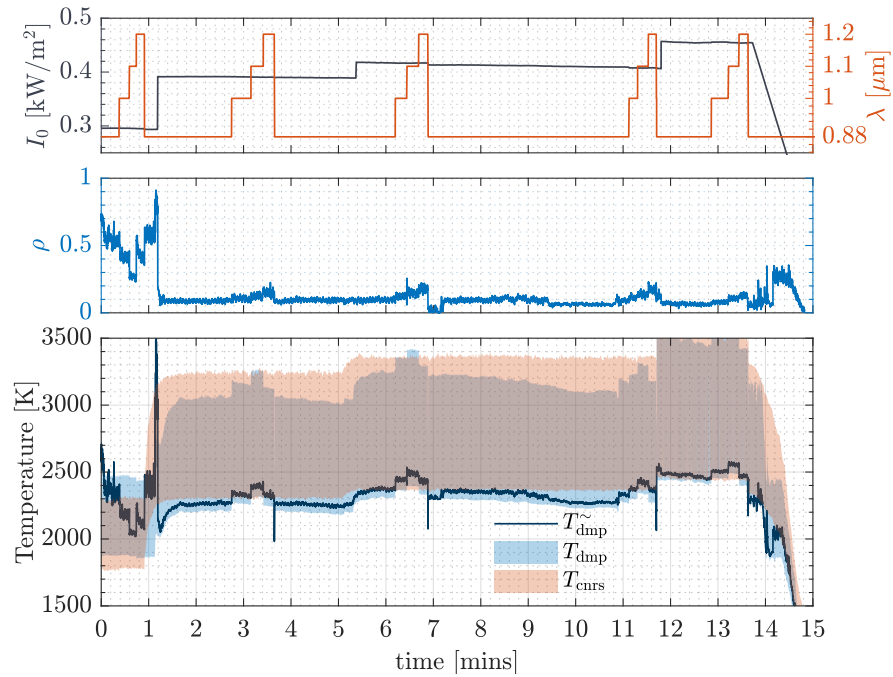


Figure 6.11: Summary of data measured on Al_2TiO_5 . DNI and operation wavelength (top), reflectance measured *in-situ* by DMP (middle) and temperatures (bottom). T_{dmp} and T_{cnrs} are presented as prediction intervals (shaded area), where the lower bound corresponds to the brightness temperature ($\varepsilon = 1$) and the upper bound assumes constant emittance measured *ex-situ* ($\varepsilon(\lambda = 5.5\mu\text{m}) = 0.3$)

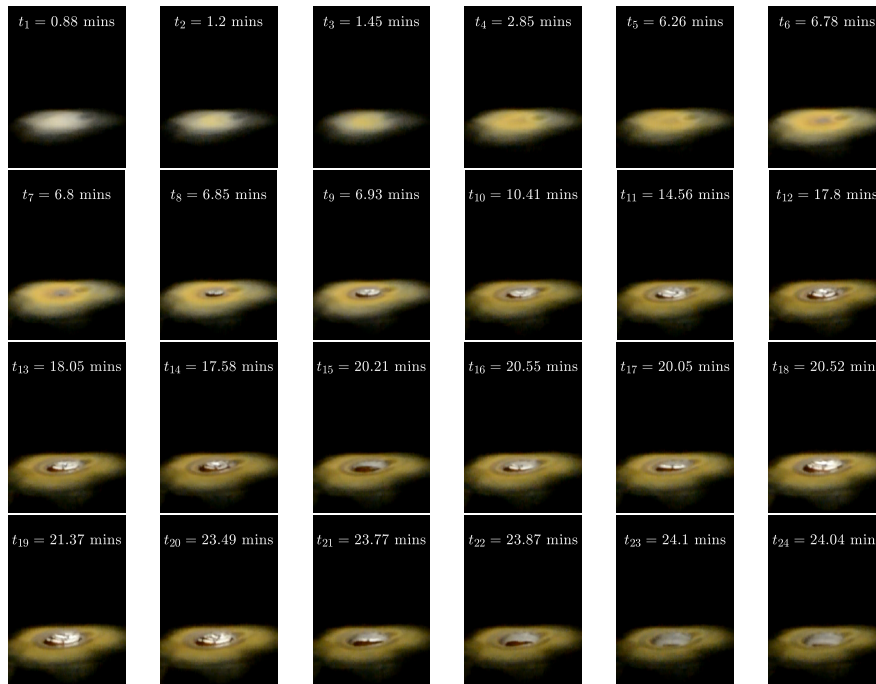


Figure 6.12: Still images of the Al_2TiO_5 sample being exposed to concentrated radiance over the course of the experiment. At t_2 melting occurs at the center of the heating zone.

Good agreement is observed between the T_{dmp} and T_{cnrs} prediction intervals. The respective brightness temperatures (lower bounds, $\varepsilon = 1$) agree within 100 K. After melting, T_{dmp}^{\sim} traces the lower bound of the prediction interval, consistent with the low ρ values that were measured *in-situ*. The upper bounds of both T_{dmp} and T_{cnrs} are unreasonably high because $\varepsilon = 0.3$ obtained from measurements on the solid sample at 1400 K is not applicable for the melt. In fact, both ρ and T_{dmp}^{\sim} indicate that the true temperature must lie close to the lower bound and that emittance must be closer to ≈ 0.9 .

Towards the end of the experiment I_0 is decreased and the sample cools. As the sample solidifies, ρ increases to 0.3 again consistent with the values determined before the experiment.

6.6.4 ZrO₂ reticulate porous ceramic

The same reticulate porous zirconia that was already studied in [116] was also examined in this study. Only T_{dmp} could be measured on these samples and are reported in Fig. 6.13. The CNRS reference pyrometer could not cope with the porous sample.

In the first part of the experiment up to about $t = 7$ min, the ZrO₂ sample is slowly heated from about 2200 K by increasing I_0 in discrete steps. At each step data are collected at $\lambda = 0.88, 1.0, 1.1, 1.2 \mu\text{m}$.

T_{dmp}^{\sim} increases and approaches ZrO₂'s melting point of 2988 K as the flux reaches its maximum value. These temperatures seem trustworthy as we found evidence of melting on a small area at the center of the sample after the experiment. T_{dmp}^{\sim} measurements at $\lambda = 0.88, 1.0, 1.1 \mu\text{m}$ generally agree within 100 K throughout the experiment while temperatures measured at $1.2 \mu\text{m}$ are consistently lower.

The reflectance steadily decreases from about $\rho = 0.2$ at the beginning of the experiment to about 0.05 after 7 min. This causes T_{dmp}^{\sim} to gradually approach the lower bound of the prediction interval, i.e. the brightness temperature. The same temperature dependence of ρ has been observed before on an identical sample that was studied in a solar simulator [116]. A wavelength dependence of ρ is also observed: At temperatures below 2700 K, ρ increases with increasing wavelength while at higher temperatures the trend is reversed.

At about 7 min, shutters are closed and the sample is left to cool over a period of 30 s. Then the sample is again exposed to the maximum flux of before and temperatures are again determined for the four operation wavelengths. This time, the data collection time at each wavelength is increased to about 30 s to better ensure steady state conditions. Note that the dip in T_{dmp} at around $t = 8$ min is caused by a 25% decrease in DNI. Very similar temperatures and reflectances are observed in the second series as compared to the first, confirming the repro-

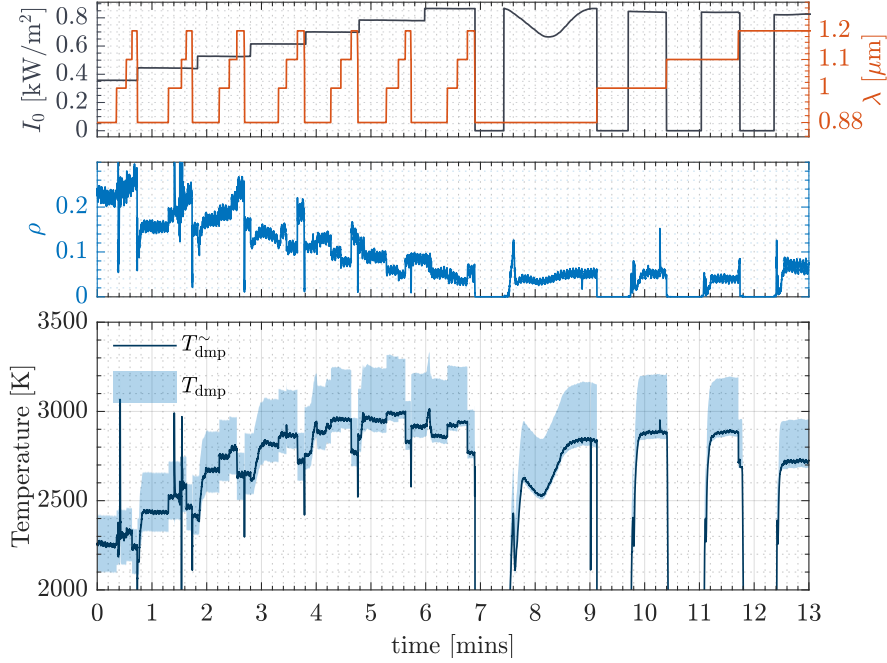


Figure 6.13: Summary of data measured on reticulate porous ZrO_2 . DNI and operation wavelength (top), reflectance measured *in-situ* by DMP (middle) and temperatures (bottom). T_{dmp} is presented as prediction intervals (shaded area), where the lower bound corresponds to the brightness temperature ($\varepsilon = 1$) and the upper bound assumes constant emittance measured *ex-situ* ($\varepsilon = 0.6$).

ducibility of both T_{dmp} and ρ observations. Temperatures determined at $1.2 \mu\text{m}$ are consistently lower by about 200 K. We consider this to be an artifact most probably originating from a glitch in the gain calibration at this wavelength.

6.6.5 CeO_2 reticulate porous ceramic

The same testing procedure as for the ZrO_2 sample was applied to the ceria sample (Fig. 6.14). In the first part of the experiment until about $t = 7$ min, the sample is subjected to a step-wise increase of I_0 . T_{dmp} increases and approaches the melting point of CeO_2 at 2673 K in the measurement interval at around 6.5 min. At each value of I_0 data is collected at $\lambda = 0.88, 1.0, 1.1, 1.2 \mu\text{m}$. At around 7 min, shutters are brought to a closing position and the sample is left to cool over a period of 30 s. Then, the shutter opens within 1 s exposing the sample to the maximum flux applied in the series before. The sample is rapidly heated while DMP observes at $\lambda = 0.88 \mu\text{m}$. Once the steady-state temperature has been reached, the shutter closes and the sample is rapidly cooled again. This sequence

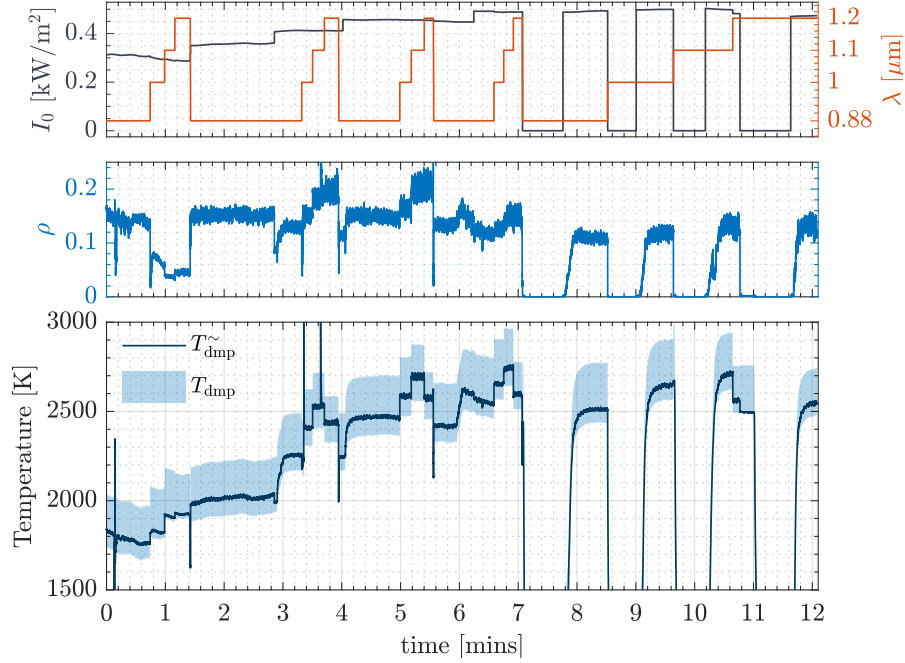


Figure 6.14: Summary of data measured on reticulate porous CeO_2 . DNI and operation wavelength (top), reflectance measured *in-situ* by DMP (middle) and temperatures (bottom). T_{dmp} is presented as prediction intervals (shaded area), where the lower bound corresponds to the brightness temperature ($\varepsilon = 1$) and the upper bound assumes constant emittance measured *ex-situ* ($\varepsilon = 0.73$).

is repeated for the wavelength bands at $\lambda = 1.0, 1.1, 1.2 \mu\text{m}$. Significantly lower temperatures are obtained this time compared to the first series. However, peak temperatures clearly increase with each heating cycles except for the last one. We thus assume, that the cooling time of 30 s was insufficient and that the sample become hotter with each exposure to the concentrated solar radiation. Note, that I_0 is decreased by about 5% at $t = 10.5$ min accompanied by a temperature drop. This temperature is later observed again towards the end of the measurement at $\lambda = 1.2 \mu\text{m}$ as now steady state conditions are finally reached.

A small decrease in ρ is observed with increasing temperature as well as a clear increases of reflectance. This trend is consistent with recent measurements of the spectral hemispherical reflectance of reticulate porous CeO_2 [128].

6.7 Conclusion

We demonstrated temperature and *in-situ* reflectance measurements under natural concentrated sunlight using double modulation pyrometry. The performance of

DMP was assessed at four wavelengths ($\lambda = 0.88, 1.0, 1.1, 1.2 \mu\text{m}$) and compared to a reference solar blind pyrometer operating at $5.5 \mu\text{m}$ using reflectance values of the samples determined before at room temperature.

For all samples the agreement between T_{dmp}^{\sim} and T_{cnrs} generally lies within of about 100 K. Using the *in-situ* ρ data improves the the accuracy of the prediction. In the case of ZrO_2 RPC, T_{dmp}^{\sim} data are consistent with the observed melting of the sample.

Applying DMP in a solar furnace exposed several problems, none of which are connected to the method in general but rather to the specifics of a solar furnace or the experimental setup available at CNRS.

Generally, the assumption of homogeneous solar radiation after the heliostat is not well fulfilled. Due to the waviness of the heliostat surface an inhomogeneous flux distribution results that varies as function of reflection angle and thus varies during the day. As a consequence, also M_1 varies during the day making the gain calibration unreliable therefore hampering the separation of reflected radiation from the thermal radiation.

Due to mechanical limitations of the rotating blade modulator at CNRS, ω_1 was below 10 Hz very close to the lowest operation frequency of the LIA. This led to intermittent signal losses cause by the failure of the phase locking loop to reliably lock onto the reference signal. Also, the rotating blade modulator at CNRS is mounted parallel to the shutter blades. Therefore, M_1 , and thus also g_1 depend on the shutter transmission an effect that could largely be avoided if the modulator was mounted perpendiculat to the shutter blades.

We found that an additional bias introduced in the measurement of the reflectance comes from uncertainties of the DNI measured. As the pyrhelimeter is located away from the heliostat at CNRS, an bias is introduced, especially if DNI varies to the presence of clouds.

Nevertheless we consider DMP to be a useful tool also for application in a solar furnce. Most of the difficulties encountered could be solved with a setup optimized for use with DMP.

Chapter 7

Conclusions and Outlook

A novel radiometric method to measure the true surface temperature of radiatively heated opaque samples was realized and experimentally demonstrated in two solar simulator facilities and a solar furnace. The method modulates the intensity of both the irradiance (I_0) and radiosity ($I_\varepsilon + \rho \cdot I_0$) emanating from the surface at two different frequencies ω_1 and ω_2 and uses phase sensitive detection to measure independently the two components. The thermal signal (I_ε) — bearing the temperature information — can then be extracted as the difference of the two measurements.

The main requirement of the method is the modulation of I_0 , which is conceptually simple but challenging to implement. Electronic modulation of I_0 by superimposing a voltage signal on the DC voltage supply of the Xenon-arc lamp is an elegant approach that was investigated in a single-source simulator but failed to satisfy design objectives. Because the lamp's axis coincides with the optical axis, an image of both of the lamp's main radiation components — *arc* and *anode* — is formed on the focal plane. The arc's radiance — maintained by the electron flux emitted from the cathode — responds instantaneously to the modulated current. The same is not true for the anode's thermal radiance whose thermal time constant is larger than the modulation period of $\tau \approx 0.01$ s. Even though the arc has a significantly higher brilliance, the anode contributes about 40% to the total lamp output due to its large surface area. Under these conditions, a significant fraction of irradiance (I_0) remains unmodulated. As the temperature of the anode varies stochastically during lamp operation, its contribution to the total flux cannot be accounted for by calibration.

In light of the failure of the electronic route, the most robust approach to attain modulation of the total flux irradiating the surface proved to be intercepting the flux by use of a mechanical component. In this thesis, the flux modulator in two representative CSP facilities was designed and implemented. For each case, the optical characteristics of the CSP facility had to be taken into account. First, the

typical design of an optical chopper-wheel could not be applied in the single-source imaging furnace, due to the confined space and the hemispherical irradiation of the sample. To design an instrument that modulates the radiation intensity originating from both the arc and the glowing anode of the xenon-arc lamp, the cylindrical symmetry of the lamp-reflector module was leveraged, whereby only an angular sector of the total lamp output was intercepted by a rotating blade. The blade featured a rhomboidal cross section with an aspect ratio of 1/3, a rotation axis parallel to the optical axis and a modulation depth of about 5%. Second, in the multi-source high-flux solar simulator, intercepting the total cross section of the converging beam by an optical chopper was realized, leading to a modulation depth of about 30% and a minimum detectable temperature of about 1000 K. To avoid excessive size, the optical chopper had to be placed relatively close to the sample, leading to the modulator structure partially conflicting with the experimental setup of the cavity reactor and enforcing relatively oblique observation angles. Third, in the CNRS solar furnace facility, the homogeneity of the parallel solar rays deflected by the heliostat was leveraged in the design process, so that a fraction of the parallel rays were intercepted by the rotating blade — designed and built at CNRS.

Instrumental to the proof of concept experiments was a simple experimental setup consisting of a thin platinum strip placed in focus, with its irradiated side being observed by DMP and its back side by a calibrated pyrometer. The platinum strip satisfied the requirements of an isothermal object whose emissivity exhibits weak temperature and wavelength dependence. Hence, it could be assumed with confidence that the two instruments register the same temperature. The setup was versatile in that it enabled both calibration by comparing measurements of DMP (T_{dmp}) against measurements of the reference pyrometer (T_{ref}) over an extended temperature range, and validation by enabling observation of the melting point of platinum. The melting event was identified by the observed abrupt change in reflectance signal ($\rho \cdot I_0$). By associating the brightness temperature observed at the point of melting with the Platinum melting point, $\epsilon_{\text{eff}}(T = 2041 \text{ K}, \lambda = 1.2 \mu\text{m})$ was determined and was used to convert brightness temperature to true surface temperature.

The calibration using the platinum sample offered the advantage of easy replication in-place, but has limitations in terms of accuracy and precision: It is prone to a potential systematic temperature error (ΔT_{sys}), which is a function of the difference in operating wavebands of the two pyrometers ($\Delta\lambda$) and of our uncertainty about the emissivity of platinum ($\Delta\epsilon$). From empirical distributions of the two measurement inputs ($\text{LIA}_1, \text{LIA}_2$), we simulated using the Monte-Carlo method the propagation of uncertainty across the calibration and measurement chain obtaining simulated distribution of each of the five calibration coefficients (g_1, g_0, k_1, k_2, k_3) and temperature. The k_1, k_2, k_3 distributions were characterized

by relatively high dispersion which itself translates to an imprecise temperature estimate. A sensitivity analysis of the output variable (T) with respect to each coefficient showed that (k_2) may contribute 50% of the temperature error.

In principle, the temperature calibration coefficients (k_1, k_2, k_3) depend solely on the modulation function ($m_2(t)$) of the radiosity signal and are decoupled from the modulation function ($m_1(t)$) of irradiance. Changes in $m_1(t)$ are absorbed by the gain calibration coefficients (g_1, g_0) during the gain-calibration step. Given that the chopper implementing $m_2(t)$ is fixed inside the portable electronics case, decoupling has practical implications: As long as proper care is taken to keep the optical configuration within the box unchanged, the laborious temperature calibration step does not have to be repeated even if $m_1(t)$ is varied, say, by transporting the instrument from one facility to another.

A significant source of uncertainty tied to the implementation of the method at the imaging furnace was the the small size of the simulator's hot zone that was comparable to the measurement spot ($\varnothing \approx 3$ mm). It is a limiting factor of measurement accuracy due to temperature non-uniformity. Since the hot spot is characterized by steep temperature gradients, the measured radiance is a weighted sum of the intensity levels within the non-isothermal area. The temperature measured by DMP on the front surface of the low emissivity sample was within 20 K to the back-side temperature measured by the reference pyrometer. In addition, it was difficult to maintain an overlap of the two spots: small changes in sample thickness or holder position would result in misalignment between the measurement spot and the hot spot. We decreased the collecting aperture by about 50% to reduce the observation spot, but this had a detrimental effect on the minimum detectable temperature that was already approaching the melting point of Platinum — although the use of a more sensitive detector could have compensated for the reduced signal level. The hot spot size of about 3 mm is a limitation specific to the facility, rather than a limitation of the method, since in most solar simulators the size of the hot spot is larger by an order of magnitude (about 5 cm). The combination of the low emissivity metallic sample and the small size of the hot zone led to a minimum detectable temperature of about 1700 K for the series of experiments conducted in the imaging furnace. In contrast, the chopper wheel prototype implemented in the multi-source solar simulator exhibited superior performance — in terms of minimum detectable signal — of about 1000 K, benefiting from the combination of increased modulation depth and a large hot spot.

The functionality to measure ε is built into the instrument and does not require additional equipment or calibration steps. This is a departure from other methods, where emissivity correction had to be implemented in relatively complex set-ups requiring an external light source or concurrent measurements at multiple wavebands. First, I_0 is the broadband, intense light irradiating the surface under an

approximately hemispherical solid angle. Second, the reflected component tracked by $LIA_1(t)$ contains a good approximation of the hemispherical-directional reflectivity ($\rho \approx \rho_{\Gamma,\theta}$). Third, $LIA_1(t)$ is calibrated against the known reflectance of the cold reference target during the gain calibration step. Hence, the only prerequisite to extract ρ is to be able to obtain a relative measure of I_0 compared to its value during calibration. In the solar simulator experiment (Ch. 5), I_0 was maintained constant relative to the calibration value. In the solar furnace experiments (Ch. 6), measurements of the direct normal irradiance ($DNI(t)$) were used as a proxy for I_0 , since $I_0 \propto DNI$ (Eq. 3.19). Subsequently, the directional emissivity was calculated via Kirchhoff's law ($\varepsilon = 1 - \rho$).

The radiosity $I_\varepsilon + \rho I_0$, thermal radiance I_ε and corrected thermal radiance $I_\varepsilon/(1 - \rho)$ can all be measured by DMP, yielding respectively three temperature measurements $T_{\text{pyro}}(t)$, $T_{\text{dmp}}^-(t)$, $T_{\text{dmp}}^\sim(t)$ (Eq. 5.4). From the difference between these measurements, time series of the temperature error caused by reflectance ($\Delta T_\rho(t)$) and emissivity ($\Delta T_\varepsilon(t)$) were extracted, showing their relative contribution over time. We found that the errors varied significantly as a function of the reflectance and temperature of the surface. It was also observed that $\Delta T_\rho(t)$ and $\Delta T_\varepsilon(t)$ have an opposite sign so that their effects on the true temperature partially cancel out.

These enhancements allowed the temperature determination of surfaces undergoing dynamic emissivity changes under adverse conditions of direct irradiance in two experimental setups, a multi-source solar simulator at PSI and a solar furnace at CNRS. In the solar simulator, measurements were conducted on three representative ceramic materials (Al_2O_3 , SiSiC and ZrO_2) undergoing fast heat-up accompanied by dynamic changes in emissivity. The method was also applied to measure the temperature of a cavity-type cylindrical solar receiver whose walls are made of CeO_2 in the form of reticulated porous ceramic (RPC) foam and whose irradiated aperture is sealed with a quartz window. Radiation enters the cavity through the quartz window at the front, diverges and irradiates the back wall of the reactor. Measurements were collected from four thermocouples, the reference pyrometer and DMP during two consecutive heating cycles. It was observed that the two pyrometers tended to overestimate surface temperature due to the cavity reflection error, while thermocouples underestimated it due to their offset (about 4 cm) from the point of measurement. Specifically, the two pyrometers observing the reactor's colder wall measured consistently about 100 K higher than the thermocouple placed close to the directly irradiated, hotter back wall. We also concluded that the advantages of measuring with DMP versus with a solar blind pyrometer are limited — especially in the cavity wall region that was not directly irradiated. Because the reflected signal was negligible, DMP's ability to filter out $\rho_s \cdot I_0$ did not offer any significant advantage versus the reference pyrometer in

this application. On the other hand, the effect of the cavity tends to dampen the severity of the emissivity error (ΔT_ε) and of the parasitic reflectance error (ΔT_ρ). ΔT_ε is reduced due to an increase in effective emissivity caused by the cavity effect. ΔT_ρ is reduced because the direct concentrated irradiance (I_0) gets diffused inside the cavity leading to a weak reflected signal ($\rho_s \cdot I_0 \rightarrow 0$).

DMP was applied to experiments in a natural concentrated sunlight facility, where it was feasible to compare it directly against measurements from a calibrated solar-blind pyrometer operating at $5.5 \mu\text{m}$. For all samples the agreement between T_{dmp}^\sim and T_{cnrs} generally lied within 100 K. Despite the modest performance, it was observed that emissivity correction improved the accuracy of T_{dmp}^\sim . Particularly, in the case of the ZrO_2 sample, T_{dmp}^\sim measurements were consistent with the observed melting of the sample.

Unlike solar blind pyrometry that is typically used in solar furnace experiments, DMP offers the advantage of selecting freely the operating wavebands to better adapt to experimental requirements. To demonstrate this capability, the performance of DMP was assessed at four wavelengths in the near-IR region (0.88, 1.0, 1.1, 1.2 μm). The waveband selection entails a trade-off between the thermal (S) and reflected (R) signal levels, which are both indispensable for an accurate temperature measurement. For the temperatures (about 1000–3000 K) and wavebands (from 0.88 μm to 1.4 μm) considered in this thesis, S tends to increase at longer wavebands, while R at shorter wavebands, since it bears the spectral characteristics of the light source, i.e. the peaks of the xenon-arc lamp and the solar spectrum.

Several difficulties were encountered during the solar furnace experiments. Due to the blade's low rotation speed, the modulation frequency (ω_1) was at the low end of the lock-in's operating specifications leading to sporadic failures of the phase-lock loop. In addition, due to the blade being mounted parallel to the shutter blades, the modulation function ($m_1(t)$) was sensitive to the shutter opening.

The waviness of the heliostat surface resulted in an inhomogeneous spatial distribution of the deflected solar flux I_0 that was sensitive to the reflection angle, and hence varied with the position of the sun. As a consequence, the modulation function $m_1(t)$ varies during the day causing an unwanted drift to the calibration coefficient g_1 . Furthermore, the pyrliometer was located at a distance from the heliostat causing an error to the DNI measurements, especially in the presence of Cirrus clouds.

Although electronic modulation of the total output was not possible due to the configuration in the imaging furnace, the approach should not be abandoned since it could be applied in solar simulator facilities where the lamp's axis is oriented so that radiation from the electrode does not reach the target.

DMP could be improved by rethinking the temperature calibration step, which

was a limiting factor of performance. To increase the accuracy in the estimation of k_1, k_2, k_3 emphasis should be placed on conducting a high-quality temperature calibration step against a temperature-controlled black-body and taking measures to keep the $m_2(t)$ modulation function characteristics intact. Due to the fact that k_1, k_2, k_3 are decoupled from the $m_1(t)$ modulation function applied to I_0 , the instrument could be ported to a different setup without the need to repeat the temperature calibration step.

Most of the limitations associated with the application of the method at the CNRS solar furnace were caused by the fact that the experimental setup was not optimized to be used with DMP, and they could be easily overcome in future implementations. Specifically, the dependence of the modulation function $m_1(t)$ on shutter opening could be avoided by positioning the blade perpendicular to the shutter axis. In addition, the DNI measurements could function as a more reliable measure of I_0 , if the pyrhelimeter was installed at the location of the heliostat.

DMP could be enhanced to measure concurrently at multiple wavebands [62], offering the benefits of multi-spectral reflectance information and increased temperature accuracy. A prototype could be built such that the radiosity be collected and spatially dispersed to n opto-electronic modules, with the i^{th} module consisting of a narrow band filter centered at λ_i , a photo-detector and two lock-in amplifiers. The arrangement is equivalent to an array of n single-waveband double modulation pyrometers, where pyrometer i operates at λ_i and outputs the thermal signal S_i and reflectance signal R_i . Note that since $2n$ lock-in units would be required for the setup, the implementation of all-digital lock-ins by using Field-Programmable-Gate Arrays (FPGA) [129–136] could be pursued as this may be more economical for large n values.

While the above setup might contribute to increased accuracy during measurement, it would be worthwhile to investigate whether the redundant measurements of a multi-wavelength DMP pyrometer collected over a wide temperature range could in principle enable estimation of the temperature calibration coefficients without relying on any external reference source, i.e. a self-calibration of the instrument as in [82]. This would be of value because, as previously discussed, a proper calibration would require measurements against a temperature controlled black-body cavity with an operating range that overlaps with that of the pyrometer ($\approx 1000 - 3000$ K).

List of publications

Journal articles

Potamias, D., Alxneit, I., & Wokaun, A. (2017). Double modulation pyrometry: A radiometric method to measure surface temperatures of directly irradiated samples. *Review of Scientific Instruments*, 88(9), 95112.

Potamias, D., Alxneit, I., Koepf, E., and Wokaun, A. (2018). Double modulation pyrometry with emissivity correction based on in-situ reflectance measurements applied to surfaces with dynamic optical properties. *Journal of Solar Energy Engineering*, 141(1), 011003.

Potamias, D., Alxneit, I. and Wokaun, A. (2018). Assessment of Double Modulation Pyrometry as a diagnostic tool for use in concentrated solar facilities. *Solar Energy*, 174, 660-668.

List of Figures

1.1	Variables affecting the response \hat{T} of a radiometric sensor.	4
1.2	Schematics of natural sunlight concentrating facilities.	5
1.3	Schematics of solar simulators.	6
1.4	Comparison between the Air Mass 1.5 terrestrial solar spectrum [47] and the spectrum of the xenon-arc lamp that is typically used as light source in high-flux solar simulators.	8
1.5	The basic principle of double modulation pyrometry (DMP): modulation of the intensity of irradiance $I_0(t)$ and lock-in detection of the reflected fraction $\rho \cdot I_0(t)$	9
2.1	Classification of pyrometric methods in four quadrants with respect to their ability or not to eliminate any of the parasitic reflectance (ΔT_ρ) and emissivity (ΔT_ε) errors.	13
2.2	Experimental setup for the flash-assisted multi-wavelength pyrometry (FAMP). Adapted from Fig. 1 of [42].	23
3.1	Relative temperature error $\delta T/T$ arising from a 10% error in emissivity $\delta\varepsilon/\varepsilon$, plotted as a function of wavelength and temperature.	28
3.2	Lambertian surface δA . \hat{n} is the surface normal unit vector, while \hat{r} is the unit vector along the oblique observation angle.	29
3.3	Simplified schematic of the frequency spectrum of the detected signal $D(t)$	35
3.4	Distribution of light-intensity over wavelength for various components of a short discharge Xenon-arc lamp.	36
4.1	The operating principle of DMP.	40
4.2	R_1 and R_2 off a cold target measured with neutral density filters inserted in the optical path.	41
4.3	R'_1 and R_2 from gain calibrations sessions spanning a one-month period. Outlier corresponds to a new operation wavelength of $1.2 \mu\text{m}$	42
4.4	Temperature calibration setup.	43

4.5	Temperature calibration curve for DMP operated at $1.2 \mu\text{m}$ and $\epsilon_{\text{eff}} = 1.0$	43
4.6	Shut down behavior of arc lamp. The relative contribution of the anode's thermal emission is obtained by extrapolation (red line). . .	45
4.7	Imaging furnace with the xenon-arc lamp, pyrometer, conjugate focus, rotating blade and ray pattern.	46
4.8	Lamp model used in ray tracing simulations.	46
4.9	Measured spectral reflectivities of pure and oxidized aluminum. . .	47
4.10	Calculated (absorbed) flux distribution on blade with a square cross section and one side facing the source at $d = 9 \text{ cm}$, 800 W	48
4.11	$m(\theta)$ as function of aspect ratio a/b , $d = 9 \text{ cm}$ (bottom) and distance from the optical axis d , $a/b = 1$ (top).	48
4.12	Explanation of how the location of the blade's axis (d) affects the presence of higher harmonics.	49
4.13	The first four harmonics of the blade's modulation function as function of a/b (left) and d (right).	49
4.14	Response of R'_1 (top) and R_2 (bottom) to changes in I_0 and T	50
4.15	Comparison of true temperature recorded with solar blind pyrometer (T_{ref}) and DMP (T_{DMP}) while varying the relative strength of the cooling air flow (air). R'_1 is used to track changes in the sample's reflectivity.	51
4.16	Picture of Pt sample before and after the experiment.	52
4.17	Results of Fig. 4.15 shown with corrected temperature scale. (Left) Correction point coincides with melting. (Right) Correction point prior to melting.	53
4.18	Absolute temperature error due to transfer of calibration from reference operating at $\lambda_1 = 1.385 \mu\text{m}$ to DMP operating at $\lambda_2 = 1.2 \mu\text{m}$ as function of emissivity error at $T_{\text{true}} = 2000 \text{ K}$	54
4.19	Error propagation during calibration and measurement.	55
4.20	Probability density distributions of calibration constants (top) and combined uncertainty of T_{dmp}	56
4.21	Sensitivity of T_{DMP} on the calibration coefficients.	57
5.1	Schematic of DMP's measurement setup.	62
5.2	Representation of the measurement process.	63
5.3	Optical properties affecting the response of an opaque sample subjected to external radiation I_0	64
5.4	Final design of chopper wheel. Region bounding the radiative flux from the solar simulator is indicated in yellow (compare to Fig. 5.5, top).	65

5.5	Modulation function $m_1(t)$ determined by monte-carlo ray-tracing for all ten lamps used.	66
5.6	Calibration constant g_1 for different configurations of active light sources and operation wavelengths.	67
5.7	Relative spectral sensitivity of the DMP calculated from the spectral sensitivity of the detector (λ), the transmissivity of the filters and the spectral irradiance of the Xenon arc-lamp.	68
5.8	Temperatures and reflectivity measured on Al_2O_3 during heating of the sample.	70
5.9	Temperatures and reflectivity measured on ZrO_2 during heating of the sample.	71
5.10	Temperatures and reflectivity measured on SiSiC during heating of the sample.	72
5.11	Evolution of reflectance (ΔT_ρ) and emissivity (ΔT_ε) induced temperature errors extracted from data of Fig 5.8.	73
5.12	Ratio of thermal to reflected signals at all operating wavelengths as function of temperature based on the data presented in Fig. 5.8. . .	74
5.13	A simplified cross-section schematic of the reactor's cavity and window.	75
5.14	Temperature distribution of the glass window.	76
5.15	Temperature measurements during two heating cycles. The location of the sensors is indicated in Fig. 5.13.	77
6.1	Experimental setup of the CNRS experiments.	82
6.2	Gain calibration coefficient g_1 as function of operation wavelength and shutter transmission (τ_{shutter}).	84
6.3	Scatter plot of DMP's two lock-in amplifier outputs and fitted straight lines while observing a cold Lambertian reference.	85
6.4	Summary of data measured on a stainless steel sample used for temperature calibration.	86
6.5	Assessment of the temperature calibration for the four operation wavelengths ($\lambda = 0.88, 1.0, 1.1, 1.2 \mu\text{m}$).	87
6.6	Explanation of temperature observations belonging to the two instruments (DMP) and (CNRS).	88
6.7	Summary of data measured on copper (sample A).	90
6.8	Summary of data measured on copper (sample B).	91
6.9	High correlation of the T_{dmp} and ρ values collected during the first 3 mins of the Cu^B experiment.	92
6.10	Summary of data measured on a stainless steel sample.	93
6.11	Summary of data measured on Al_2TiO_5	95

6.12	Still images of the Al_2TiO_5 sample being exposed to concentrated radiance.	95
6.13	Summary of data measured on reticulate porous ZrO_2	97
6.14	Summary of temperature and reflectance data measured on reticulate porous CeO_2	98

List of Tables

- 2.1 Operating range and accuracy of pyrometric methods. 12
- 6.1 Symbols of measured temperatures 89

Bibliography

- [1] T. Duvaut, “Comparison between multiwavelength infrared and visible pyrometry: Application to metals,” *Infrared Physics & Technology*, vol. 51, no. 4, p 292, 2008.
- [2] R. Barber, “Glass Industry Applications,” in *Theory and Practice of Radiation Thermometry*, ser. Wiley Online Books, Hoboken, NJ, USA: John Wiley & Sons, Inc., 2007, p 973.
- [3] T Mizutani, “Correct substrate temperature monitoring with infrared optical pyrometer for molecular-beam epitaxy of III–V semiconductors,” *Journal of Vacuum Science & Technology B: Microelectronics and Nanometer Structures*, vol. 6, no. 6, p 1671, 1988.
- [4] M Delfino and D. Hodul, “Wavelength-specific pyrometry as a temperature measurement tool,” *IEEE Transactions on Electron Devices*, vol. 39, no. 1, p 89, 1992.
- [5] D. Ng and G. Fralick, “Use of a multiwavelength pyrometer in several elevated temperature aerospace applications,” *Review of Scientific Instruments*, vol. 72, no. 2, p 1522, 2001.
- [6] P. Herve and A. Sadou, “Determination of the complex index of refractory metals at high temperatures: Application to the determination of thermo-optical properties,” *Infrared Physics & Technology*, vol. 51, no. 3, p 249, 2008.
- [7] R. Khatami and Y. A. Levendis, “On the deduction of single coal particle combustion temperature from three-color optical pyrometry,” *Combustion and Flame*, vol. 158, no. 9, p 1822, 2011.
- [8] N. E. Tuffrey, G. G. Richards, and J. K. Brimacombe, “Two-wavelength pyrometry study of the combustion of sulfide minerals: Part I. Apparatus and general observations,” *Metallurgical and Materials Transactions B*, vol. 26, no. 5, p 929, 1995.

- [9] T. Panagiotou and Y. Leventis, "Observations on the Combustion of Polymers (Plastics): From Single Particles to Groups of Particles," *Combustion Science and Technology*, vol. 137, no. 1-6, p 121, 1998.
- [10] T. Fu, Z. Wang, and X. Cheng, "Temperature Measurements of Diesel Fuel Combustion With Multicolor Pyrometry," *Journal of Heat Transfer*, vol. 132, no. 5, p 051602, 2010.
- [11] J. Estevadeordal, N. Tralshawala, and V. Badami, "Multi-Color Imaging Pyrometry Techniques for Gas Turbine Engine Applications," in *Volume 2, Fora: Cavitation and Multiphase Flow; Fluid Measurements and Instrumentation; Microfluidics; Multiphase Flows: Work in Progress*, ASME, 2013, V002T11A007.
- [12] J. Estevadeordal, G. Wang, N. Nirmalan, A. Wang, S. P. Harper, and J. D. Rigney, "Multicolor Techniques for Identification and Filtering of Burst Signals in Jet Engine Pyrometers," *Journal of Turbomachinery*, vol. 136, no. 3, p 031004, 2013.
- [13] R. Reichle, P. Andrew, C. Balorin, B. Brichard, S. Carpentier, Y. Corre, M. Davi, R. Daviot, C. Desgranges, J. Gardarein, E. Gauthier, D. Guilhem, S. Gicquel, A. Herrmann, D. Hernandez, M. Jouve, C. Le Niliot, T. Loarer, A. Martin, J. Martins, J.-B. Migozzi, J. Patterlini, C. Pocheau, F. Rigollet, H. Roche, and J. Travere, "Concept and development of ITER divertor thermography diagnostic," *Journal of Nuclear Materials*, vol. 390-391, p 1081, 2009.
- [14] F. Trombe and Albert Le Phat Vinh, "Thousand kW solar furnace, built by the National Center of Scientific Research, in Odeillo (France)," *Solar Energy*, vol. 15, no. 1, p 57, 1973.
- [15] H. Ries and M. Schubnell, "The optics of a two-stage solar furnace," *Solar Energy Materials*, vol. 21, no. 2-3, p 213, 1990.
- [16] P. Haueter, T. Seitz, and A. Steinfeld, "A New High-Flux Solar Furnace for High-Temperature Thermochemical Research," *Journal of Solar Energy Engineering*, vol. 121, no. 1, p 77, 1999.
- [17] Y. Chen, K. Chong, C. Lim, B. Lim, K. Tan, O. Aliman, T. Bligh, B. Tan, and G. Ismail, "Report of the first prototype of non-imaging focusing heliostat and its application in high temperature solar furnace," *Solar Energy*, vol. 72, no. 6, p 531, 2002.
- [18] A Neumann and U Groer, "Experimenting with concentrated sunlight using the DLR solar furnace," *Solar Energy*, vol. 58, no. 4-6, p 181, 1996.

- [19] D. Riveros-Rosas, J. Herrera-Vázquez, C. Pérez-Rábago, C. Arancibia-Bulnes, S. Vázquez-Montiel, M. Sánchez-González, F. Granados-Agustín, O. Jaramillo, and C. Estrada, "Optical design of a high radiative flux solar furnace for Mexico," *Solar Energy*, vol. 84, no. 5, p 792, 2010.
- [20] A. Lewandowski, C. Bingham, J. O'Gallagher, R. Winston, and D. Sagie, "Performance characterization of the SERI High-Flux solar furnace," *Solar Energy Materials*, vol. 24, no. 1-4, p 550, 1991.
- [21] F Sibieude, M Ducarroir, A Tofighi, and J Ambritz, "High temperature experiments with a solar furnace: The decomposition of Fe₃O₄, Mn₃O₄, CdO," *International Journal of Hydrogen Energy*, vol. 7, no. 1, p 79, 1982.
- [22] B. Martínez, A. Roig, X. Obradors, E. Molins, A. Rouanet, and C. Monty, "Magnetic properties of γ -Fe₂O₃ nanoparticles obtained by vaporization condensation in a solar furnace," *Journal of Applied Physics*, vol. 79, no. 5, p 2580, 1996.
- [23] R. Levitan, H. Rosin, and M. Levy, "Chemical reactions in a solar furnace—Direct heating of the reactor in a tubular receiver," *Solar Energy*, vol. 42, no. 3, p 267, 1989.
- [24] A. Steinfeld, A. Frei, P. Kuhn, and D. Wuillemin, "Solar thermal production of zinc and syngas via combined ZnO-reduction and CH₄-reforming processes," *International Journal of Hydrogen Energy*, vol. 20, no. 10, p 793, 1995.
- [25] N Tzouganatos, R Matter, C Wieckert, J Antrekowitsch, M Gamroth, and A Steinfeld, "Thermal Recycling of Waelz Oxide Using Concentrated Solar Energy," *JOM*, vol. 65, no. 12, p 1733, 2013.
- [26] P. Kuhn and A. Hunt, "A new solar simulator to study high temperature solid-state reactions with highly concentrated radiation," *Solar Energy Materials*, vol. 24, no. 1-4, p 742, 1991.
- [27] D. Hirsch, P. V. Zedtwitz, T. Osinga, J. Kinamore, and A. Steinfeld, "A New 75 kW High-Flux Solar Simulator for High-Temperature Thermal and Thermochemical Research," *Journal of Solar Energy Engineering*, vol. 125, no. 1, p 117, 2003.
- [28] J. Petrasch, P. Coray, A. Meier, M. Brack, P. Haberling, D. Wuillemin, and A. Steinfeld, "A Novel 50 kW 11,000 suns High-Flux Solar Simulator Based on an Array of Xenon Arc Lamps," *Journal of Solar Energy Engineering*, vol. 129, no. 4, p 405, 2007.
- [29] D. S. Codd, A. Carlson, J. Rees, and A. H. Slocum, "A low cost high flux solar simulator," *Solar Energy*, vol. 84, no. 12, p 2202, 2010.

- [30] K. R. Krueger, J. H. Davidson, and W. Lipinski, "Design of a New 45 kW_e High-Flux Solar Simulator for High-Temperature Solar Thermal and Thermochemical Research," *Journal of Solar Energy Engineering*, vol. 133, no. 1, p 011013, 2011.
- [31] W. Wang, L. Aichmayer, B. Laumert, and T. Fransson, "Design and Validation of a Low-cost High-flux Solar Simulator using Fresnel Lens Concentrators," *Energy Procedia*, vol. 49, no. 0, p 2221, 2014.
- [32] K. R. Krueger, W. Lipiński, and J. H. Davidson, "Operational Performance of the University of Minnesota 45 kW_e High-Flux Solar Simulator," *Journal of Solar Energy Engineering*, vol. 135, no. 4, p 044501, 2013.
- [33] R. Bader, S. Haussener, and W. Lipinski, "Optical Design of Multisource High-Flux Solar Simulators," *Journal of Solar Energy Engineering*, vol. 137, no. 2, p 021012, 2014.
- [34] J. Sarwar, G. Georgakis, R. LaChance, and N. Ozalp, "Description and characterization of an adjustable flux solar simulator for solar thermal, thermochemical and photovoltaic applications," *Solar Energy*, vol. 100, p 179, 2014.
- [35] R. Gill, E. Bush, P. Haueter, and P. Loutzenhiser, "Characterization of a 6 kW high-flux solar simulator with an array of xenon arc lamps capable of concentrations of nearly 5000 suns," *Review of Scientific Instruments*, vol. 86, no. 12, p 125107, 2015.
- [36] B. M. Ekman, G. Brooks, and M. A. Rhamdhani, "Development of High Flux Solar Simulators for Solar Thermal Research," in *Energy Technology 2015*, vol. 141, Cham: Springer International Publishing, 2015, p 149.
- [37] K. Wieghardt, K.-H. Funken, G. Dibowski, B. Hoffschmidt, D. Laaber, P. Hilger, and K.-P. Eßer, "SynLight – the world's largest artificial sun," in *AIP Conference Proceedings*, vol. 1734, 2016, p 030038.
- [38] G. Levêque, R. Bader, W. Lipiński, and S. Haussener, "Experimental and numerical characterization of a new 45 kW_e multisource high-flux solar simulator," *Optics Express*, vol. 24, no. 22, A1360, 2016.
- [39] A. Gallo, A. Marzo, E. Fuentealba, and E. Alonso, "High flux solar simulators for concentrated solar thermal research: A review," *Renewable and Sustainable Energy Reviews*, vol. 77, no. April, p 1385, 2017.
- [40] J. Petrasch, P. Coray, A. Meier, M. Brack, P. Haberling, D. Wullemin, and A. Steinfeld, "A Novel 50 kW 11,000 suns High-Flux Solar Simulator Based on an Array of Xenon Arc Lamps," *Journal of Solar Energy Engineering*, vol. 129, no. 4, p 405, 2007.

- [41] A. Marzo, J. Ballestrín, J. Barbero, I. Cañadas, and J. Rodríguez, “Solar blind pyrometry not relying on atmospheric absorption bands,” *Solar Energy*, vol. 107, p 415, 2014.
- [42] H. R. Tschudi and G. Morian, “Pyrometric Temperature Measurements in Solar Furnaces,” *Journal of Solar Energy Engineering*, vol. 123, no. 2, p 164, 2001.
- [43] D Hernandez, G Olalde, J. M. Gineste, and C Gueymard, “Analysis and Experimental Results of Solar-Blind Temperature Measurements in Solar Furnaces,” English, *Journal of Solar Energy Engineering*, vol. 126, no. 1, p 645, 2004.
- [44] A. P. Freid, P. K. Johnson, M. Musella, R. Muller, J. E. Steinbrenner, and R. D. Palumbo, “Solar Blind Pyrometer Temperature Measurements in High Temperature Solar Thermal Reactors: A Method for Correcting the System-Sensor Cavity Reflection Error,” *Journal of Solar Energy Engineering*, vol. 127, no. 1, p 86, 2005.
- [45] M. Pfänder, E. Lüpfert, and P. Pistor, “Infrared temperature measurements on solar trough absorber tubes,” *Solar Energy*, vol. 81, no. 5, p 629, 2007.
- [46] J. Ballestrín, A. Marzo, I. Cañadas, and J. Rodríguez, “Testing a solar-blind pyrometer,” en, *Metrologia*, vol. 47, no. 6, p 646, 2010.
- [47] ASTM G173-03(2012), *Standard Tables for Reference Solar Spectral Irradiances: Direct Normal and Hemispherical on 37deg Tilted Surface*, West Conshohocken, 2012.
- [48] D. Nakar, A. Malul, D. Feuermann, and J. M. Gordon, “Radiometric characterization of ultrahigh radiance xenon short-arc discharge lamps,” *Applied Optics*, vol. 47, no. 2, p 224, 2008.
- [49] M Schubnell and H. R. Tschudi, “Simultaneous measurement of irradiation, temperature and reflectivity on hot irradiated surfaces,” *Applied Physics A Materials Science & Processing*, vol. 60, no. 6, p 581, 1995.
- [50] M. Schubnell, H. Tschudi, and C. Müller, “Temperature measurement under concentrated radiation,” *Solar Energy*, vol. 58, no. 1-3, p 69, 1996.
- [51] H. R. Tschudi, M. Schubnell, and C. Müller, “Measuring temperatures on absorbers irradiated in a solar furnace by flash assisted multi-wavelength pyrometry (FAMP),” en, *Le Journal de Physique IV*, vol. 09, no. PR3, Pr3, 1999.
- [52] H. R. Tschudi and M. Schubnell, “Measuring temperatures in the presence of external radiation by flash assisted multiwavelength pyrometry,” English, *Review of Scientific Instruments*, vol. 70, no. 6, p 2719, 1999.

- [53] G. R. Gathers, "Monte Carlo studies of multiwavelength pyrometry using linearized equations," *International Journal of Thermophysics*, vol. 13, no. 2, p 361, 1992.
- [54] M. A. Khan, C. Allemand, and T. W. Eagar, "Noncontact temperature measurement. I. Interpolation based techniques," *Review of Scientific Instruments*, vol. 62, no. 2, p 392, 1991.
- [55] P. A. Ni, R. M. More, H Yoneda, and F. M. Bieniosek, "Polarization pyrometry: An improvement to multi-wavelength optical pyrometry," *Review of Scientific Instruments*, vol. 83, no. 12, p 123501, 2012.
- [56] D. Hernandez, G. Olalde, A. Beck, and E. Milcent, "Bicolor pyroreflectometer using an optical fiber probe," *Review of Scientific Instruments*, vol. 66, no. 12, p 5548, 1995.
- [57] D. Hernandez, "A concept to determine the true temperature of opaque materials using a tricolor pyroreflectometer," *Review of Scientific Instruments*, vol. 76, no. 2, p 024904, 2005.
- [58] D Hernandez, A Netchaieff, and A Stein, "True temperature measurement on metallic surfaces using a two-color pyroreflectometer method," *Review of Scientific Instruments*, vol. 80, no. 9, p 094903, 2009.
- [59] E. Delchambre, D. Hernandez, M. H. Aumeunier, T. Loarer, and E. Gauthier, "Performance of pyroreflectometry in a reflective environment," *Physica Scripta*, vol. T145, p 014078, 2011.
- [60] N. Rohner and A. Neumann, "Measurement of High Temperatures in the DLR Solar Furnace by UV-B Detection," *Journal of Solar Energy Engineering*, vol. 125, no. 2, p 152, 2003.
- [61] N. J. Themelis and W. H. Gauvin, "A two-wavelength pyrometer for temperature measurements in gas-solids systems," *The Canadian Journal of Chemical Engineering*, vol. 40, no. 4, p 157, 1962.
- [62] P. B. Coates, "Multi-Wavelength Pyrometry," en, *Metrologia*, vol. 17, no. 3, p 103, 1981.
- [63] M. A. Khan, C. Allemand, and T. W. Eagar, "Noncontact temperature measurement. II. Least squares based techniques," *Review of Scientific Instruments*, vol. 62, no. 2, p 403, 1991.
- [64] M. Hoch, "Multiwavelength pyrometry: Radiance temperature versus wavelength curve should be used for temperature determination," *Review of Scientific Instruments*, vol. 63, no. 9, p 4205, 1992.

- [65] G. B. Hunter, C. D. Allemand, and T. W. Eagar, "An improved method of multi-wavelength pyrometry," *Proceedings of SPIE*, vol. 520, no. December 1985, p 40, 1984.
- [66] T. Duvaut, D. Georgeault, and J. Beaudoin, "Multiwavelength infrared pyrometry: optimization and computer simulations," *Infrared Physics & Technology*, vol. 36, no. 7, p 1089, 1995.
- [67] C.-d. Wen and Y.-h. Chr, "The Assessment of Multispectral Radiation Thermometry Using Linear and Log-Linear Emissivity Models for Steel," *Numerical Heat Transfer, Part B: Fundamentals*, vol. 58, no. 1, p 40, 2010.
- [68] C.-D. Wen and T.-Y. Chai, "Experimental investigation of emissivity of aluminum alloys and application of multispectral radiation thermometry," *Applied Thermal Engineering*, vol. 31, no. 14-15, p 2414, 2011.
- [69] M. Hoch, "The integral six-color pyrometer: Linear dependence of the radiance temperature from the wavelength λ ," *Review of Scientific Instruments*, vol. 63, no. 4, p 2274, 1992.
- [70] J. L. Gardner and T. P. Jones, "Multi-wavelength radiation pyrometry where reflectance is measured to estimate emissivity," *Journal of Physics E: Scientific Instruments*, vol. 13, no. 3, p 306, 1980.
- [71] K. a. Bertness, "Smart pyrometry for combined sample temperature and reflectance measurements in molecular-beam epitaxy," *Journal of Vacuum Science & Technology B: Microelectronics and Nanometer Structures*, vol. 18, no. 3, p 1426, 2000.
- [72] F. Boebel and H. Moller, "Simultaneous in-situ measurement of film thickness and temperature by using multiple wavelength pyrometric interferometry (MWPI)," in *IEEE/SEMI Advanced Semiconductor Manufacturing Conference and Workshop - ASMC '92 Proceedings*, vol. 6, IEEE, 1993, p 67.
- [73] D Hernandez, J. L. Sans, and M. Pfander, "Pyroreflectometry to Determine the True Temperature and Optical Properties of Surfaces," *Journal of Solar Energy Engineering*, vol. 130, no. 3, p 031003, 2008.
- [74] D Hernandez, J. Sans, A Netchaieff, P Ridoux, and V Le Sant, "Experimental validation of a pyroreflectometric method to determine the true temperature on opaque surface without hampering reflections," *Measurement*, vol. 42, no. 6, p 836, 2009.
- [75] V. Grigorova, A. Semerok, D. Farcage, J. Weulersse, P. Thro, E. Gauthier, H. Roche, T. Loarer, and C. Grisolia, "Temperature measurement of plasma-facing surfaces in tokamaks by active pyrometry," *Journal of Nuclear Materials*, vol. 390-391, p 1097, 2009.

- [76] T. Loarer, "Surface Temperature Measurement of Plasma Facing Components in Metallic Environment," *Contributions to Plasma Physics*, vol. 51, no. 2-3, p 201, 2011.
- [77] S. Amiel, T. Loarer, C. Pocheau, H. Roche, E. Gauthier, M.-H. Aumeunier, C. Le Niliot, F. Rigollet, X. Courtois, M. Jouve, C. Balorin, and V. Moncada, "2D surface temperature measurement of plasma facing components with modulated active pyrometry," *Review of Scientific Instruments*, vol. 85, no. 10, p 104905, 2014.
- [78] D Hernandez, J. L. Sans, and M. Pfander, "Pyroreflectometry to Determine the True Temperature and Optical Properties of Surfaces," *Journal of Solar Energy Engineering*, vol. 130, no. 3, p 031003, 2008.
- [79] S Amiel, T Loarer, C Pocheau, H Roche, M. H. Aumeunier, E Gauthier, C. L. Niliot, and F Rigollet, "Surface temperature measurement of plasma facing components with active pyrometry," *Journal of Physics: Conference Series*, vol. 395, p 012074, 2012.
- [80] P. Ni, M. Kulish, V. Mintsev, D. Nikolaev, V. Ternovoi, D. Hoffmann, S. Udrea, A. Hug, N. Tahir, and D. Varentsov, "Temperature measurement of warm-dense-matter generated by intense heavy-ion beams," *Laser and Particle Beams*, vol. 26, no. 04, p 583, 2008.
- [81] H Pauly and F Engel, *Das Pyrometer-Kompendium: eine Firmenschrift der IMPAC Electronic GmbH*. IMPAC Electronic, 1999.
- [82] N. B. Crane, "Pyrometric Temperature Measurement in Concentrated Sunlight With Emissivity Determination," *Journal of Solar Energy Engineering*, vol. 132, no. 1, p 011007, 2010.
- [83] A. Seifter and A. W. Obst, "About the Proper Wavelength for Pyrometry on Shock Physics Experiments," *International Journal of Thermophysics*, vol. 28, no. 3, p 934, 2007.
- [84] T. A. Ota, D. J. Chapman, and D. E. Eakins, "Monte-Carlo modelling to determine optimum filter choices for sub-microsecond optical pyrometry," *Review of Scientific Instruments*, vol. 88, no. 4, p 044902, 2017.
- [85] F. Sakuma and S. Hattori, "Establishing a practical temperature standard by using a narrow-band radiation thermometer with a silicon detector," *Bulletin of NRLM*, vol. 32, no. 2, p91, 1983.
- [86] A Ono, S Hattori, and F Sakuma, "Detector-Based Traceability of Temperature Standards," in *Theory and Practice of Radiation Thermometry*, Hoboken, NJ, USA: John Wiley & Sons, Inc., 2007, p 839.

- [87] J. W. Hahn and C Rhee, “Interpolation Equation for the Calibration of Infrared Pyrometers,” *Metrologia*, vol. 31, no. 1, p 27, 1994.
- [88] P Saunders, “Uncertainties in the realization of thermodynamic temperature above the silver point,” *International Journal of Thermophysics*, vol. 32, no. 1-2, p 26, 2011.
- [89] P. Saunders, J. Fischer, M. Sadli, M. Battuello, C. W. Park, Z. Yuan, H. Yoon, W. Li, E. van der Ham, F. Sakuma, J. Ishii, M. Ballico, G. Machin, N. Fox, J. Hollandt, M. Matveyev, P. Bloembergen, and S. Ugur, “Uncertainty Budgets for Calibration of Radiation Thermometers below the Silver Point,” *International Journal of Thermophysics*, vol. 29, no. 3, p 1066, 2008.
- [90] I. Alxneit, “Measuring temperatures in a high concentration solar simulator – Demonstration of the principle,” *Solar Energy*, vol. 85, no. 3, p 516, 2011.
- [91] F. E. Nicodemus, J. Richmond, J. Hsia, I. Ginsberg, and T. Limperis, *Geometrical Considerations and Nomenclature for Reflectance*. US Department of Commerce, National Bureau of Standards, 1977.
- [92] T. F. Coleman and Y. Li, “On the convergence of interior-reflective Newton methods for nonlinear minimization subject to bounds,” *Mathematical Programming*, vol. 67, no. 1-3, p 189, 1994.
- [93] ———, “An Interior Trust Region Approach for Nonlinear Minimization Subject to Bounds,” *SIAM Journal on Optimization*, vol. 6, no. 2, p 418, 1996.
- [94] C. Guesdon, I. Alxneit, H. R. Tschudi, D. Wuillemin, and M. Sturzenegger, “1kW imaging furnace with in situ measurement of surface temperature,” *Review of Scientific Instruments*, vol. 77, no. 3, p 035102, 2006.
- [95] C Guesdon, I Alxneit, H. Tschudi, D Wuillemin, J Petrasch, Y Brunner, L Winkel, and M Sturzenegger, “PSI’s 1kW imaging furnace—A tool for high-temperature chemical reactivity studies,” *Solar Energy*, vol. 80, no. 10, p 1344, 2006.
- [96] S. Deemyad and I. F. Silvera, “Temperature dependence of the emissivity of platinum in the IR,” *Review of Scientific Instruments*, vol. 79, no. 8, p 086105, 2008.
- [97] D. De Sousa Meneses, P. Melin, L. del Campo, L. Cosson, and P. Echegut, “Apparatus for measuring the emittance of materials from far infrared to visible wavelengths in extreme conditions of temperature,” *Infrared Physics & Technology*, vol. 69, p 96, 2015.
- [98] G. A. F. Seber and C. J. Wild, *Nonlinear Regression*, ser. Wiley Series in Probability and Statistics. Hoboken, NJ, USA: John Wiley & Sons, Inc., 1989.

- [99] I Alxneit, *rt — a multi-threaded Monte-Carlo geometric ray tracer [Computer software]*, Available at <https://github.com/ialxn/rt>, 2016.
- [100] H. Ehrenreich, H. R. Philipp, and B. Segall, “Optical properties of Aluminum,” *Physical Review*, vol. 132, no. 5, p 1918, 1963.
- [101] J Bartl and M Baranek, “Emissivity of aluminium and its importance for radiometric measurement,” *Measurement Science Review*, vol. 4, no. 3, p 31, 2004.
- [102] ANSYS® *Academic Research, Release 14.5*.
- [103] G. K. Burgess and R. G. Waltenberg, “The Emissivity of Metals and Oxides, II: Measurements with the Micropyrometer,” *Physical Review*, vol. 4, no. 6, p 546, 1914.
- [104] D. Potamias, I. Alxneit, and A. Wokaun, “Double modulation pyrometry: A radiometric method to measure surface temperatures of directly irradiated samples,” *Review of Scientific Instruments*, vol. 88, no. 9, p 095112, 2017.
- [105] M. Alaa, M. Rady, M. Attia, and E. Ewais, “Optical study of using ceramic foams for volumetric solar receivers,” in *2016 International Renewable and Sustainable Energy Conference (IRSEC)*, IEEE, 2016, p 284.
- [106] A. Kribus, Y. Gray, M. Grijnevich, G. Mittelman, S. Mey-Cloutier, and C. Caliot, “The promise and challenge of solar volumetric absorbers,” *Solar Energy*, vol. 110, p 463, 2014.
- [107] A. Kuwabara, T. Tohei, T. Yamamoto, and I. Tanaka, “Ab initio lattice dynamics and phase transformations of Zr O 2,” *Physical Review B*, vol. 71, no. 6, p 064301, 2005.
- [108] A. Y. Vorob’ev, V. A. Petrov, V. E. Titov, and A. P. Chernyshov, “The reflectivity of alumina ceramics under intense surface heating and subsequent free cooling,” *High Temperature*, vol. 45, no. 1, p 13, 2007.
- [109] C. P. Cagran, L. M. Hanssen, M. Noorma, A. V. Gura, and S. N. Mekhontsev, “Temperature-resolved infrared spectral emissivity of SiC and Pt–10Rh for temperatures up to 900C,” *International Journal of Thermophysics*, vol. 28, no. 2, p 581, 2007.
- [110] B. Rousseau, S. Guevelou, A. Mekeze-Monthe, J. Vicente, L. Del Campo, D. De Sousa Meneses, P. Echegut, C. Caliot, and G. Flamant, “Tuning the spectral emittance of α -SiC open-cell foams up to 1300 K with their macro porosity,” *AIP Advances*, vol. 6, no. 6, p 065226, 2016.
- [111] R. H. Breeze and B. Ke, “Some comments on xenon arc lamp stability,” *Review of Scientific Instruments*, vol. 43, no. 5, p 821, 1972.

- [112] S. Rolt, P. Clark, J. Schmoll, and B. J. R. Shaw, "Xenon arc lamp spectral radiance modelling for satellite instrument calibration," H. A. MacEwen, G. G. Fazio, M. Lystrup, N. Batalha, N. Siegler, and E. C. Tong, Eds., vol. 9904, 2016, p 99044V.
- [113] R. G. Wilson, "Hemispherical spectral emittance of ablation chars, carbon, and zirconia to 3700 K," National Aeronautics and Space Administration, Hampton VA, Langley Research Center, NASA Technical Note NASA TN D-2704, 1965.
- [114] G. Teodorescu and P. D. Jones, "Spectral and directional emittance of alumina at 823 K," *Journal of Materials Science*, vol. 43, no. 22, p 7225, 2008.
- [115] D. Marxer, P. Furler, M. Takacs, and A. Steinfeld, "Solar thermochemical splitting of CO₂ into separate streams of CO and O₂ with high selectivity, stability, conversion, and efficiency," *Energy & Environmental Science*, vol. 10, no. 5, p 1142, 2017.
- [116] D. Potamias, I. Alxneit, E. Koepf, and A. Wokaun, "Double modulation pyrometry with emissivity correction based on in-situ reflectance measurements applied to surfaces with dynamic optical properties," *Journal of Solar Energy Engineering*, 2018.
- [117] E. Sani, L. Mercatelli, J.-L. Sans, and D. Sciti, "Optical properties of black and white ZrO₂ for solar receiver applications," *Solar Energy Materials and Solar Cells*, vol. 140, p 477, 2015.
- [118] J. Li, G. Vizkelethy, P. Revesz, J. W. Mayer, and K. N. Tu, "Oxidation and reduction of copper oxide thin films," *Journal of Applied Physics*, vol. 69, no. 2, p 1020, 1991.
- [119] S. Lahiri, N. Waalib Singh, K. Heng, L. Ang, and L. Goh, "Kinetics of oxidation of copper alloy leadframes," *Microelectronics Journal*, vol. 29, no. 6, p 335, 1998.
- [120] P. D. Jones, G. Teodorescu, and R. a. Overfelt, "Spectral-Directional Emittance of CuO at High Temperatures," *Journal of Heat Transfer*, vol. 128, no. 4, p 382, 2006.
- [121] Y. S. Touloukian and D. P. DeWitt, *Thermal Radiative Properties*. Boston, MA: Springer US, 1970, p 14.
- [122] G. Teodorescu, *Radiative emissivity of metals and oxidized metals at high temperature*, 2007.
- [123] B. Karlsson, C. G. Ribbing, A. Roos, E. Valkonen, and T. Karlsson, "Optical Properties of Some Metal Oxides in Solar Absorbers," *Physica Scripta*, vol. 25, no. 6A, p 826, 1982.

- [124] J. Ballestrín, J. Rodríguez, M. E. Carra, I. Cañadas, M. I. Roldan, J. Barbero, and A. Marzo, "Pyrometric method for measuring emittances at high temperatures," in *AIP Conference Proceedings*, vol. 1734, 2016, p 130003.
- [125] Mikron Instrument Company, *Table of Emissivity of Various Surfaces*, 2014.
- [126] F. Zhang, K. Yu, K. Zhang, Y. Liu, K. Xu, and Y. Liu, "An emissivity measurement apparatus for near infrared spectrum," *Infrared Physics & Technology*, vol. 73, p 275, 2015.
- [127] S. T. Norberg, N. Ishizawa, S. Hoffmann, and M. Yoshimura, "Redetermination of β -Al₂TiO₅ obtained by melt casting," *Acta Crystallographica Section E Structure Reports Online*, vol. 61, no. 8, p i160, 2005.
- [128] S. Ackermann and A. Steinfeld, "Spectral hemispherical reflectivity of non-stoichiometric cerium dioxide," *Solar Energy Materials and Solar Cells*, vol. 159, p 167, 2017.
- [129] G. Giaconia, G. Greco, L. Mistretta, and R. Rizzo, "Exploring FPGA-Based Lock-In Techniques for Brain Monitoring Applications," *Electronics*, vol. 6, no. 1, p 18, 2017.
- [130] M. O. Sonnaillon and F. J. Bonetto, "A low-cost, high-performance, digital signal processor-based lock-in amplifier capable of measuring multiple frequency sweeps simultaneously," *Review of Scientific Instruments*, vol. 76, no. 2, p 024703, 2005.
- [131] D. Wenn, "Implementing digital lock-in amplifiers using the dsPIC® DSC," *Application Note*, 2007.
- [132] G Yang, J. F. Barry, E. S. Shuman, M. H. Steinecker, and D DeMille, "A low-cost, FPGA-based servo controller with lock-in amplifier," *Journal of Instrumentation*, vol. 7, no. 10, P10026, 2012.
- [133] A. Restelli, R. Abbiati, and A. Geraci, "Digital field programmable gate array-based lock-in amplifier for high-performance photon counting applications," *Review of Scientific Instruments*, vol. 76, no. 9, p 093112, 2005.
- [134] J. M. Masciotti, J. M. Lasker, and A. H. Hielscher, "Digital Lock-In Detection for Discriminating Multiple Modulation Frequencies With High Accuracy and Computational Efficiency," *IEEE Transactions on Instrumentation and Measurement*, vol. 57, no. 1, p 182, 2008.
- [135] J.-j. Vandenbussche, P. Lee, and J. Peuteman, "On the Accuracy of Digital Phase Sensitive Detectors Implemented in FPGA Technology," *IEEE Transactions on Instrumentation and Measurement*, vol. 63, no. 8, p 1926, 2014.

- [136] J. W. Wilson, W. S. Warren, and M. C. Fischer, “Real-time digital signal processing in multiphoton and time-resolved microscopy,” in *Optical Biopsy XIV: Toward Real-Time Spectroscopic Imaging and Diagnosis*, R. R. Alfano and S. G. Demos, Eds., vol. 9703, 2016, 97030O.